

D^0 mesons in jets in pp collisions: preliminary figures for HP 2018 (jet p_T cross-section), SQM 2019 (parallel momentum fraction)

Auro Mohanty¹, Barbara A. Trzeciak¹, André Mischke¹

1. Utrecht University, the Netherlands

Email: auro.mohanty@cern.ch, barbara.antonina.trzeciak@cern.ch, A.Mischke@uu.nl

Abstract

Heavy quarks (charm and beauty) are produced in hard parton scatterings in the early stages of hadronic collisions. Therefore, they are ideal probes to investigate the properties of the Quark-Gluon Plasma (QGP) produced in ultra-relativistic heavy-ion collisions. The measurement of heavy-flavour jets gives more direct access to the initial parton kinematics and can provide further constraints for heavy-quark energy loss mechanisms, in particular adding information on how the radiated energy is dissipated in the medium. It also allows us to characterize the heavy-quark fragmentation process and its possible modification in the hot nuclear matter environment.

Studies in pp collisions are mandatory to characterize heavy quark production and fragmentation in vacuum, constituting the necessary reference for interpreting heavy-ion collision results. Differences between results from pp and p-Pb collisions can give insight on how the heavy-quark production and hadronization into jets is affected by cold nuclear matter effects.

The aim of the analysis is to present studies of the D^0 -tagged jets in pp collisions at $\sqrt{s} = 5.02$ TeV. We identify D-meson candidates via their hadronic decay channels using topological selections and particle identification. These candidates are combined with the other charged tracks reconstructed by the central tracking system, using the anti- k_T jet-finding algorithm. We extract the yield of D-tagged jets through their invariant mass analysis in bins of D^0 p_T and get their jet p_T spectra or $z_{||}$ distribution.

In this note, we present details of the D^0 -tagged jet analysis approved as a preliminary result for the Hard Probes 2018 conference: p_T differential cross-section in pp at $\sqrt{s} = 5.02$ TeV. The measurement was also be used as a baseline for the preliminary D^0 -jet measurement in p-Pb collisions at $\sqrt{s_{NN}} = 5.02$ TeV, in order to extract the nuclear modification factor R_{pPb} . Also presented in this note are parallel momentum fraction ($z_{||,ch} = \frac{\vec{p}_{ch,jet} \cdot \vec{p}_D}{\vec{p}_{ch,jet} \cdot \vec{p}_{ch,jet}}$) studies for different jet radii $R = 0.3, 0.4$ in different intervals of jet p_T aiming to be approved for Strangeness in Quark Matter 2019.

Contents

1	Software	1
2	Dataset and Event Selection	1
2.1	Monte Carlo productions	2
2.1.1	D ⁰ -tagged jets	2
3	D-Meson Selection	2
3.1	Particle Identification	3
4	Jet Reconstruction	3
4.1	Jet Selection	3
5	Raw Yield Extraction	4
5.1	Side-Band Subtraction: jet p_T cross-section, $R = 0.3$	4
5.2	Side-Band Subtraction: $z_{ ,ch}$ distribution, $R = 0.3, 0.4$	4
5.2.1	$R = 0.3$	4
5.2.2	$R = 0.4$	6
6	Efficiency Correction Procedure	17
6.1	Reconstruction Efficiency	17
6.2	Efficiency-Corrected Yields	17
6.2.1	Side-Band Subtraction Method	17
7	Detector Response Matrix	23
7.1	Jet Momentum Detector Response	23
7.2	Parallel Momentum Fraction Detector Response	23
8	Feed-Down Correction	27
8.1	Monte Carlo Simulation	27
8.2	Feed-Down Subtraction for jet- p_T cross-section and $z_{ ,ch}$ distributions	27
9	Unfolding	33
9.1	D ⁰ -tagged jets	33
9.2	D ⁰ -tagged jets: Parallel momentum fraction, $z_{ }^{ch}$	33
9.2.1	$R = 0.3$	34
9.2.2	$R = 0.4$	34

10 Systematic Uncertainties	45
10.1 Raw Yield Extraction	45
10.1.1 Fitting procedure	45
10.1.2 Variation of signal and side-band ranges	46
10.1.3 Variation of reflection to signal ratio	47
10.2 D-Meson Selection Cuts	47
10.3 B Feed-Down Correction	48
10.4 Unfolding	49
10.5 Tracking Efficiency	51
10.6 Tracking Efficiency – Jet Energy Scale	52
10.7 p_T Shape of the Monte Carlo Spectrum	52
10.8 Summary of Systematic Uncertainties	53
10.8.1 Systematic Uncertainties for R_{pPb}	53
11 Results	56
11.0.1 Monte Carlo Simulations	56
12 Preliminary Figures	57
13 Nuclear Modification Factor (R_{pPb})	57

1 Software

The main analysis tasks (C++ classes) used in the analysis are in the PWGJE library of the AliPhysics software package:

- AliAnalysisTaskSEDmesonsFilterCJ (filters D mesons and creates a set of particles with the D meson instead of the daughters);
- AliAnalysisTaskFlavourJetCorrelations (correlates each D meson found with a jet);
- AliEmcalJetTask ;
- AliAnalysisTaskRhoSparse.

The AliPhysics version used for this analysis is the analysis tag: vAN-20170826 (with AliRoot v5-09-14-1).

The task used for this analysis generates a multiple axis histogram (THnSparse) that keeps information about: $z_{||}$, jet p_T , D-meson p_T and D-meson invariant mass.

The post-processing includes: projection of the THnSparse onto lower-dimensional histograms, raw signal extraction, response matrix generation, B feed-down correction, unfolding and the final plotting. The post-processing is relatively light-weight and is performed directly in a personal computer. This code is written using the C++ with ROOT.

The analysis follows closely the analysis procedure of the D⁰-jet p_T differential cross-section measurement in p–Pb collisions at $\sqrt{s_{NN}}=5.02$ TeV: <https://aliceinfo.cern.ch/Notes/node/784> and in pp collisions at $\sqrt{s}=5.02$ TeV: <https://aliceinfo.cern.ch/Notes/node/840>.

2 Dataset and Event Selection

For this analysis we use the data collected by ALICE in 2017 during the Minimum Bias period of the pp collisions at $\sqrt{s} = 5.02$ TeV. This data corresponds to the following data taking periods: LHC17p and LHC17q pass1, FAST and CENT_woSDD productions were merged. The complete list of runs used in this analysis are:

LHC17p_CENT_woSDD: 282343, 282342, 282341, 282340, 282314, 282313, 282312, 282309, 282307, 282306, 282305, 282304, 282303, 282302, 282247, 282230, 282229, 282227, 282224, 282206, 282189, 282147, 282146, 282127, 282126, 282125, 282123, 282122, 282120, 282119, 282118, 282099, 282098, 282078, 282051, 282050, 282031, 282030, 282025, 282021, 282016, 282008

LHC17p_FAST: 282343, 282342, 282341, 282340, 282314, 282313, 282312, 282309, 282307, 282306, 282305, 282304, 282303, 282302, 282247, 282230, 282229, 282227, 282224, 282206, 282189, 282147, 282146, 282127, 282126, 282125, 282123, 282122, 282120, 282119, 282118, 282099, 282098, 282078, 282051, 282050, 282031, 282025, 282021, 282016, 282008

LHC17q_CENT_woSDD: 282367, 282366, 282365

LHC17q_FAST: 282367, 282366, 282365

Events were selected using the event selection kINT7. Note that the analysis is performed in AOD, where the beam-gas and gas-gas events have been filtered out. Events were further filtered using the Physics Selection, and selection provided by:

- `AliAnalysisTaskEmcal::IsEventSelected()`, which rejects events based on event vertex quality, in particular requiring a reconstructed vertex position not farther than 10 cm from the center of the detector along the beam axis; and a distance between the SPD vertex and the V0 vertex not larger than 0.5 cm;
- `AliRDHFCutsDStartoKpypi::IsEventSelected(AliEvent*)`, which rejects events for D* candidates based on event vertex quality and pileup
- `AliRDHFCutsD0toKpi::IsEventSelected(AliEvent*)`, which rejects events for D⁰ candidates based on event vertex quality and pileup.

The total number of events is 906.308 M out of analysed (after all the selections outlined below). Results shown in this *note* come from the LEGO train HFCJ_pp 437 for jet p_T cross-section with $R = 0.3$ and HFCJ_pp 437, 503 for $z_{||}$ distribution for $R = 0.3, 0.4$ respectively. (including: LHC17p_pass1_FAST, LHC17p_pass1_CENT_woSDD, LHC17q_pass1_FAST, LHC17q_pass1_CENT_woSDD).

2.1 Monte Carlo productions

For this analysis the Monte Carlo production LHC18a4a2_g3_fast was used, anchored to the 2017 pp data taking periods LHC17p and LHC17q and the FAST production. The FAST production simulation is used to correct the data sample, which is the merged: FAST+CENT_woSDD, assuming that efficiencies and detector response are the same for both. The simulations uses PYTHIA6 with the Perugia2011 tune as particle generator at $\sqrt{s} = 5.02$ TeV. The charm content has been enhanced by requesting a $c\bar{c}$ in 50% of the events and a $b\bar{b}$ in the remaining half. Furthermore, all D mesons are forced to decay hadronically. This MC production is used to compute the D-meson efficiency with jets, acceptance corrections and a response matrix of D-tagged jets with prompt and non-prompt D⁰ : $c, b \rightarrow D^0$.

2.1.1 D^0 -tagged jets

Results shown in this Note come from the LEGO trains HFCJ_pp_MC:

Reconstruction efficiency and response matrices: LEGO train 414 (jet- p_T production) and 634, 642 ($z_{||}$ distribution with $R = 0.3, 0.4$)

For $R = 0.3$ jet p_T cross-section cut-variation studies: LEGO train 414, 443, 440, 438, 431, 479

[and for HFCJ_pp: 365, 405, 401, 399, 393, 439 respectively]

Jet Energy Scale systematic studies: LEGO trains 474.

3 D-Meson Selection

The D mesons were reconstructed through their hadronic decay channels [1]:

$$D^0(\bar{D}^0) \rightarrow K^\pm + \pi^\mp, \text{BR} = 3.89 \pm 0.04\%$$

The selection strategy is based on the topological displacement of the secondary vertex from the primary vertex due to their relatively large lifetime.

The candidate vertices are read from the AOD friend chain `AliAOD.VertexingHF.root`. A list of topological and kinematic cuts applied for D^0 in pp collisions at $\sqrt{s} = 5.02$ TeV. The same quality track selection on the decay products used for the D-meson spectra analysis of the same datasets has been used in this analysis. For the final jet spectrum we will apply $p_{T,D} > 3$ GeV/c on the D mesons. The accepted $|y_D|$ range is p_T -dependent, with the upper limit growing from 0.5 to 0.8 at $p_T = 5$ GeV/c.

Table 1: D^0 cuts for pp collisions at $\sqrt{s} = 5.02$ TeV.

p_{T,D^0} (GeV/c)	0.5–1	1–2	2–3	3–4	4–5	5–6	6–7	7–8	8–10	10–12	12–16	16–24	24–36
ΔM_{D^0} (GeV/c ²)	0.4	0.4	0.4	0.4	0.4	0.4	0.4	0.4	0.4	0.4	0.4	0.4	0.4
DCA (cm)	0.03	0.03	0.03	0.03	0.03	0.03	0.03	0.03	0.03	0.03	0.03	0.03	0.03
$\cos(\theta^*)$	0.8	0.8	0.8	0.8	0.8	0.8	0.8	0.8	0.9	0.9	1	1	1
$p_{T,K}$ (GeV/c)	0.5	0.5	0.7	0.7	0.7	0.7	0.7	0.7	0.7	0.7	0.7	0.7	0.7
$p_{T,\pi}$ (GeV/c)	0.5	0.5	0.7	0.7	0.7	0.7	0.7	0.7	0.7	0.7	0.7	0.7	0.7
d_0^K (cm)	0.1	0.1	0.1	0.1	0.1	0.1	0.1	0.1	0.1	0.1	0.1	0.1	0.1
d_0^π (cm)	0.1	0.1	0.1	0.1	0.1	0.1	0.1	0.1	0.1	0.1	0.1	0.1	0.1
$d_0^K \cdot d_0^\pi$ (10 ⁻⁴ cm ²)	-5	-3.5	-3	-3	-1.5	-1	-0.8	-0.8	-0.5	-0.5	1	1	1
$\cos(\theta_{\text{point}})$	0.95	0.95	0.95	0.95	0.95	0.95	0.95	0.95	0.95	0.95	0.95	0.90	0.90
$L_{xy}/\sigma_{L_{xy}}$ (cm)	5	5	5	5	5	4	4	4	3	3	3	3	3

3.1 Particle Identification

The Particle Identification (PID) of pions and kaons was performed using the information of the specific energy loss in the TPC and the time of flight provided by the TOF detector. In order to identify a track as a pion or a kaon its TPC dE/dx and/or time-of-flight were required to be within 3σ of the expected values. Tracks with no TOF information were identified using only the TPC. When PID is inconclusive and neither the pion nor the kaon hypothesis can be excluded, tracks compatible with both the hypotheses were retained for analysis.

As a result, for the decay $D^0(\bar{D}^0) \rightarrow K^\pm + \pi^\mp$, the $(K\pi)$ pair is counted twice with the two possible mass assignments. If the pair does not correspond to a real D meson, it would add two background entries in the invariant mass histogram, else it counts a signal plus a background entry. The misidentification rate (i.e. cases in which the wrong mass hypothesis is accepted while the correct one is rejected) is very small. In this case the signal D meson is lost and the entry contributes to the background in the invariant mass histogram. In the following D^0 analysis, D^0 reflections are defined as pion-kaon pairs that come from the decay of a real D^0 , but with the reflected mass hypothesis.

4 Jet Reconstruction

The FASTJET[2] package was used to reconstruct the jets. In particular, the anti- k_T algorithm [3] was employed to reconstruct signal jets. This algorithm is infrared-safe (not sensitive to low energy radiations) and collinear-safe (not sensitive to collinear particle splitting). Resolution parameters of $R=0.3, 0.4$ were used for D⁰ in pp. For this analysis, only charged tracks are used to reconstruct the jets (*charged jets*). The underlying event is not subtracted.

The set of tracks given as input to the jet finder has the D-meson daughters replaced by the 4-momentum of the D-meson candidate (sum of the 4-momenta of the daughters). The procedure is repeated independently for each D-meson candidate in each event, i.e. each candidate is treated as if it were the only one in the event, then (if there is more than one candidate) the procedure is repeated for each candidate one by one. This is done because two (or even more) candidates can share the same daughter.

4.1 Jet Selection

Tracks with $p_T > 0.15$ GeV/ c and $|\eta| < 0.9$ were included in the jet finding. Reconstructed jets with the axis not satisfying $|\eta_{\text{jet}}| < 0.9 - R$ were rejected.

5 Raw Yield Extraction

The signal in the D⁰ invariant mass distribution is fit with a Gaussian distribution for the signal and a power function for the background:

$$f(m) = Ce^{-\left(\frac{m-m_0}{2\sigma}\right)^2} + am^b, \quad (1)$$

where m is the invariant mass, a, b, C, m_0, σ are free parameters.

Side-band subtraction in D-meson p_T bins : in the case of D⁰, the signal region is defined as 2σ around the peak position, and the side-band region is between 4σ and 9σ away from the D⁰ peak from both sides. In addition, the “reflection” templates are extracted from the charm-enhanced MC production.

5.1 Side-Band Subtraction: jet p_T cross-section, $R = 0.3$

The D-meson candidates in the signal region are used to build a jet p_T distribution, which comprises both signal and background D-meson candidates. Another jet p_T distribution is built using candidates with invariant mass that is the side-band regions: 4σ and 9σ from the peak. The normalization is done using the information of the fit integrating the background function inside the signal area. This is done separately and independently for each $p_{T,D}$ bin.

The invariant mass distributions in bins of D-meson p_T are shown in Fig. 1 where the signal region is shown as the red shaded area, and the background region is depicted as the blue shaded area. Also shown in Fig. 1 are reflections for D⁰ in green, and their ratio over signal is shown in Fig. 2 right. Figure 2 shows a summary of the raw signal extraction: yield, relative statistical uncertainty, signal / background ratio and significance.

The raw jet p_T distributions are shown in Fig. 3, along with the jet p_T distributions for the background region. Then the background distributions are subtracted from the signal distributions and raw jet p_T distributions are obtained in each D p_T bin, as it is shown also in Fig. 3. Figure 4 shows the sum of the jet p_T distributions without a correction for the D-meson-jet efficiency.

In order to obtain the final jet p_T spectrum, the distributions in each D p_T bin need to be corrected for the D efficiency and finally summed up. The corrections will be discussed in Section 6.1.

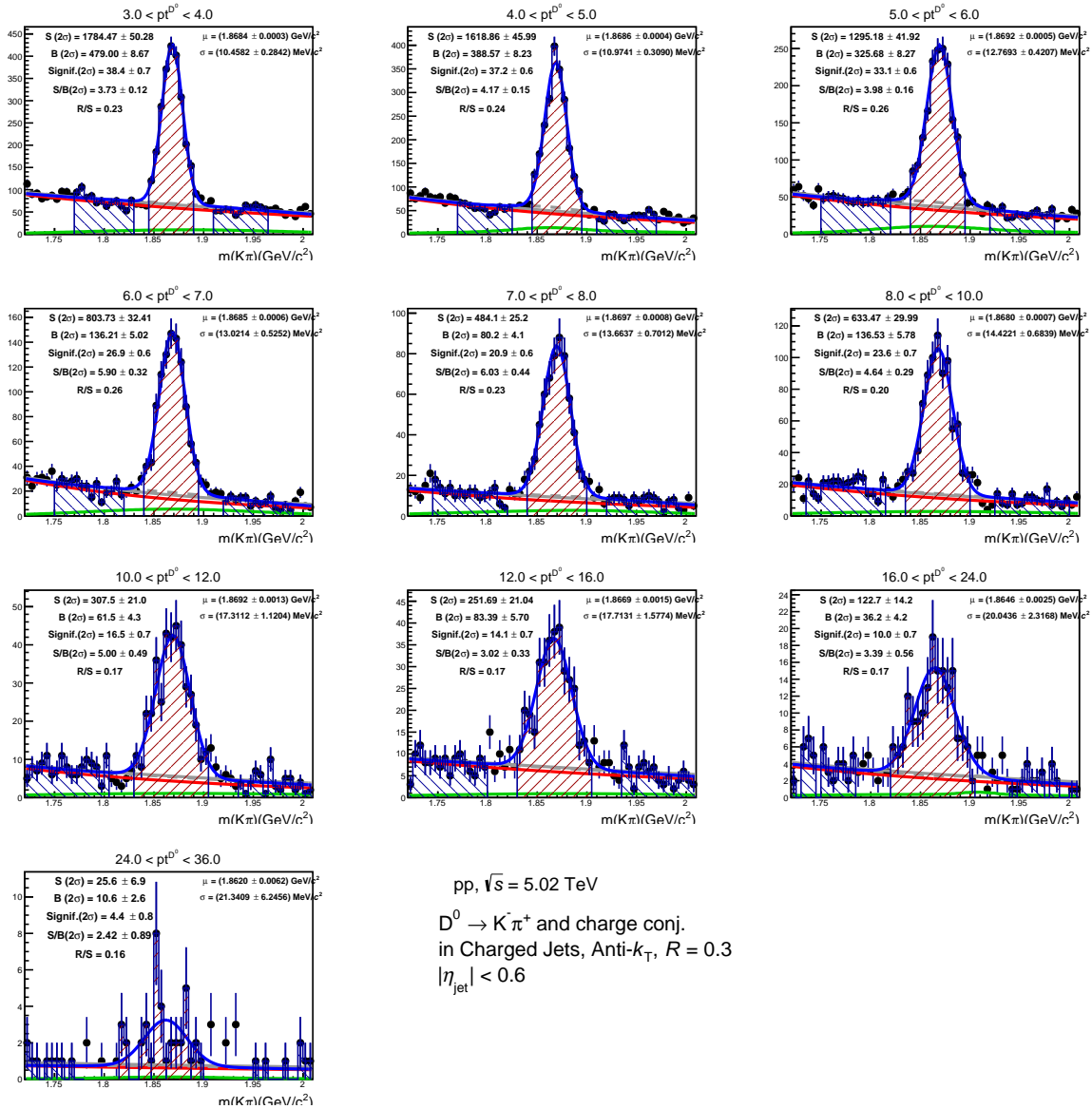


Fig. 1: D^0 -jet signal extraction in bins of jet transverse momentum in pp collisions at $\sqrt{s} = 5.02$ TeV (raw yields). D mesons are required to have $p_T > 3$ GeV/c. Reflections shown by green curve add with the combinatorial background (red curve) to give the overall background in grey.

5.2 Side-Band Subtraction: $z_{||,\text{ch}}$ distribution, $R = 0.3, 0.4$

We extract the $z_{||,\text{ch}}$ distribution for different intervals of jet p_T : 5-7, 7-10, 10-15 and 15-50 GeV/c. For any given jet p_T interval, the D-meson candidates in the signal region are used to build a $z_{||,\text{ch}}$ distribution, which comprises both signal and background D-meson candidates. Another $z_{||,\text{ch}}$ distribution is built using candidates with invariant mass in the side-band regions: 4σ and 9σ from the peak. The normalization is done using the information of the fit integrating the background function inside the signal area. This is done separately and independently for each $p_{T,D}$ bin.

5.2.1 $R = 0.3$

For $5 < \text{jet } p_T < 7$ GeV/c, the invariant mass distributions in bins of D-meson p_T are shown in fig. 5 where the signal region is shown as the red shaded area, and the background region is depicted as the blue shaded area. Figure 6 shows a summary of the raw signal extraction: yield, relative statistical

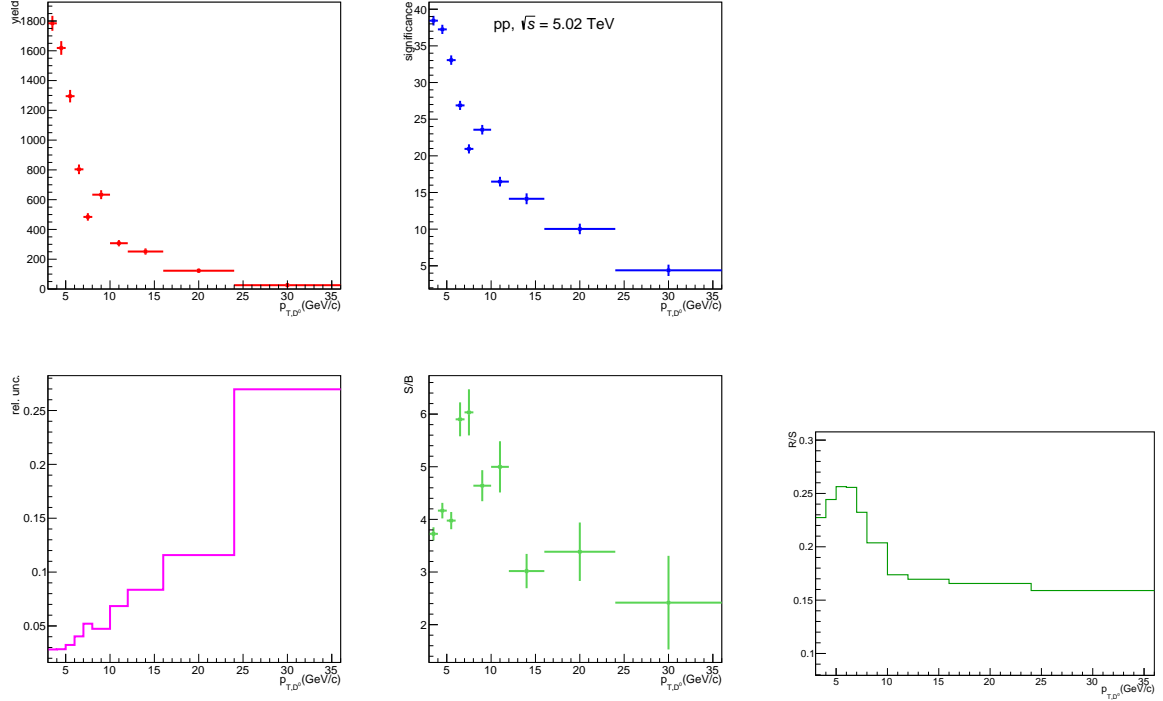


Fig. 2: Left: D⁰-jet raw signal extraction: raw yields, relative statistical uncertainties, significance and S/B ratio in D⁰ p_T bins, in pp collisions at $\sqrt{s} = 5.02$ TeV for $p_{T,D} > 3$ GeV/ c with the Side Band method.

Right: D⁰-jet raw signal extraction, reflections over signal ratio, in pp collisions at $\sqrt{s} = 5.02$ TeV for $p_{T,D} > 3$ GeV/ c with the Side Band method.

uncertainty, signal / background ratio and significance. The raw $z_{||, \text{ch jet}}$ distributions are shown in fig. 7, along with the $z_{||, \text{ch jet}}$ distributions for the background region. Then the background distributions are subtracted from the signal distributions and raw $z_{||, \text{ch jet}}$ distributions are obtained in each D p_T bin, as it is shown also in fig. 7. Figure 8 shows the sum of the $z_{||, \text{ch jet}}$ distributions without a correction for the D-meson-jet efficiency. In order to obtain the final $z_{||, \text{ch jet}}$ spectrum, the distributions in each D p_T bin need to be corrected for the D efficiency and are then summed up. The corrections will be discussed in Section 6.1.

Similarly for $7 < \text{jet } p_T < 10$ GeV/ c , we have figures 9, 10, 11 and 12.

For $10 < \text{jet } p_T < 15$ GeV/ c , we have figures 13, 14, 15 and 16.

For $15 < \text{jet } p_T < 50$ GeV/ c , the sigma of the last bin was bound within 10% of its corresponding MC value to get better fit results. Our figures are 17, 18, 19 and 20. This step was also done for $R = 0.4$.

A comparison between invariant mass fits with free sigma, sigma bound within 10% of MC value for the last bin, sigma bound within 10% and 20% of MC values for all bins in this jet- p_T interval can be seen in figures 37 and 38. Particular difference between free sigma fit and last bin bound within 10% MC sigma fit is observed for $R = 0.4$.

5.2.2 $R = 0.4$

For jet radius of $R = 0.4$ (in $\eta - \phi$ plane), the corresponding figures for different jet p_T intervals are:

– 5-7 GeV/ c : 21, 22, 23 and 24.

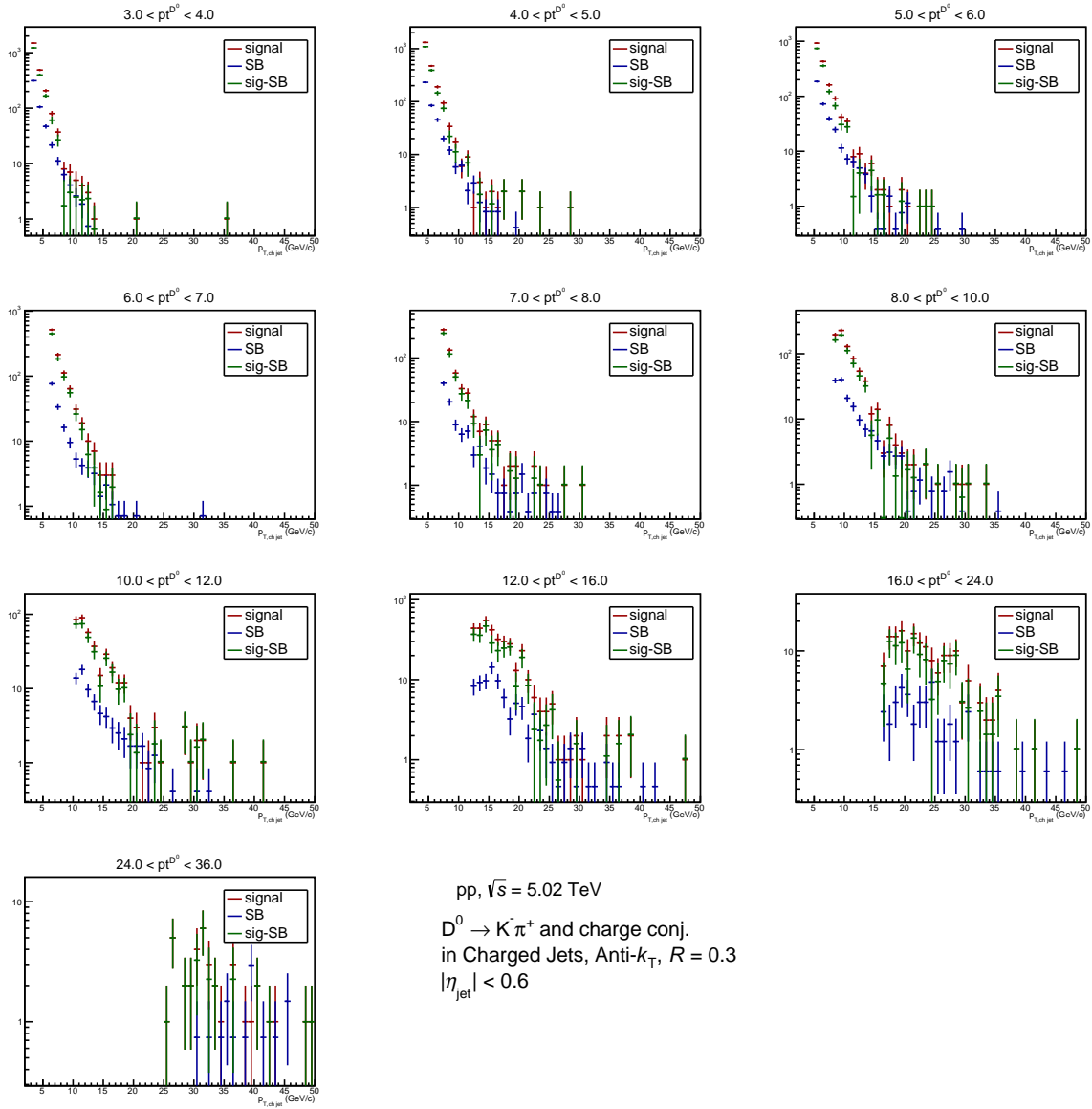


Fig. 3: Raw jet p_T distributions in bins of D^0 transverse momentum in pp collisions at $\sqrt{s} = 5.02$ TeV.

- 7-10 GeV/ c : 25, 26, 27 and 28.
- 10-15 GeV/ c : 29, 30, 31 and 32.
- 15-50 GeV/ c : 33, 34, 35 and 36.

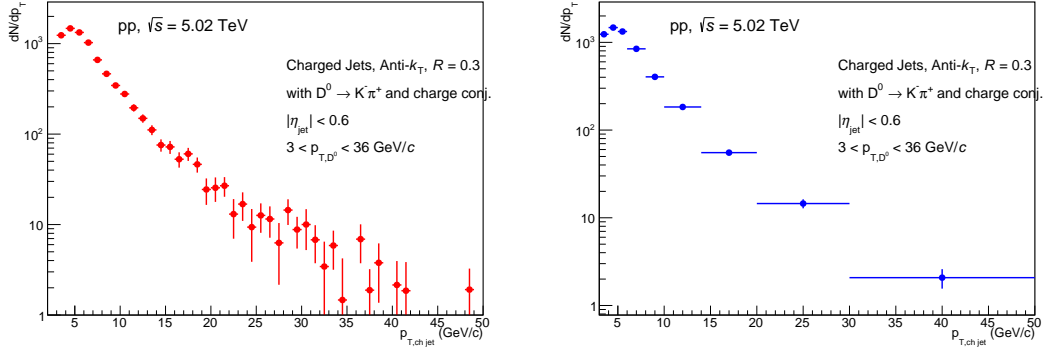


Fig. 4: Total raw jet p_T distributions (left) in pp collisions at $\sqrt{s} = 5.02 \text{ TeV}$, obtained summing together all D p_T bins without an efficiency correction. The same after rebinning (right).

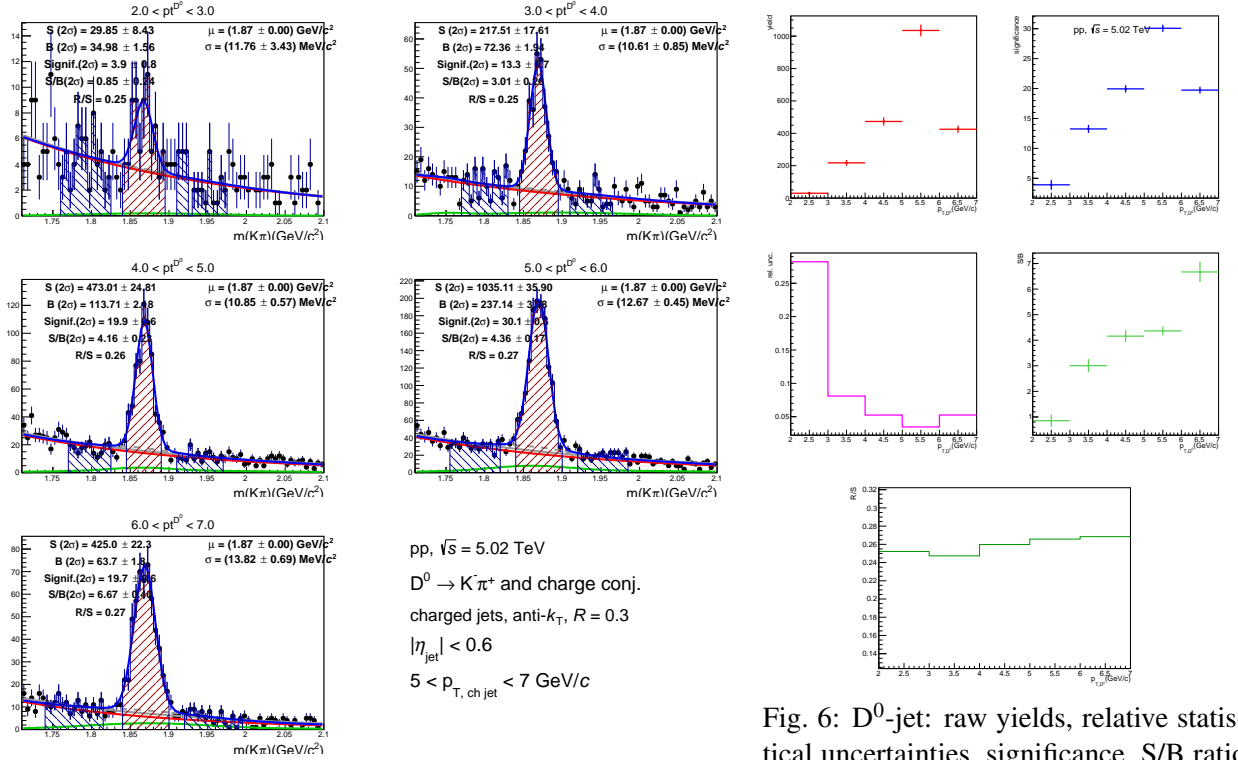


Fig. 5: D⁰-jet signal extraction in bins of D transverse momentum and R/S ratio in D⁰ p_T bins, in pp collisions at $\sqrt{s} = 5.02 \text{ TeV}$ (raw yields). D mesons are required to have $p_T > 2 \text{ GeV/c}$. Jet p_T is in 5-7 GeV/c.

Fig. 6: D⁰-jet: raw yields, relative statistical uncertainties, significance, S/B ratio in D⁰ p_T bins, in pp collisions at $\sqrt{s} = 5.02 \text{ TeV}$ for $5 < \text{jet } p_T < 7 \text{ GeV/c}$ with the Side Band method.

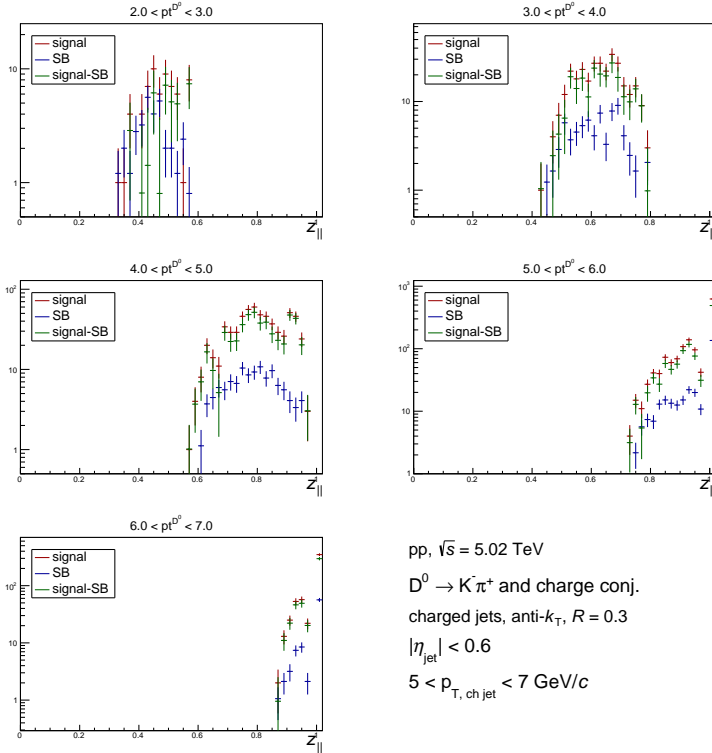


Fig. 7: Raw $z_{||}$ distributions in bins of D^0 transverse momentum in pp collisions at $\sqrt{s} = 5.02$ TeV.

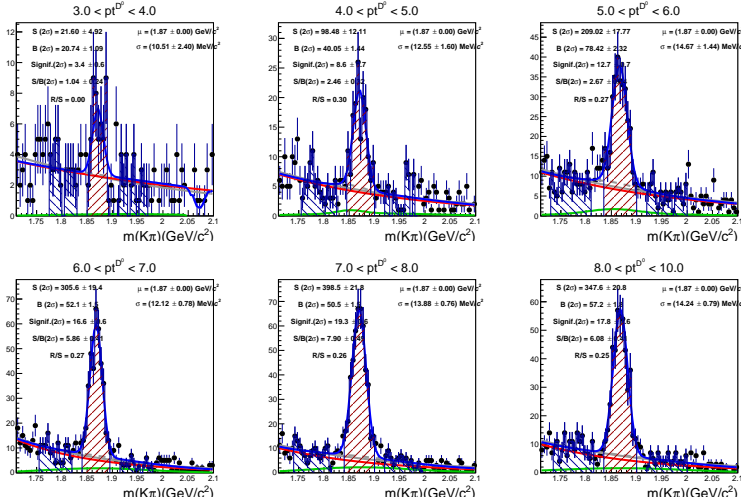


Fig. 9: D^0 -jet signal extraction in bins of D transverse momentum and R/S ratio in D^0 p_T bins, in pp collisions at $\sqrt{s} = 5.02$ TeV (raw yields). D mesons are required to have $p_T > 3$ GeV/c. Jet p_T is in 7-10 GeV/c.

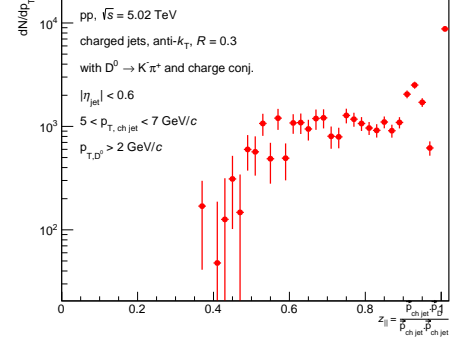


Fig. 8: Total raw $z_{||}$ distributions in pp collisions at $\sqrt{s} = 5.02$ TeV, obtained summing together all D p_T bins without an efficiency correction for $5 < \text{jet } p_T < 7$ GeV/c.

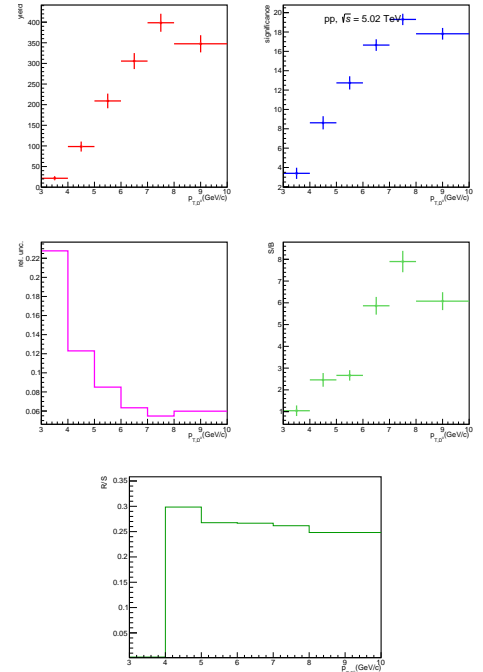
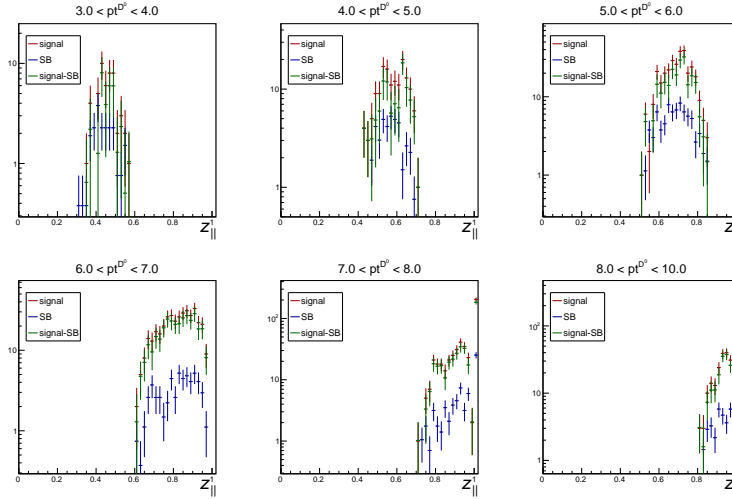


Fig. 10: D^0 -jet: raw yields, relative statistical uncertainties, significance, S/B ratio in D^0 p_T bins, in pp collisions at $\sqrt{s} = 5.02$ TeV for $7 < \text{jet } p_T < 10$ GeV/c with the Side Band method.



pp, $\sqrt{s} = 5.02$ TeV
 $D^0 \rightarrow K^+ \pi^-$ and charge conj.
 charged jets, anti- k_T , $R = 0.3$
 $|\eta_{\text{jet}}| < 0.6$
 $7 < p_{T, \text{ch jet}} < 10$ GeV/c

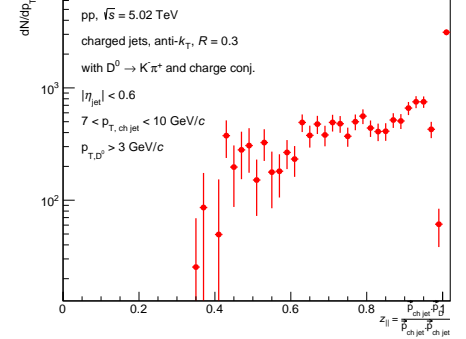
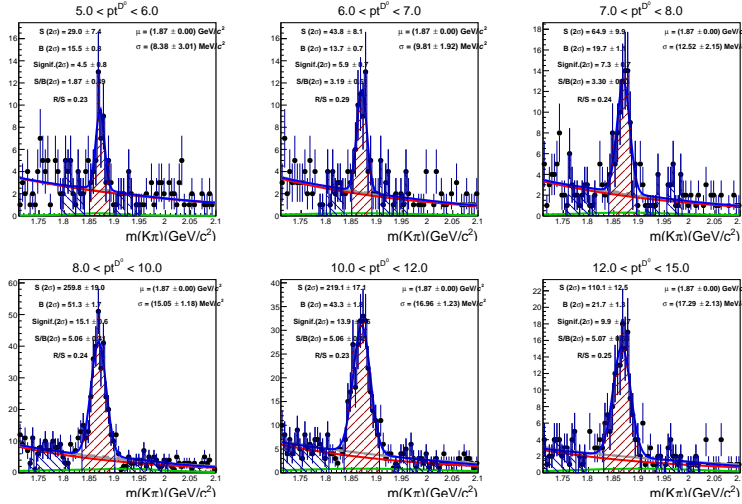


Fig. 12: Total raw $z_{||}$ distributions in pp collisions at $\sqrt{s} = 5.02$ TeV, obtained summing together all D p_T bins without an efficiency correction for $7 < \text{jet } p_T < 10$ GeV/c.

Fig. 11: Raw $z_{||}$ distributions in bins of D⁰ transverse momentum in pp collisions at $\sqrt{s} = 5.02$ TeV.



pp, $\sqrt{s} = 5.02$ TeV
 $D^0 \rightarrow K^+ \pi^-$ and charge conj.
 charged jets, anti- k_T , $R = 0.3$
 $|\eta_{\text{jet}}| < 0.6$
 $10 < p_{T, \text{ch jet}} < 15$ GeV/c

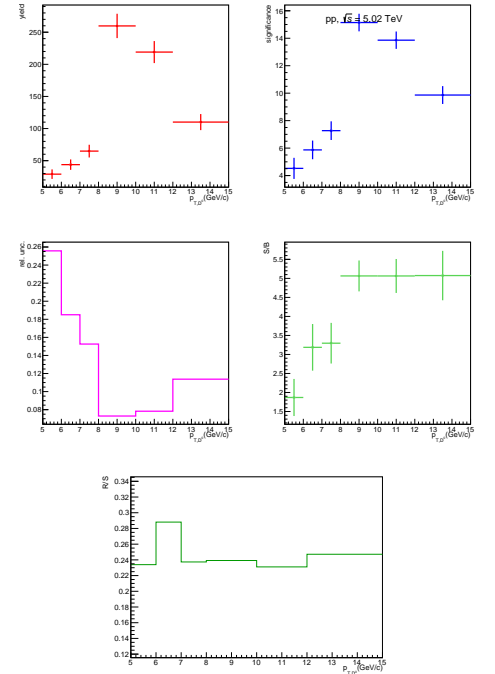
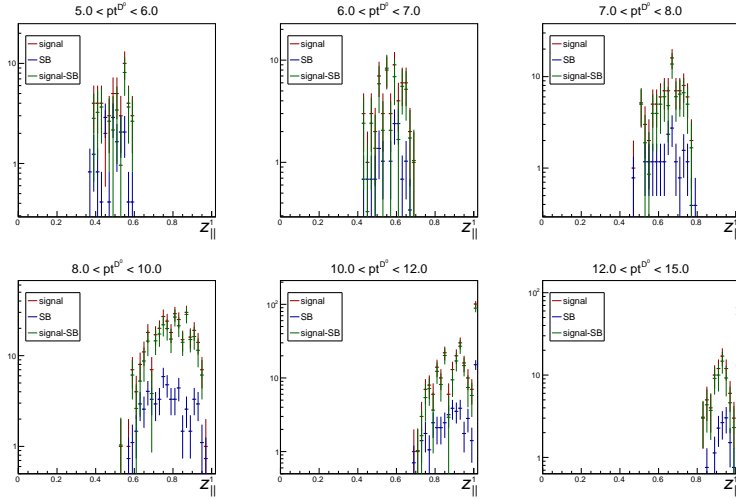


Fig. 14: D⁰-jet: raw yields, relative statistical uncertainties, significance, S/B ratio in D⁰ p_T bins, in pp collisions at $\sqrt{s} = 5.02$ TeV (raw yields). D mesons are reconstructed at $\sqrt{s} = 5.02$ TeV for $10 < \text{jet } p_T < 15$ GeV/c with the Side Band method.

Fig. 13: D⁰-jet signal extraction in bins of D transverse momentum and R/S ratio in D⁰ p_T bins, in pp collisions at $\sqrt{s} = 5.02$ TeV (raw yields). D mesons are reconstructed at $\sqrt{s} = 5.02$ TeV for $10 < \text{jet } p_T < 15$ GeV/c. Jet p_T is in 10-15 GeV/c.



pp, $\sqrt{s} = 5.02$ TeV
 $D^0 \rightarrow K^-\pi^+$ and charge conj
 charged jets, anti- k_T , $R = 0.3$
 $|\eta_{\text{jet}}| < 0.6$
 $10 < p_{T, \text{ch jet}} < 15$ GeV/c

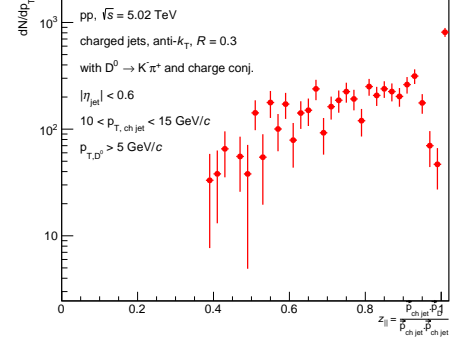
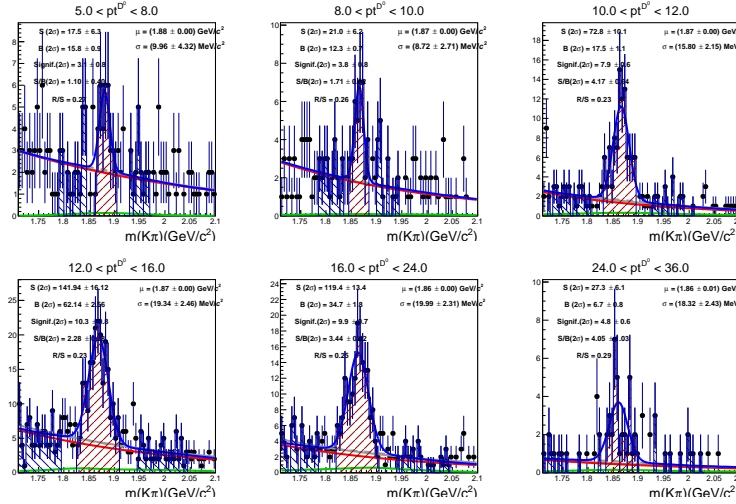


Fig. 16: Total raw $z_{||}$ distributions in pp collisions at $\sqrt{s} = 5.02$ TeV, obtained summing together all D p_T bins without an efficiency correction for $10 < \text{jet } p_T < 15$ GeV/c.

Fig. 15: Raw $z_{||}$ distributions in bins of D^0 transverse momentum in pp collisions at $\sqrt{s} = 5.02$ TeV for $10 < \text{jet } p_T < 15$ GeV/c.



pp, $\sqrt{s} = 5.02$ TeV
 $D^0 \rightarrow K^-\pi^+$ and charge conj
 charged jets, anti- k_T , $R = 0.3$
 $|\eta_{\text{jet}}| < 0.6$
 $15 < p_{T, \text{ch jet}} < 50$ GeV/c

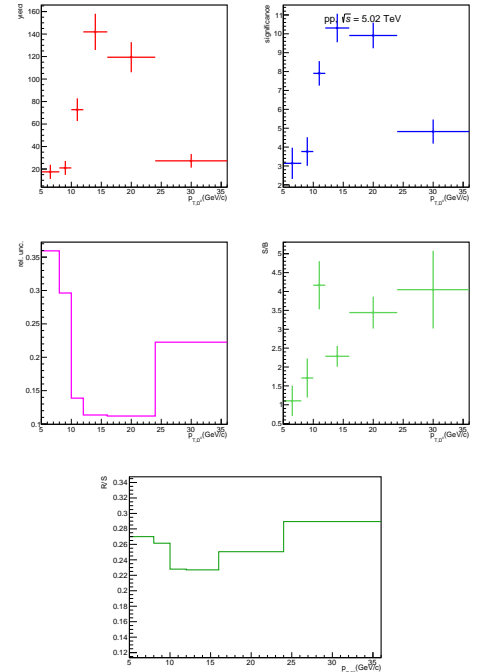
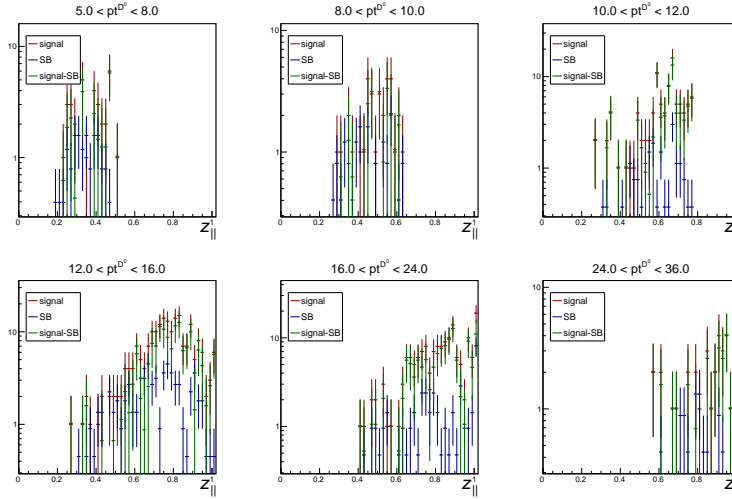


Fig. 18: D^0 -jet: raw yields, relative statistical uncertainties, significance, S/B ratio in D^0 p_T bins, in pp collisions at $\sqrt{s} = 5.02$ TeV (raw yields). D mesons are resonances at $\sqrt{s} = 5.02$ TeV for $15 < \text{jet } p_T$ required to have $p_T > 5$ GeV/c. Jet p_T is in 15-50 GeV/c.

Fig. 17: D^0 -jet signal extraction in bins of D transverse momentum in pp collisions at $\sqrt{s} = 5.02$ TeV (raw yields). D mesons are resonances at $\sqrt{s} = 5.02$ TeV for $15 < \text{jet } p_T$ required to have $p_T > 5$ GeV/c. Jet p_T is in 15-50 GeV/c.



pp, $\sqrt{s} = 5.02$ TeV
 $D^0 \rightarrow K^+ \pi^-$ and charge conj.
 charged jets, anti- k_T , $R = 0.3$
 $|\eta_{\text{jet}}| < 0.6$
 $15 < p_{T, \text{ch jet}} < 50$ GeV/c

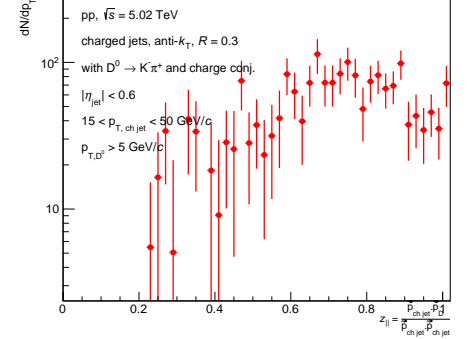
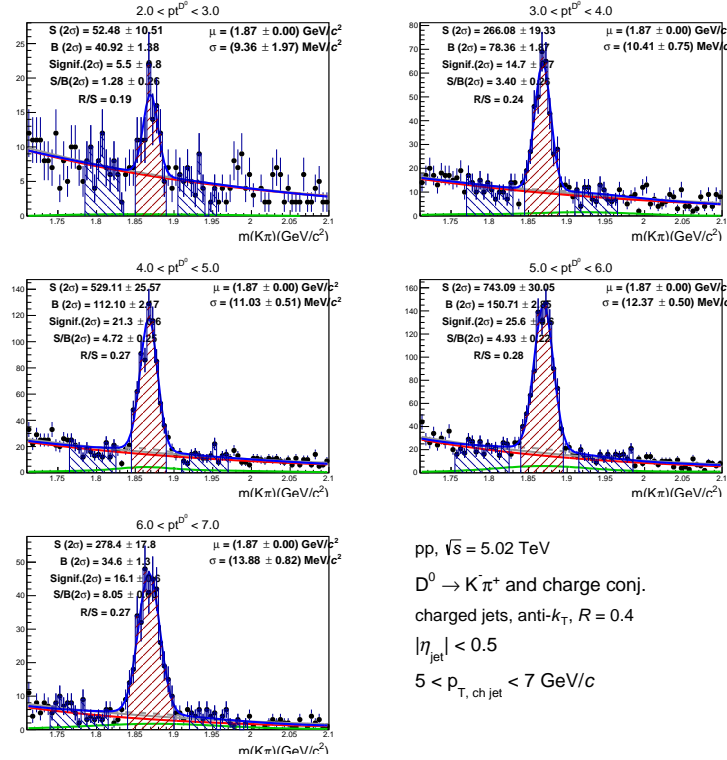


Fig. 20: Total raw $z_{||}$ distributions in pp collisions at $\sqrt{s} = 5.02$ TeV, obtained summing together all D p_T bins without an efficiency correction for $15 < \text{jet } p_T < 50$ GeV/c.

Fig. 19: Raw $z_{||}$ distributions in bins of D⁰ transverse momentum in pp collisions at $\sqrt{s} = 5.02$ TeV for $15 < \text{jet } p_T < 50$ GeV/c.



pp, $\sqrt{s} = 5.02$ TeV
 $D^0 \rightarrow K^+ \pi^-$ and charge conj.
 charged jets, anti- k_T , $R = 0.4$
 $|\eta_{\text{jet}}| < 0.5$
 $5 < p_{T, \text{ch jet}} < 7$ GeV/c

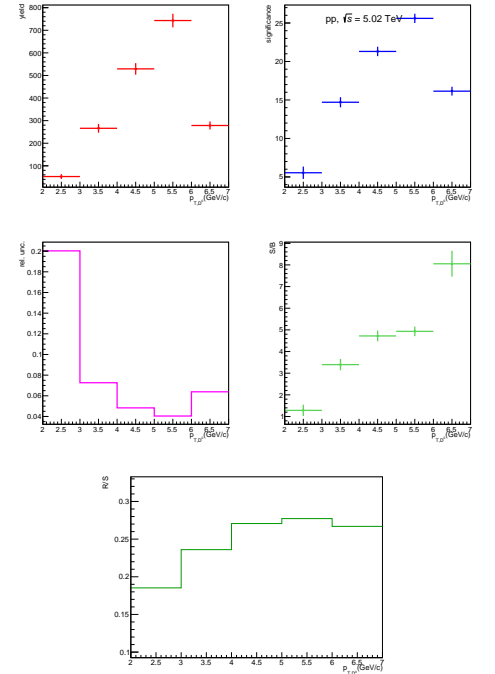


Fig. 22: D⁰-jet: raw yields, relative statistical uncertainties, significance, S/B ratio in D⁰ p_T bins, in pp collisions at $\sqrt{s} = 5.02$ TeV (raw yields). D mesons are required to have $p_T > 2$ GeV/c. Jet p_T is in 5-7 GeV/c with the Side Band method.

Fig. 21: D⁰-jet signal extraction in bins of D transverse momentum and R/S ratio in D⁰ p_T bins, in pp collisions at $\sqrt{s} = 5.02$ TeV (raw yields). D mesons are required to have $p_T > 2$ GeV/c. Jet p_T is in 5-7 GeV/c.

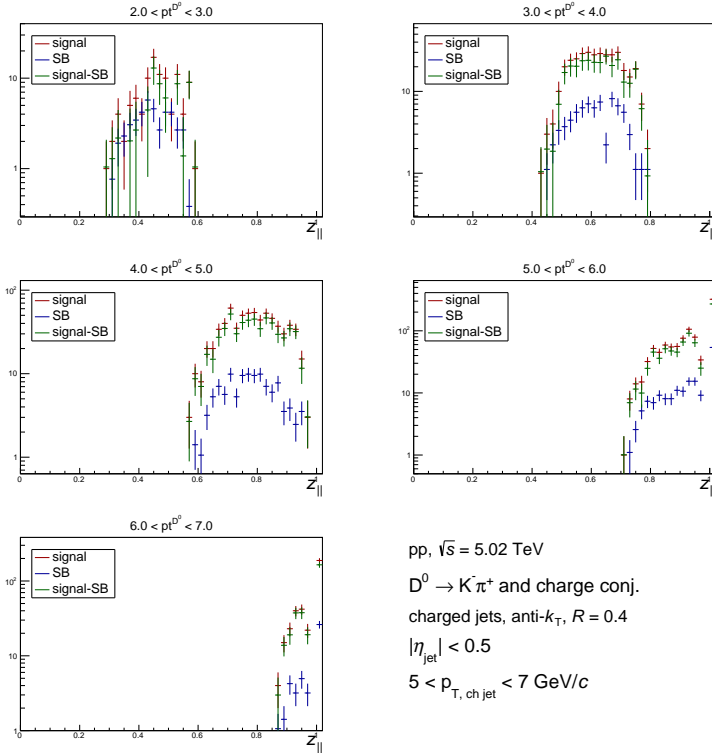


Fig. 23: Raw $z_{||}$ distributions in bins of D^0 transverse momentum in pp collisions at $\sqrt{s} = 5.02$ TeV.

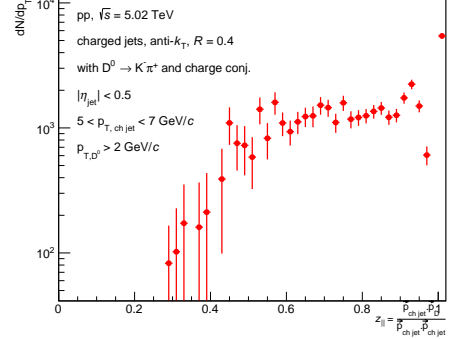


Fig. 24: Total raw $z_{||}$ distributions in pp collisions at $\sqrt{s} = 5.02$ TeV, obtained summing together all D p_T bins without an efficiency correction for $5 < \text{jet } p_T < 7$ GeV/c.

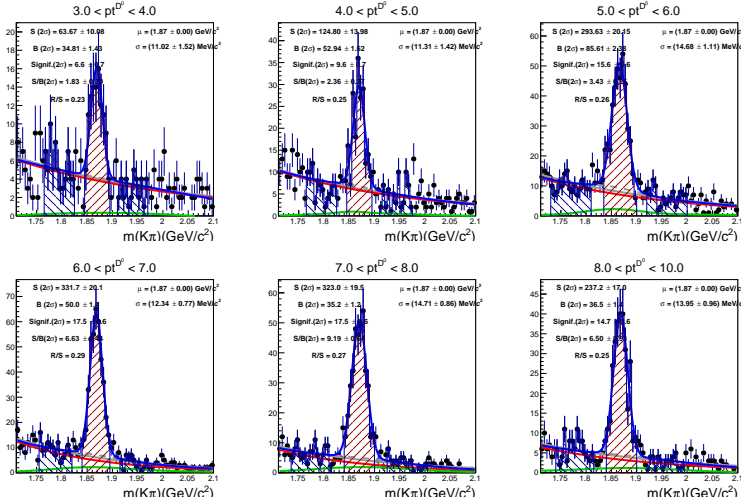


Fig. 25: D^0 -jet signal extraction in bins of D transverse momentum and R/S ratio in D^0 p_T bins, in pp collisions at $\sqrt{s} = 5.02$ TeV (raw yields). D mesons are selected at $\sqrt{s} = 5.02$ TeV for $7 < \text{jet } p_T$ required to have $p_T > 3$ GeV/c. Jet p_T is in 7-10 GeV/c.

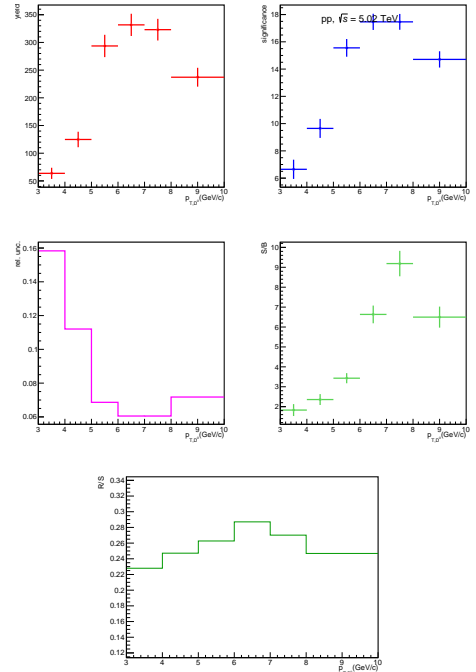
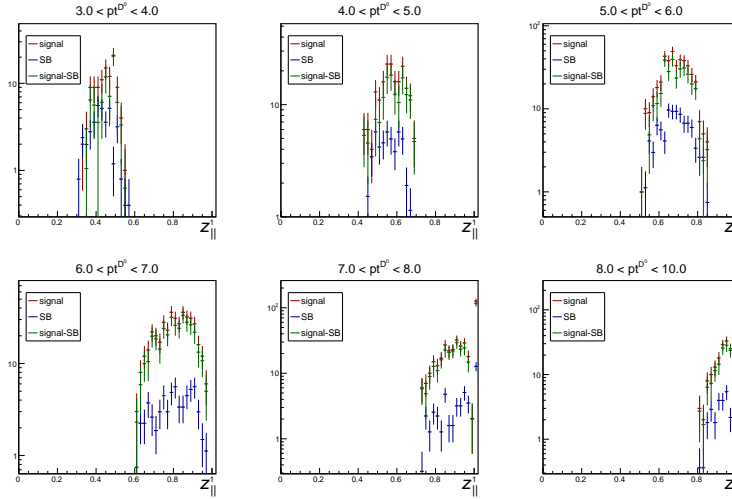


Fig. 26: D^0 -jet: raw yields, relative statistical uncertainties, significance, S/B ratio in D^0 p_T bins, in pp collisions at $\sqrt{s} = 5.02$ TeV for $7 < \text{jet } p_T$ required to have $p_T > 3$ GeV/c. Jet p_T is in 7-10 GeV/c with the Side Band method.



pp, $\sqrt{s} = 5.02$ TeV
 $D^0 \rightarrow K^-\pi^+$ and charge conj
 charged jets, anti- k_T , $R = 0.4$
 $|\eta_{\text{jet}}| < 0.5$
 $7 < p_{T, \text{ch jet}} < 10$ GeV/c

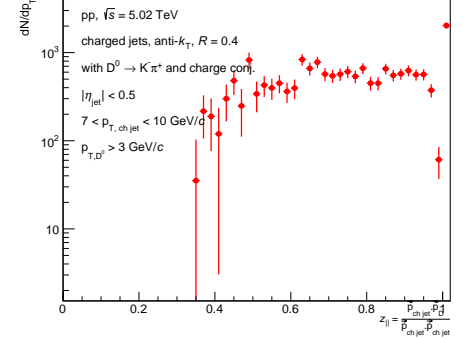
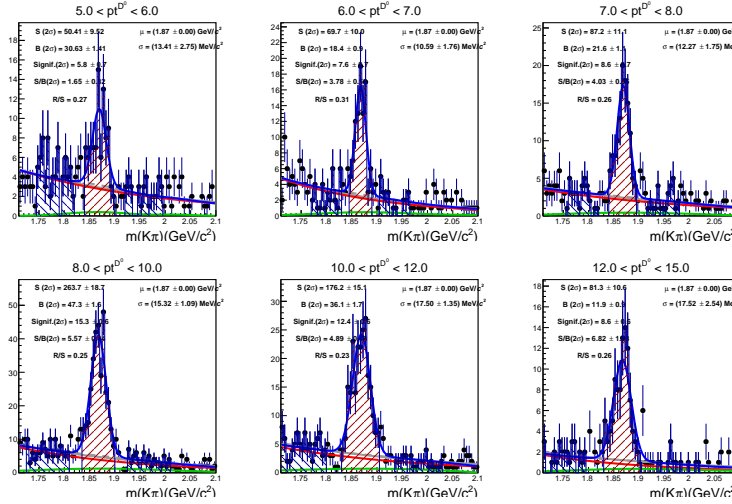


Fig. 28: Total raw $z_{||}$ distributions in pp collisions at $\sqrt{s} = 5.02$ TeV, obtained summing together all D p_T bins without an efficiency correction for $7 < \text{jet } p_T < 10$ GeV/c.

Fig. 27: Raw $z_{||}$ distributions in bins of D⁰ transverse momentum in pp collisions at $\sqrt{s} = 5.02$ TeV.



pp, $\sqrt{s} = 5.02$ TeV
 $D^0 \rightarrow K^-\pi^+$ and charge conj
 charged jets, anti- k_T , $R = 0.4$
 $|\eta_{\text{jet}}| < 0.5$
 $10 < p_{T, \text{ch jet}} < 15$ GeV/c

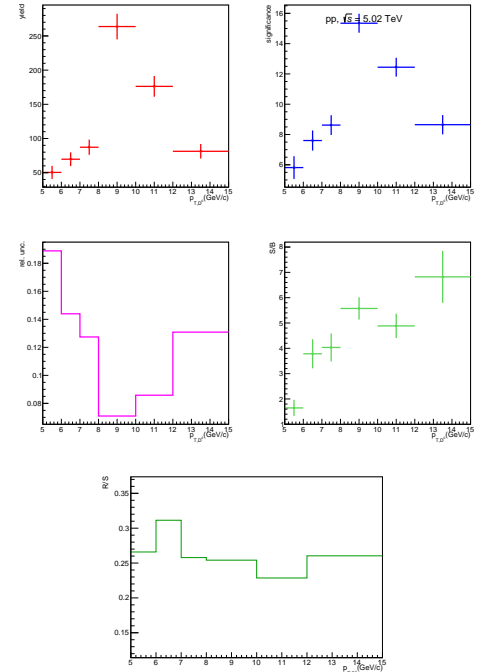
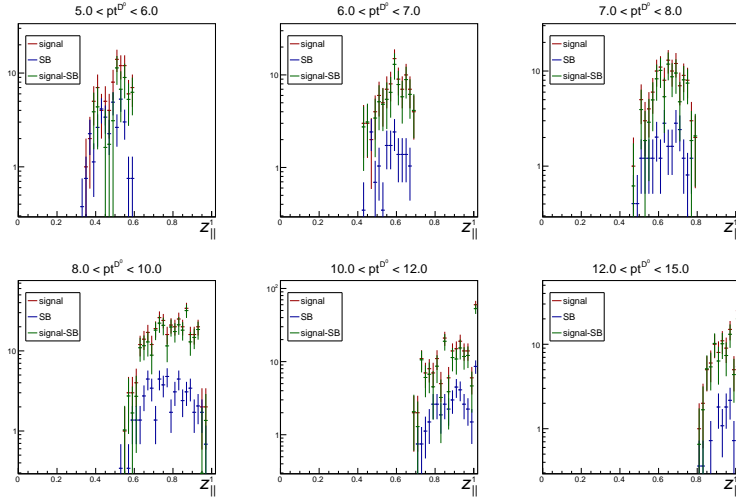


Fig. 30: D⁰-jet: raw yields, relative statistical uncertainties, significance, S/B ratio in D⁰ p_T bins, in pp collisions at $\sqrt{s} = 5.02$ TeV (raw yields). D mesons are required to have $p_T > 5$ GeV/c. Jet p_T is in 10-15 GeV/c.

Fig. 29: D⁰-jet signal extraction in bins of D transverse momentum and R/S ratio in D⁰ p_T bins, in pp collisions at $\sqrt{s} = 5.02$ TeV (raw yields). D mesons are required to have $p_T > 5$ GeV/c. Jet p_T is in 10-15 GeV/c.



pp, $\sqrt{s} = 5.02$ TeV
 $D^0 \rightarrow K^-\pi^+$ and charge conj
 charged jets, anti- k_T , $R = 0.4$
 $|\eta_{\text{jet}}| < 0.5$
 $10 < p_{T, \text{ch jet}} < 15$ GeV/c

Fig. 31: Raw $z_{||}$ distributions in bins of D^0 transverse momentum in pp collisions at $\sqrt{s} = 5.02$ TeV for $10 < \text{jet } p_T < 15$ GeV/c.

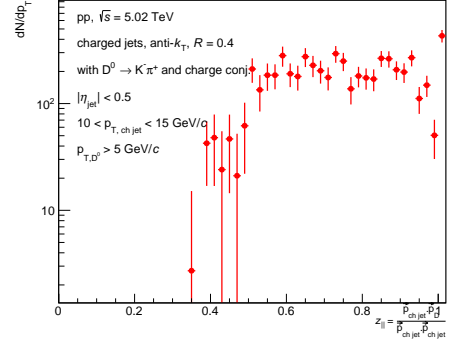
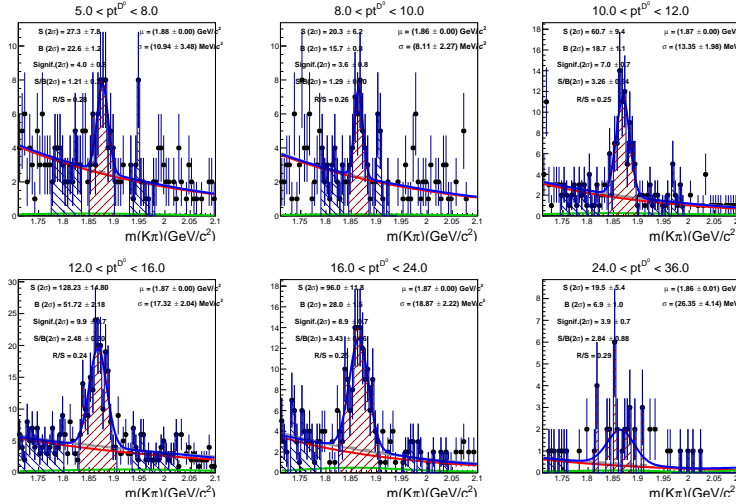


Fig. 32: Total raw $z_{||}$ distributions in pp collisions at $\sqrt{s} = 5.02$ TeV, obtained summing together all D p_T bins without an efficiency correction for $10 < \text{jet } p_T < 15$ GeV/c.



pp, $\sqrt{s} = 5.02$ TeV
 $D^0 \rightarrow K^-\pi^+$ and charge conj
 charged jets, anti- k_T , $R = 0.4$
 $|\eta_{\text{jet}}| < 0.5$
 $15 < p_{T, \text{ch jet}} < 50$ GeV/c

Fig. 33: D^0 -jet signal extraction in bins of D transverse momentum in pp collisions at $\sqrt{s} = 5.02$ TeV (raw yields). D mesons are required to have $p_T > 5$ GeV/c. Jet p_T is in 15-50 GeV/c.

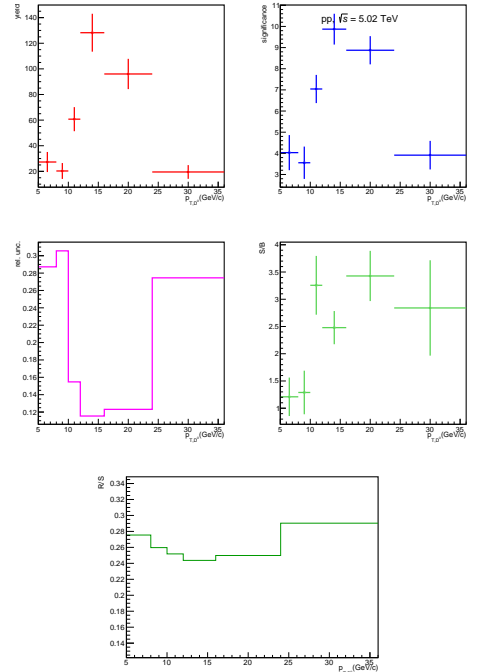
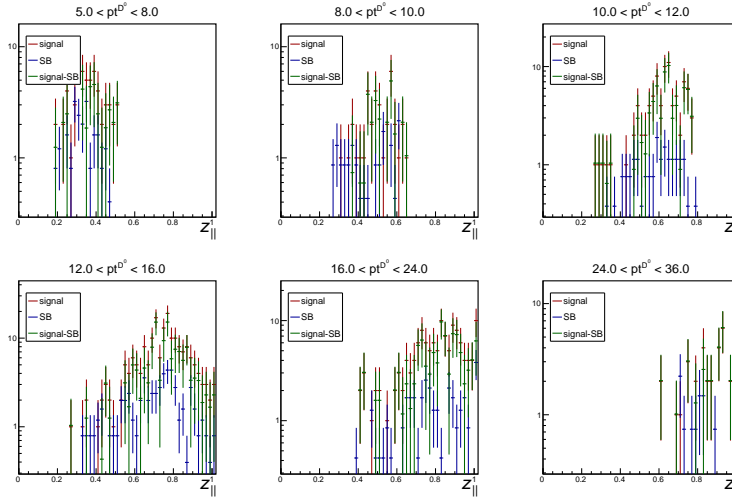


Fig. 34: D^0 -jet: raw yields, relative statistical uncertainties, significance, S/B ratio in D^0 p_T bins, in pp collisions at $\sqrt{s} = 5.02$ TeV for $15 < \text{jet } p_T < 50$ GeV/c with the Side Band method.



pp, $\sqrt{s} = 5.02$ TeV
 $D^0 \rightarrow K^-\pi^+$ and charge conj
 charged jets, anti- k_T , $R = 0.4$
 $|\eta_{jet}| < 0.5$
 $15 < p_{T, ch jet} < 50$ GeV/c

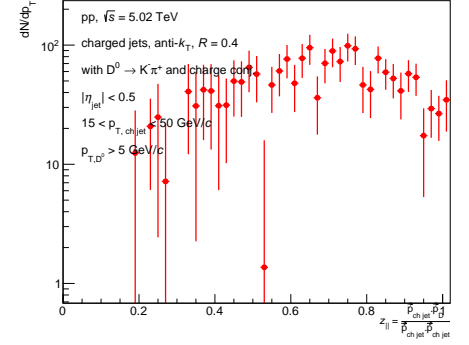


Fig. 36: Total raw $z_{||}$ distributions in pp collisions at $\sqrt{s} = 5.02$ TeV, obtained summing together all D p_T bins without an efficiency correction for $15 < \text{jet } p_T < 50$ GeV/c .

Fig. 35: Raw $z_{||}$ distributions in bins of D⁰ transverse momentum in pp collisions at $\sqrt{s} = 5.02$ TeV for $15 < \text{jet } p_T < 50$ GeV/c .

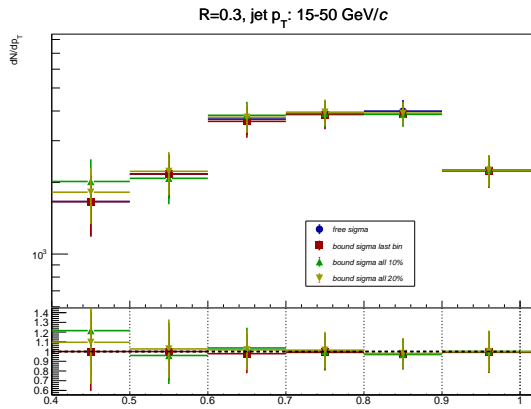


Fig. 37: Comparison of raw D⁰-jet spectra for free sigma and bound sigma fits for $R = 0.3$.

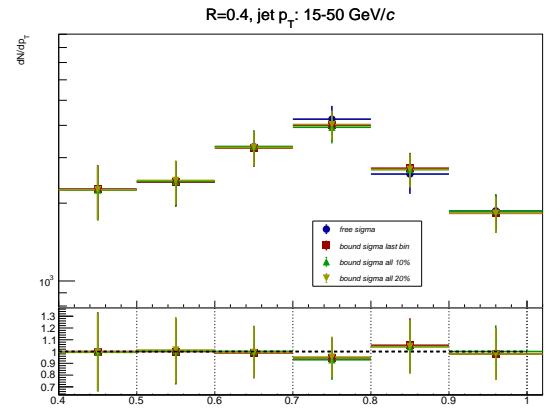


Fig. 38: Comparison of raw D⁰-jet spectra for free sigma and bound sigma fits for $R = 0.4$.

6 Efficiency Correction Procedure

6.1 Reconstruction Efficiency

The efficiency and acceptance ($\text{Acc} \times \epsilon$) were calculated using Monte Carlo PYTHIA6+GEANT3 simulations anchored to the data.

The efficiency is taken as the ratio of the $p_{T,D}$ spectra of the D-tagged generator-level jets for which a matched D-tagged detector-level jet was found over all the generated D-tagged jets. For the detector-level jets, the D meson is required to be within the standard fiducial rapidity cuts. Jets are further requested to have $|\eta_{\text{jet}}| < 0.9 - R$, both at generator and detector levels.

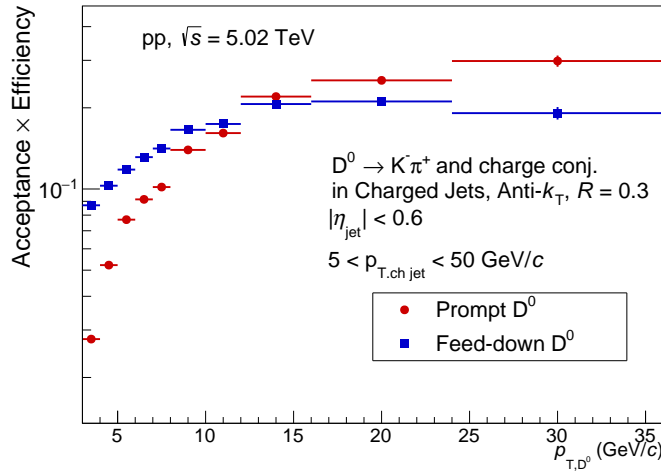


Fig. 39: D^0 -meson-jet reconstruction efficiencies in pp collisions at $\sqrt{s} = 5.02$ TeV, for prompt D mesons in red and non-prompt in blue.

Figure 39 shows the D^0 -jet reconstruction efficiencies as a function of $p_{T,D}$ for prompt and non-prompt D-mesons. Efficiency depends strongly on $p_{T,D}$ because of the topological cuts that are relaxed at higher momenta where the combinatorial background is smaller. The efficiency is with a cut on $p_{T, \text{ch jet}}$ of $5 < p_{T, \text{ch jet}} < 50$ GeV/c (range of the final D^0 -tagged jet p_T spectrum) at the generator level, applied for both denominator and nominator in the efficiency calculation.

For $z_{\parallel, \text{ch}}$ distribution studies, efficiencies are found as a function of D- p_T separately in the respective jet p_T interval and applied accordingly.

6.2 Efficiency-Corrected Yields

As discussed in the previous section, the D-meson reconstruction efficiency shows a strong dependence on $p_{T,D}$ (but has very weak or no dependence on $p_{T, \text{jet}}$). Therefore, in order to reduce the dependence on the Monte Carlo simulation for what concerns jet fragmentation and momentum spectral shape, the efficiency should be applied as a function of the D-meson momentum. In fact, each bin of $p_{T, \text{jet}}$ has contributions from D mesons with very different $p_{T,D}$, which have different efficiencies.

6.2.1 Side-Band Subtraction Method

In the side-band method the efficiency correction is applied by rescaling the D-jet background subtracted p_T spectra in Fig. 3 by $1/(\text{Acc} \times \epsilon)$ in each D-meson p_T bin shown in Fig. 39, where ϵ is the prompt D-jet reconstruction efficiency. The distributions are then summed up to obtain the corrected jet p_T spectra for D-jets. The efficiency corrected jet p_T spectra are shown in Fig. 44 (left), and after rebining in Fig. 44 (right).

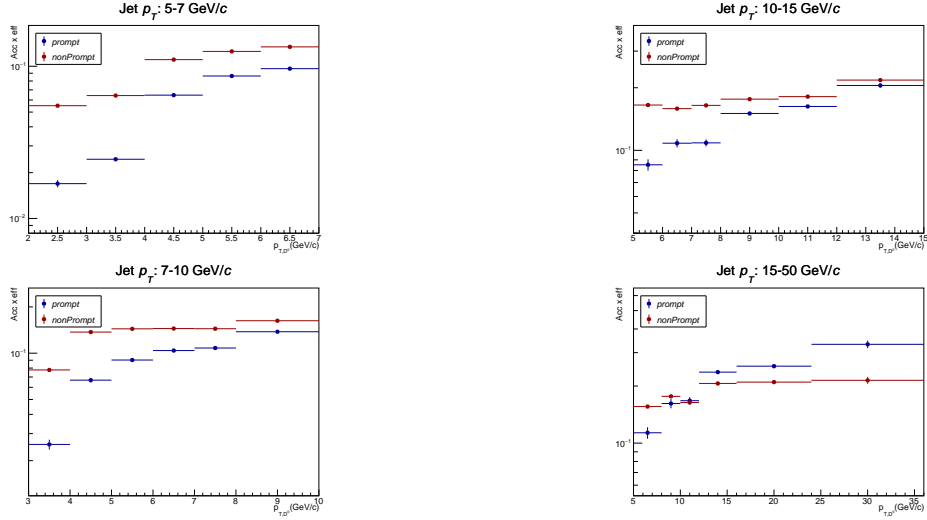


Fig. 40: D⁰-meson-jet reconstruction efficiencies for [top] $5 < \text{jet } p_T < 7 \text{ GeV}/c$ and [bottom] $7 < \text{jet } p_T < 10 \text{ GeV}/c$, $R = 0.3$.
 Fig. 41: D⁰-meson-jet reconstruction efficiencies for [top] $10 < \text{jet } p_T < 15 \text{ GeV}/c$ and [bottom] $15 < \text{jet } p_T < 50 \text{ GeV}/c$, $R = 0.3$.

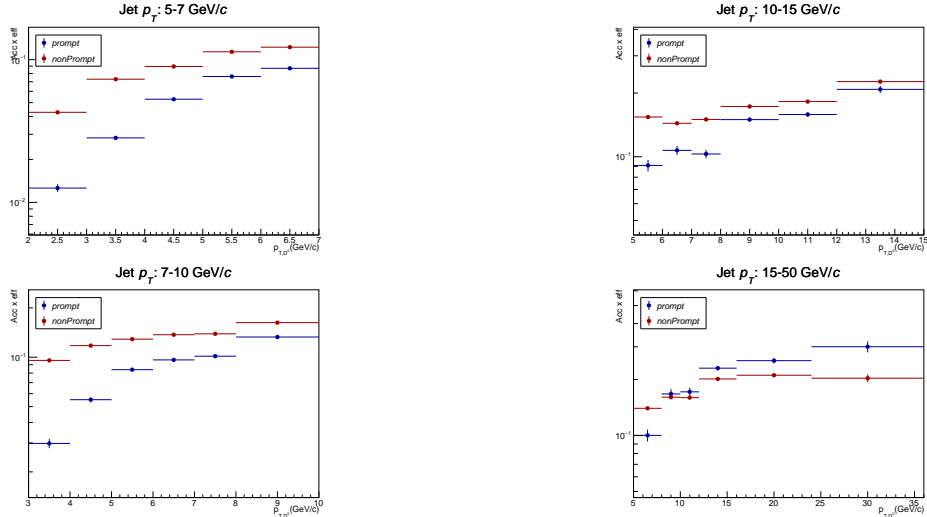


Fig. 42: D⁰-meson-jet reconstruction efficiencies for [top] $5 < \text{jet } p_T < 7 \text{ GeV}/c$ and [bottom] $7 < \text{jet } p_T < 10 \text{ GeV}/c$, $R = 0.4$.
 Fig. 43: D⁰-meson-jet reconstruction efficiencies for [top] $10 < \text{jet } p_T < 15 \text{ GeV}/c$ and [bottom] $15 < \text{jet } p_T < 50 \text{ GeV}/c$, $R = 0.4$.

Figure 45 shows the relative statistical uncertainties for the Side-Band subtraction method with $p_{T,D} > 3 \text{ GeV}/c$.

Likewise, for $z_{||,ch}$ studies, the side band subtracted signal distributions from figures 7, 11, 15, 19, 23, 27, 31, 35 are first efficiency corrected, then summed up and rebinned to give figures 46, 47, 48, 49, 50, 51, 52, 53. Their relative uncertainties are on their right in the same figures.

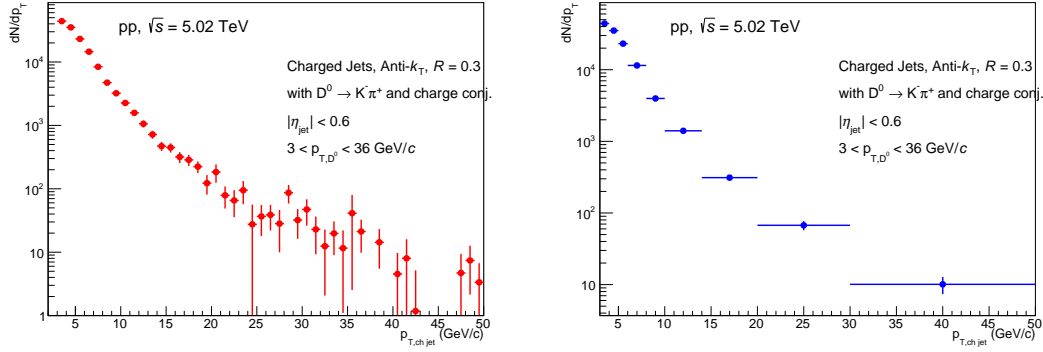


Fig. 44: Efficiency corrected D-jet yield obtained for the Side-Band subtraction method in pp collisions at $\sqrt{s} = 5.02$ TeV. D mesons are required to have $3 < p_{T, D} < 36$ GeV/c. Right: after rebinning.

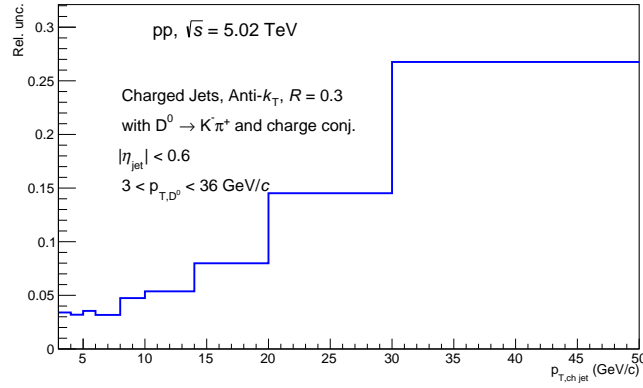


Fig. 45: Statistical uncertainties obtained using the side band method for D^0 -jets in pp at $\sqrt{s} = 5.02$ TeV, with $p_{T, D} > 3$ GeV/c. Reconstruction efficiency correction is applied.

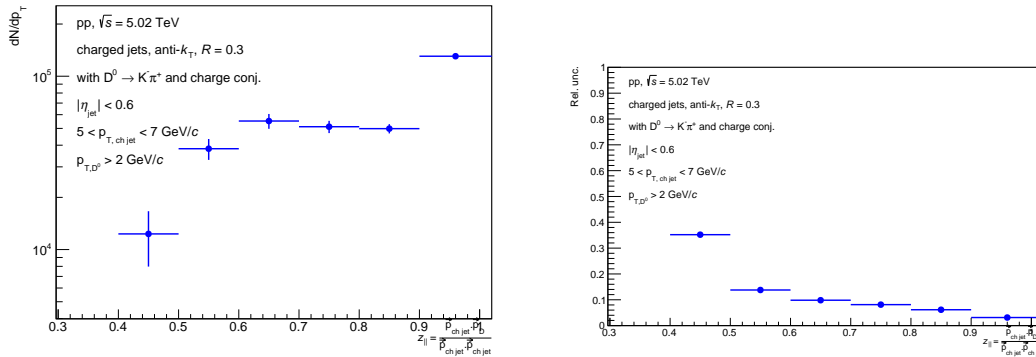


Fig. 46: Left: Efficiency corrected D-jet yield in $z_{\parallel, \text{ch}}$ obtained for jet $5 < p_T < 7$ GeV/c, $R = 0.3$ in pp collisions at $\sqrt{s} = 5.02$ TeV. D mesons are required to have $p_{T, D} > 2$ GeV/c. Right: statistical uncertainties.

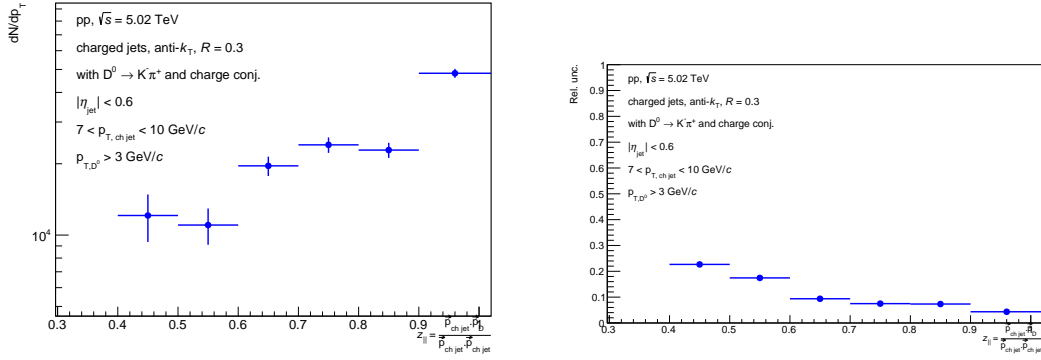


Fig. 47: Left: Efficiency corrected D-jet yield in $z_{||, \text{ch}}$ obtained for jet $7 < p_T < 10$ GeV/c, $R = 0.3$ in pp collisions at $\sqrt{s} = 5.02$ TeV. D mesons are required to have $p_{T,D} > 2$ GeV/c. Right: statistical uncertainties.

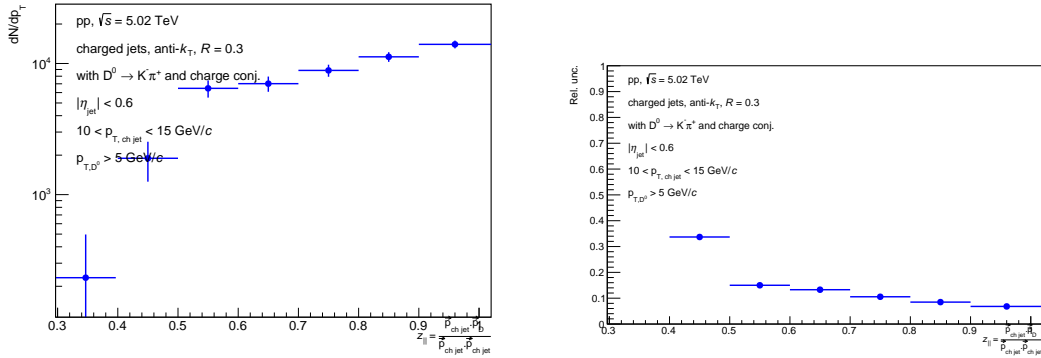


Fig. 48: Left: Efficiency corrected D-jet yield in $z_{||, \text{ch}}$ obtained for jet $10 < p_T < 15$ GeV/c, $R = 0.3$ in pp collisions at $\sqrt{s} = 5.02$ TeV. D mesons are required to have $p_{T,D} > 2$ GeV/c. Right: statistical uncertainties.

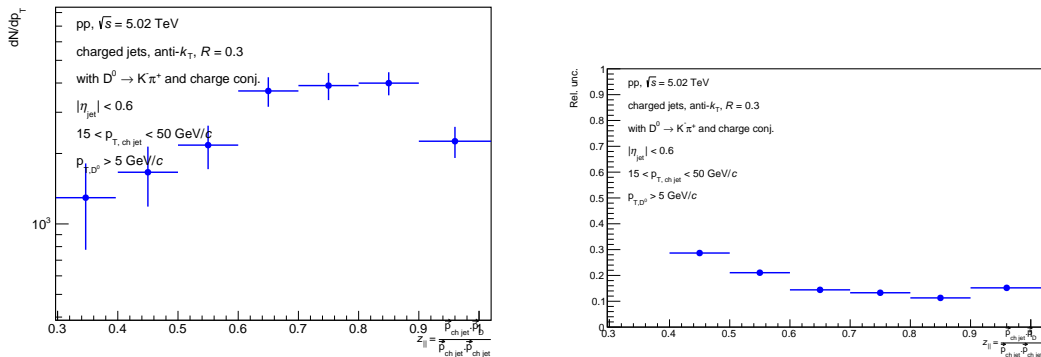


Fig. 49: Left: Efficiency corrected D-jet yield in $z_{||, \text{ch}}$ obtained for jet $15 < p_T < 50$ GeV/c, $R = 0.3$ in pp collisions at $\sqrt{s} = 5.02$ TeV. D mesons are required to have $p_{T,D} > 2$ GeV/c. Right: statistical uncertainties.

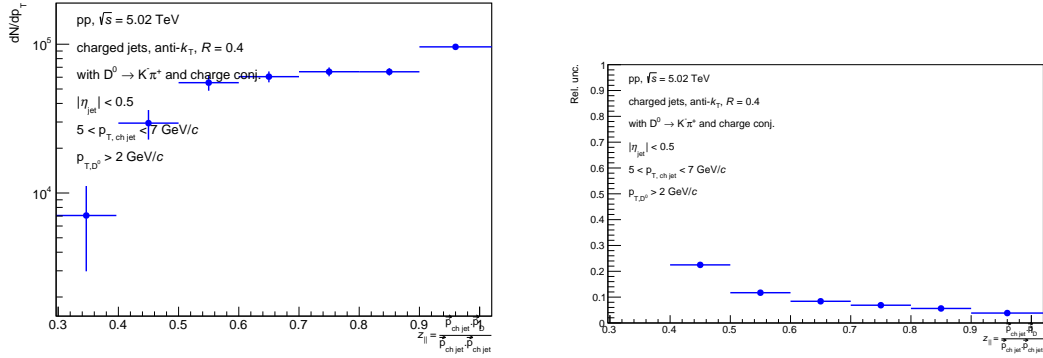


Fig. 50: Left: Efficiency corrected D-jet yield in $z_{||, \text{ch}}$ obtained for jet $5 < p_T < 7$ GeV/c, $R = 0.4$ in pp collisions at $\sqrt{s} = 5.02$ TeV. D mesons are required to have $p_{T, D} > 2$ GeV/c. Right: statistical uncertainties.

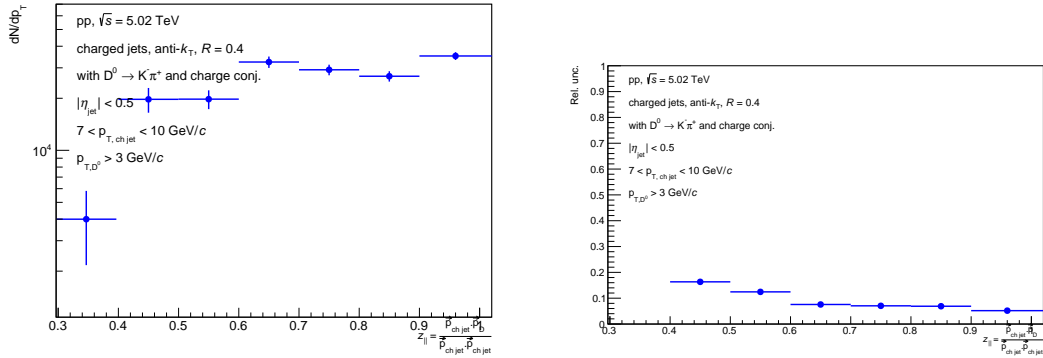


Fig. 51: Left: Efficiency corrected D-jet yield in $z_{||, \text{ch}}$ obtained for jet $7 < p_T < 10$ GeV/c, $R = 0.4$ in pp collisions at $\sqrt{s} = 5.02$ TeV. D mesons are required to have $p_{T, D} > 2$ GeV/c. Right: statistical uncertainties.

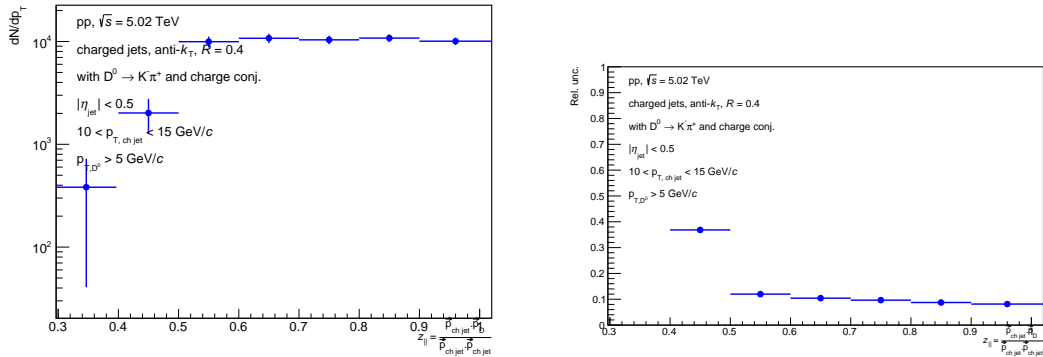


Fig. 52: Left: Efficiency corrected D-jet yield in $z_{||, \text{ch}}$ obtained for jet $10 < p_T < 15$ GeV/c, $R = 0.4$ in pp collisions at $\sqrt{s} = 5.02$ TeV. D mesons are required to have $p_{T, D} > 2$ GeV/c. Right: statistical uncertainties.

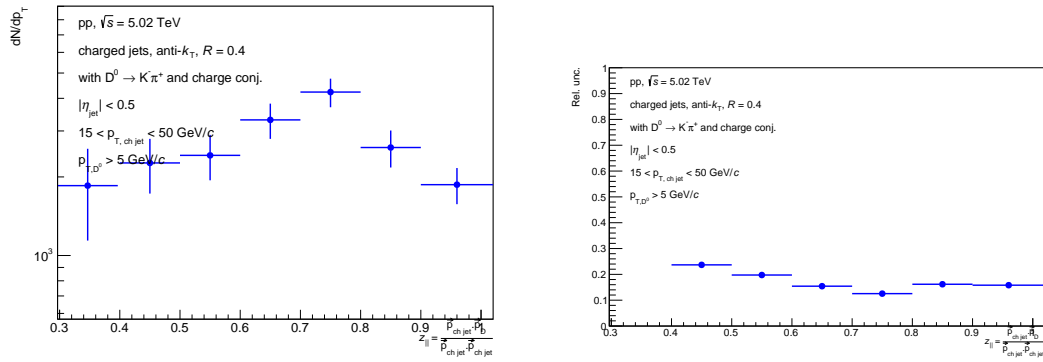


Fig. 53: Left: Efficiency corrected D-jet yield in $z_{||,ch}$ obtained for jet $15 < p_T < 50$ GeV/c, $R = 0.4$ in pp collisions at $\sqrt{s} = 5.02$ TeV. D mesons are required to have $p_{T,D} > 2$ GeV/c. Right: statistical uncertainties.

7 Detector Response Matrix

The detector response is studied with a Monte Carlo simulation in which particles generated by an event generator are run through a transport code (GEANT3), that simulates the response of the detector elements, and then the same event reconstruction used in data is performed. Only $c\bar{c}$ events are used.

Two sets of jets are obtained from the same event. One of them is obtained from the generator-level information and the second from the reconstructed signals after the detector simulation. The generated and reconstructed jets are matched by looking for the same D meson at both levels (using its MC label)

The prompt detector response matrices are used to unfold the measured D-jet p_T spectra after subtraction of the B feed-down component. For each D-jet, the B feed-down is estimated based on simulations, as described later, that is folded with the presented non-prompt detector response matrix.

7.1 Jet Momentum Detector Response

The detector response matrices for prompt and non-prompt are shown in fig. 54 for jet p_T cross-section studies.

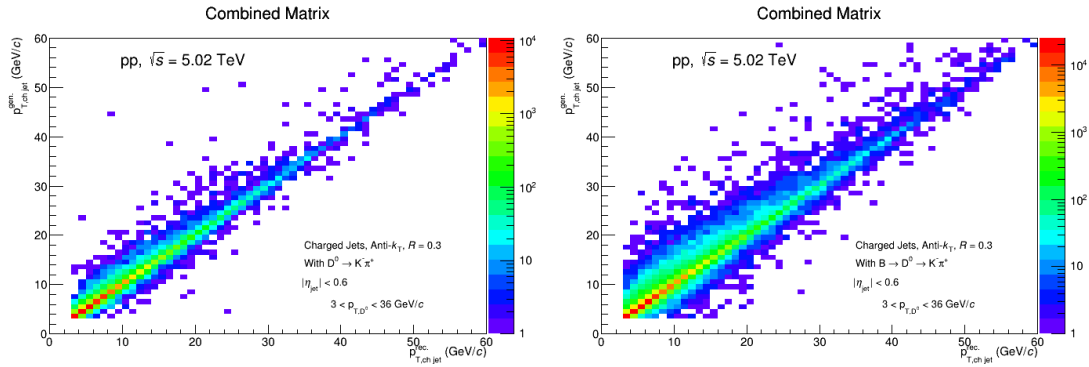


Fig. 54: Detector response matrix calculated with the PYTHIA part of the simulation of pp events at $\sqrt{s} = 5.02$ TeV, for prompt (left) and non-prompt (right) D^0 -jet, $R=0.3$. $3 < p_{T,D} < 36$ GeV/c .

7.2 Parallel Momentum Fraction Detector Response

The detector response matrices for prompt and non-prompt in different intervals of jet p_T are shown in fig. 55, 56, 57 and 58 for $z_{||,ch}$ studies with $R = 0.3$.

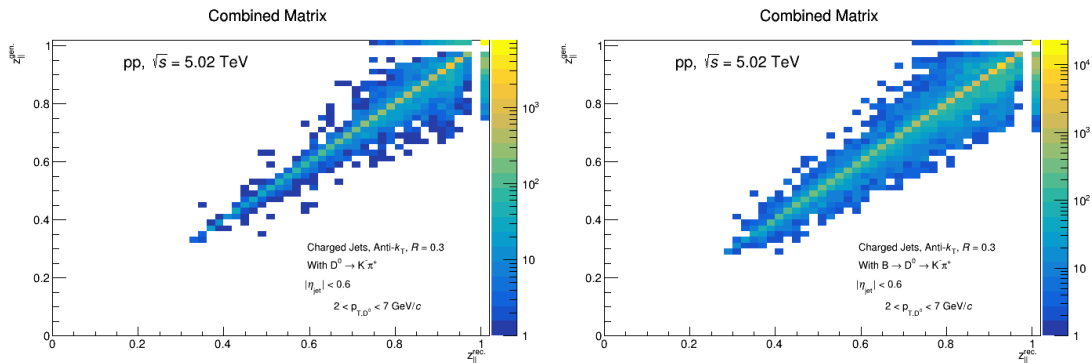


Fig. 55: Detector response matrix calculated with the PYTHIA part of the simulation of pp events at $\sqrt{s} = 5.02$ TeV, for prompt (left) and non-prompt (right) D^0 -jet, $R = 0.3$. $5 < \text{jet-}p_T < 7$ GeV/c $p_{T,D} > 2$ GeV/c .

For $R = 0.4$, the corresponding matrices are shown in fig. 59, 60, 61 and 62.

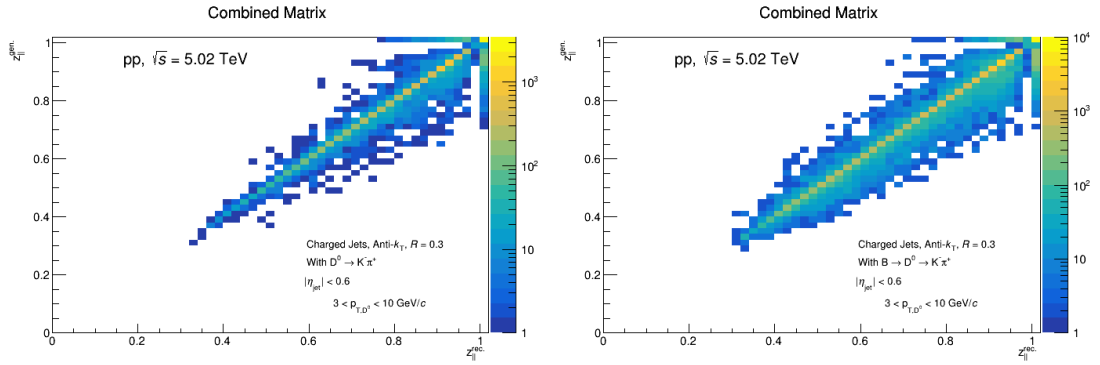


Fig. 56: Detector response matrix calculated with the PYTHIA part of the simulation of pp events at $\sqrt{s} = 5.02$ TeV, for prompt (left) and non-prompt (right) D⁰-jet, $R = 0.3$. $7 < \text{jet-}p_T < 10$ GeV/c $p_{T,D^0} > 3$ GeV/c .

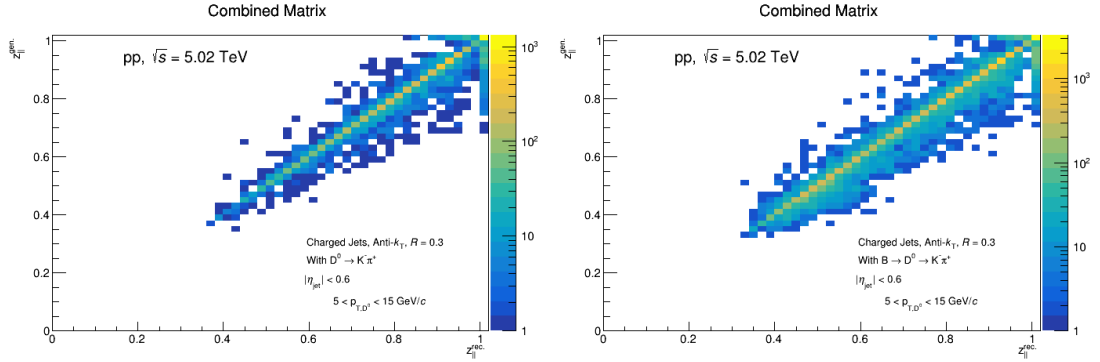


Fig. 57: Detector response matrix calculated with the PYTHIA part of the simulation of pp events at $\sqrt{s} = 5.02$ TeV, for prompt (left) and non-prompt (right) D⁰-jet, $R = 0.3$. $10 < \text{jet-}p_T < 15$ GeV/c $p_{T,D^0} > 5$ GeV/c .

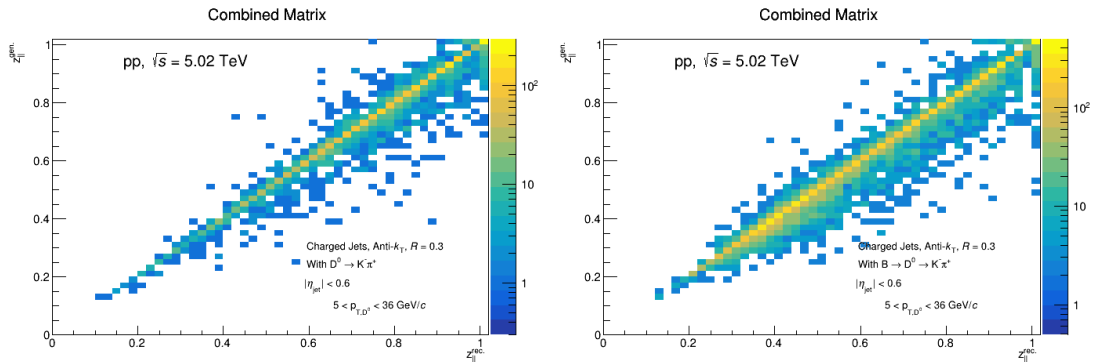


Fig. 58: Detector response matrix calculated with the PYTHIA part of the simulation of pp events at $\sqrt{s} = 5.02$ TeV, for prompt (left) and non-prompt (right) D⁰-jet, $R = 0.3$. $15 < \text{jet-}p_T < 50$ GeV/c $p_{T,D^0} > 5$ GeV/c .

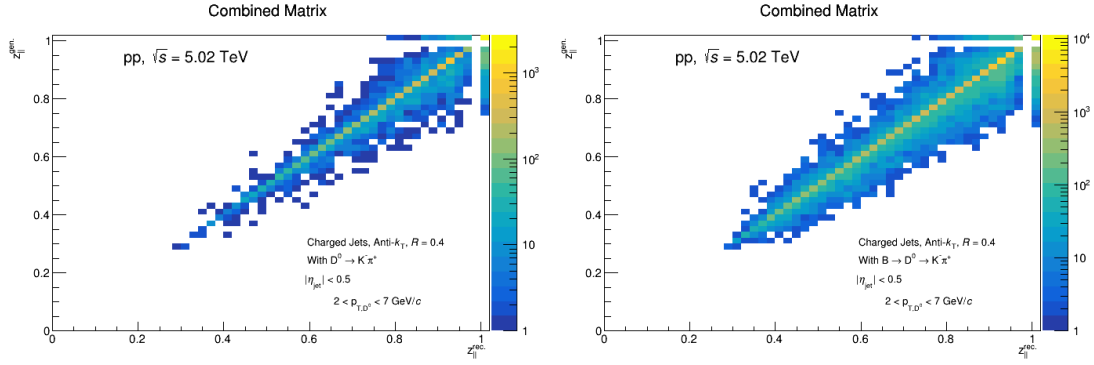


Fig. 59: Detector response matrix calculated with the PYTHIA part of the simulation of pp events at $\sqrt{s} = 5.02$ TeV, for prompt (left) and non-prompt (right) D^0 -jet, $R = 0.4$. $5 < \text{jet-}p_T < 7 \text{ GeV}/c$ $p_{T,D} > 2 \text{ GeV}/c$.

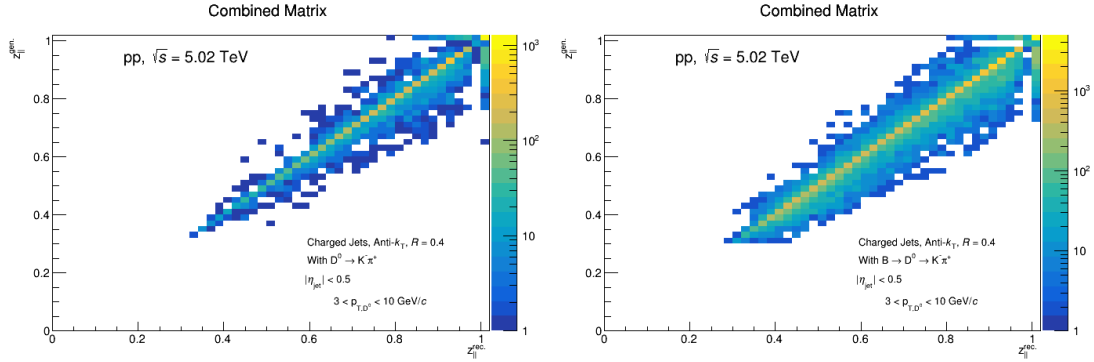


Fig. 60: Detector response matrix calculated with the PYTHIA part of the simulation of pp events at $\sqrt{s} = 5.02$ TeV, for prompt (left) and non-prompt (right) D^0 -jet, $R = 0.4$. $7 < \text{jet-}p_T < 10 \text{ GeV}/c$ $p_{T,D} > 3 \text{ GeV}/c$.

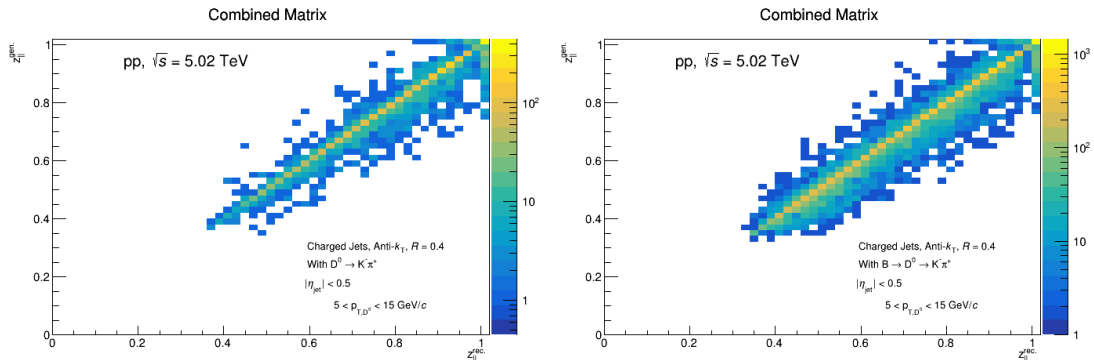


Fig. 61: Detector response matrix calculated with the PYTHIA part of the simulation of pp events at $\sqrt{s} = 5.02$ TeV, for prompt (left) and non-prompt (right) D^0 -jet, $R = 0.4$. $10 < \text{jet-}p_T < 15 \text{ GeV}/c$ $p_{T,D} > 5 \text{ GeV}/c$.

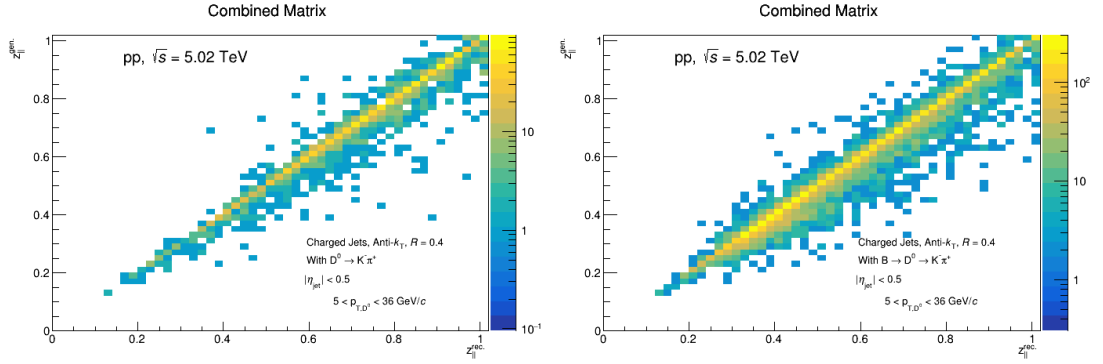


Fig. 62: Detector response matrix calculated with the PYTHIA part of the simulation of pp events at $\sqrt{s} = 5.02$ TeV, for prompt (left) and non-prompt (right) D⁰-jet, $R = 0.4$. $15 < \text{jet-}p_T < 50$ GeV/c $p_{T,D^0} > 5$ GeV/c .

8 Feed-Down Correction

A fraction of the measured D mesons originates from the decays of B mesons. These D mesons are usually referred to as non-prompt to distinguish them from the prompt fraction, i.e. the ones that come directly from the fragmentation of a charm quark or decays of higher excited charm states. The longer decay length of B mesons combined with the topological cuts applied in the D meson selection causes the reconstruction efficiency to be higher for the non-prompt fraction compared to the prompt fraction. This is shown in Fig. 39. As a consequence, the natural admixture of the prompt and non-prompt D-jets is biased in a detector-specific way towards the non-prompt. In order to make meaningful comparisons with theoretical and other experimental results one needs to either correct the bias or remove completely the non-prompt fraction and report only the prompt fraction. Both approaches require to use theoretical models or Monte Carlo simulations. In ALICE the second approach has been preferred so far, and for this analysis we decided to follow it.

8.1 Monte Carlo Simulation

For the D-meson spectra analysis, ALICE has used FONLL [4] calculations to estimate the non-prompt fraction [5, 6, 7]. In this analysis however we need to extract the B feed-down fraction also as a function of the jet kinematics, therefore this approach is not applicable. We decided to use POWHEG [8], a Monte Carlo event generator known to reasonably reproduce FONLL calculations and previous experimental results [9]. The second part of the parton shower and the fragmentation into hadrons is provided by PYTHIA6 (Perugia-2011 tune).

We generated 25 M $b\bar{b}$ events for the baseline parameters: $m_b = 4.75 \text{ GeV}/c^2$, $\mu_R = \mu_F = \mu_0 = \sqrt{m^2 + p_T^2}$, where m_b is the beauty masses, μ_R and μ_F are respectively the renormalization and factorization scale factors; used based PDF set is: CT10NLO. Variations of the simulation parameter are a source of the B feed-down subtraction systematic uncertainties.

The reconstruction of D-meson jets is performed in the POWHEG+PYTHIA6 events using the same procedure used for the main data analysis.

8.2 Feed-Down Subtraction for jet- p_T cross-section and $z_{||,ch}$ distributions

The B feed-down (FD) is subtracted from the measured D-meson jet p_T spectra by scaling the cross-section of D-meson jets obtained from the analysis of the POWHEG+PYTHIA simulation by the integrated luminosity of the analyzed data, according to Eq. 2. Similarly, the B feed-down (FD) is subtracted from the measured D-meson $z_{||,ch}$ distributions by scaling the distributions of D-meson jets obtained from the analysis of the POWHEG+PYTHIA simulation by the integrated luminosity of the analyzed data, according to Eq. 3:

$$N^{c \rightarrow D^0}(p_{T,chjet}^{\det}) = N^{c,b \rightarrow D^0}(p_{T,chjet}^{\det}) - R_{\det}^{b \rightarrow D^0}(p_{T,chjet}^{\det}, p_{T,chjet}^{\text{part}}) \otimes \sum_{p_{T,D}} \frac{\epsilon^{b \rightarrow D^0}(p_{T,D})}{\epsilon^{c \rightarrow D^0}(p_{T,D})} N_{\text{POWHEG}}^{b \rightarrow D^0}(p_{T,D}, p_{T,chjet}^{\text{part}}), \quad (2)$$

$$N^{c \rightarrow D^0}(z_{||,ch}^{\det}) = N^{c,b \rightarrow D^0}(z_{||,ch}^{\det}) - R_{\det}^{b \rightarrow D^0}(z_{||,ch}^{\det}, z_{||,ch}^{\text{gen}}) \otimes \sum_{p_{T,D}} \frac{\epsilon^{b \rightarrow D^0}(p_{T,D})}{\epsilon^{c \rightarrow D^0}(p_{T,D})} N_{\text{POWHEG}}^{b \rightarrow D^0}(p_{T,D}, z_{||,ch}^{\text{gen}}), \quad (3)$$

where:

- $N^{c \rightarrow D^0}(p_{T,chjet}^{\det})$ or $N^{c \rightarrow D^0}(z_{||,ch}^{\det})$ is the efficiency-corrected measured yield after FD subtraction;
- $N^{c,b \rightarrow D^0}(p_{T,chjet}^{\det})$ or $N^{c,b \rightarrow D^0}(z_{||,ch}^{\det})$ is the efficiency-corrected measured yield before FD subtraction;

- $R_{\text{det}}^{b \rightarrow D^0}(p_{T,\text{chjet}}^{\text{det}}, p_{T,\text{chjet}}^{\text{part}})$ or $R_{\text{det}}^{b \rightarrow D^0}(z_{||,\text{ch}}^{\text{det}}, z_{||,\text{ch}}^{\text{gen}})$ is the detector response matrix of the p_T of non-prompt D⁰-jets;
- the symbol \otimes is to be interpreted as the standard product of the response matrix times the vector of the yields in bins of $p_{T,\text{chjet}}^{\text{part}}$ or $z_{||,\text{ch}}^{\text{gen}}$;
- $\epsilon^{c \rightarrow D^0}(p_{T,D})$ and $\epsilon^{b \rightarrow D^0}(p_{T,D})$ are respectively the reconstruction efficiencies of prompt and non-prompt D⁰ mesons;
- $N_{\text{POWHEG}}^{b \rightarrow D^0}(p_{T,D}, p_{T,\text{chjet}}^{\text{part}})$ is the cross-section of D⁰-jets from the POWHEG simulation scaled by the integrated luminosity of the analyzed data.
- $N_{\text{POWHEG}}^{b \rightarrow D^0}(p_{T,D}, z_{||,\text{ch}}^{\text{gen}})$ is the D⁰-jets $z_{||,\text{ch}}$ distribution from the POWHEG simulation scaled by the integrated luminosity of the analyzed data.

Since the measured yields are corrected for the prompt D-jet efficiency, the The POWHEG D-jet spectrum is weighted with the ratio of the non-prompt over the prompt D-jet efficiency in D-meson p_T bins.

There are differences between the prompt and non-prompt response, for this reason the FD has to be subtracted before unfolding the measured spectrum; furthermore, as illustrated in Eq. 2 and 3, the spectrum obtained from the POWHEG simulation is smeared using the response of non-prompt D-jets. Figure 63 compares the measured D⁰-jet p_T spectrum with the FD spectrum and the subtracted spectrum for jet- p_T cross-section.

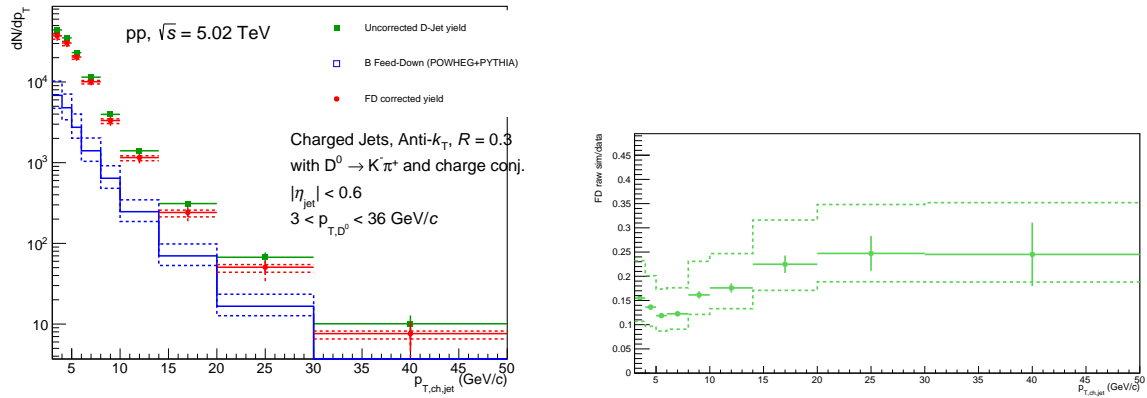


Fig. 63: Left: Efficiency-corrected measured D⁰-jet spectrum in pp collisions at $\sqrt{s} = 5.02$ TeV before FD correction (green) and after FD correction (red). The FD spectrum is also plotted (blue) with its uncertainties. Right plot shows ratio of non-prompt to inclusive D⁰-jet spectrum.

For $z_{||,\text{ch}}$ distributions with $R = 0.3$ the corresponding figures are 64, 65, 66, 67. and for $R = 0.4$, we have figures 68, 69, 70, 71.

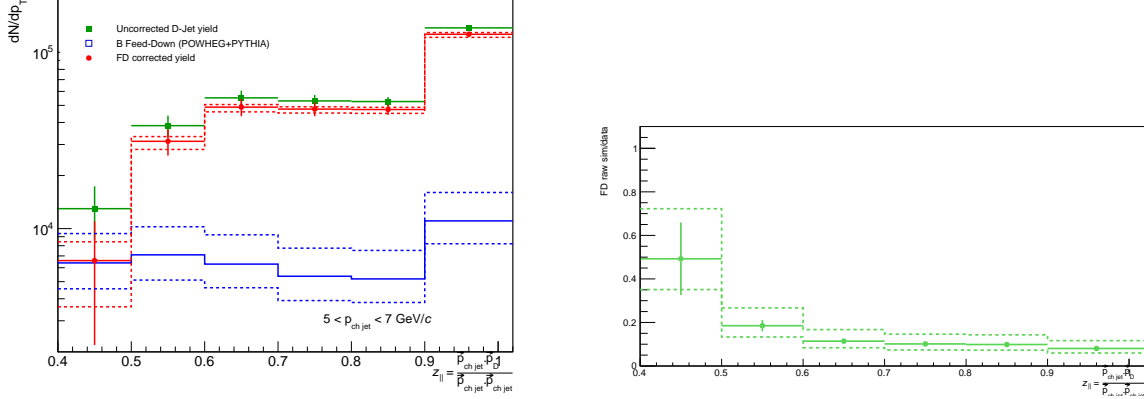


Fig. 64: $R = 0.3$, $5 < \text{jet } p_T < 7 \text{ GeV}/c$. Left: Efficiency-corrected measured D^0 -jet spectrum in pp collisions at $\sqrt{s} = 5.02 \text{ TeV}$ before FD correction (green) and after FD correction (red). The FD spectrum is also plotted (blue) with its uncertainties. Right plot shows ratio of non-prompt to inclusive D^0 -jet spectrum.

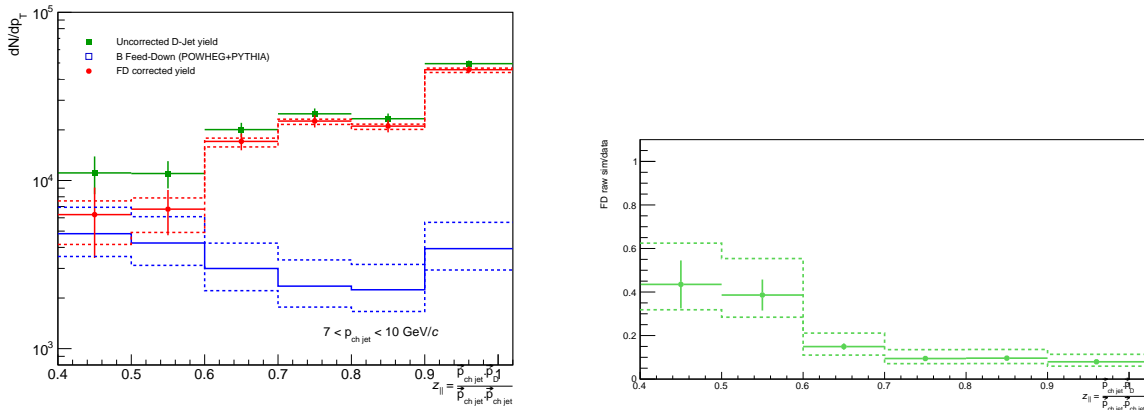


Fig. 65: $R = 0.3$, $7 < \text{jet } p_T < 10 \text{ GeV}/c$. Left: Efficiency-corrected measured D^0 -jet spectrum in pp collisions at $\sqrt{s} = 5.02 \text{ TeV}$ before FD correction (green) and after FD correction (red). The FD spectrum is also plotted (blue) with its uncertainties. Right plot shows ratio of non-prompt to inclusive D^0 -jet spectrum.

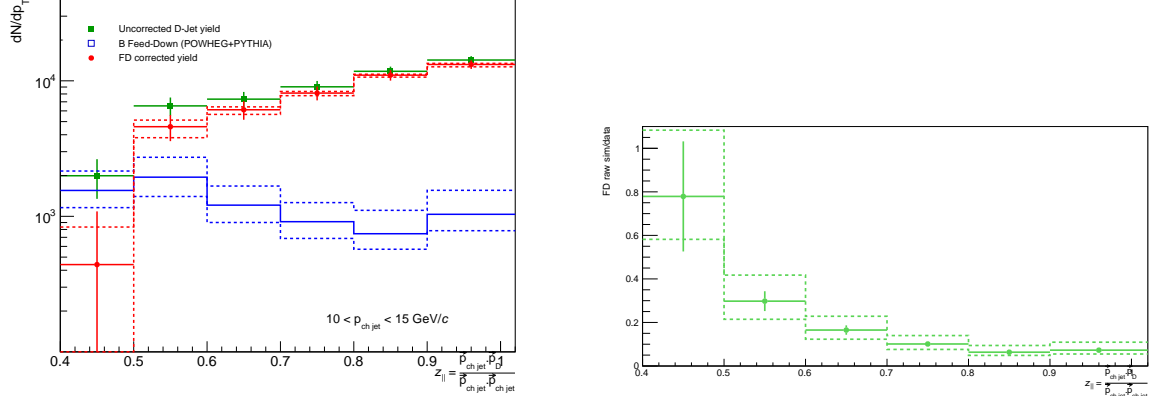


Fig. 66: $R = 0.3$, $10 < \text{jet } p_T < 15 \text{ GeV}/c$. Left: Efficiency-corrected measured D⁰-jet spectrum in pp collisions at $\sqrt{s} = 5.02 \text{ TeV}$ before FD correction (green) and after FD correction (red). The FD spectrum is also plotted (blue) with its uncertainties. Right plot shows ratio of non-prompt to inclusive D⁰-jet spectrum.

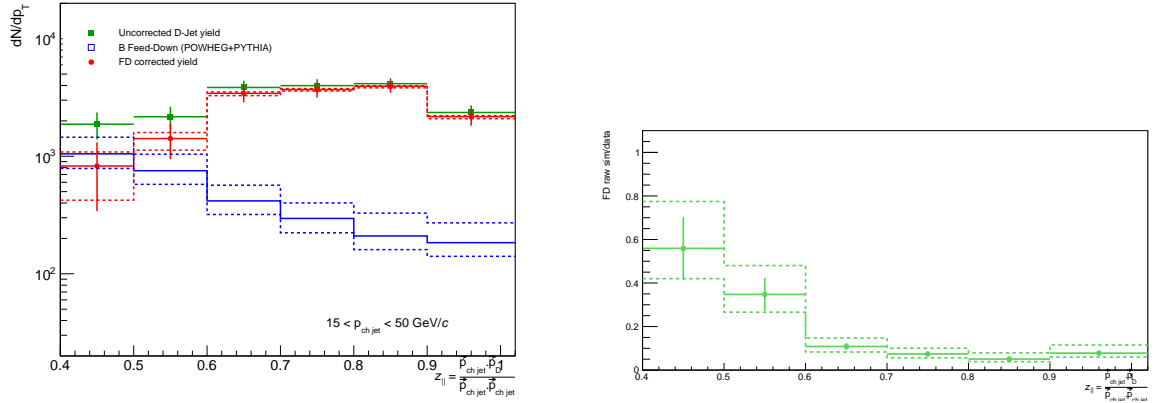


Fig. 67: $R = 0.3$, $15 < \text{jet } p_T < 50 \text{ GeV}/c$. Left: Efficiency-corrected measured D⁰-jet spectrum in pp collisions at $\sqrt{s} = 5.02 \text{ TeV}$ before FD correction (green) and after FD correction (red). The FD spectrum is also plotted (blue) with its uncertainties. Right plot shows ratio of non-prompt to inclusive D⁰-jet spectrum.

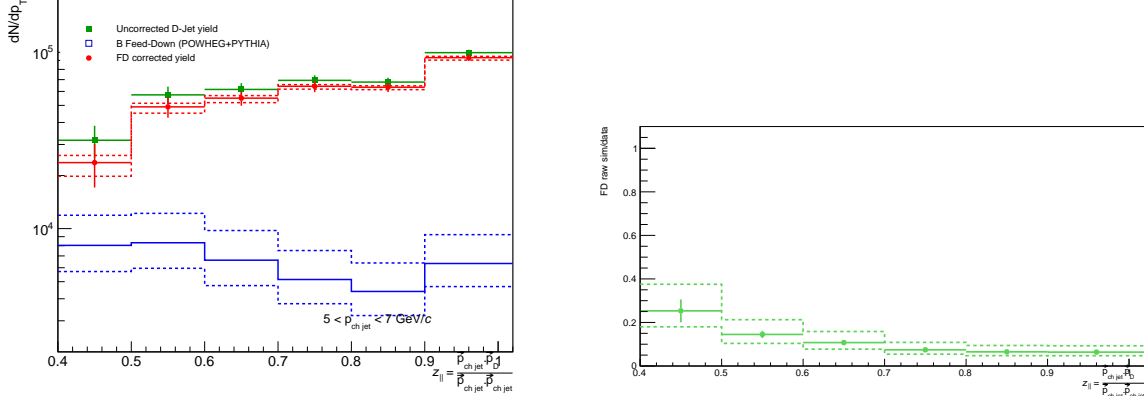


Fig. 68: $R = 0.4$, $5 < \text{jet } p_T < 7$ GeV/c . Left: Efficiency-corrected measured D^0 -jet spectrum in pp collisions at $\sqrt{s} = 5.02$ TeV before FD correction (green) and after FD correction (red). The FD spectrum is also plotted (blue) with its uncertainties. Right plot shows ratio of non-prompt to inclusive D^0 -jet spectrum.

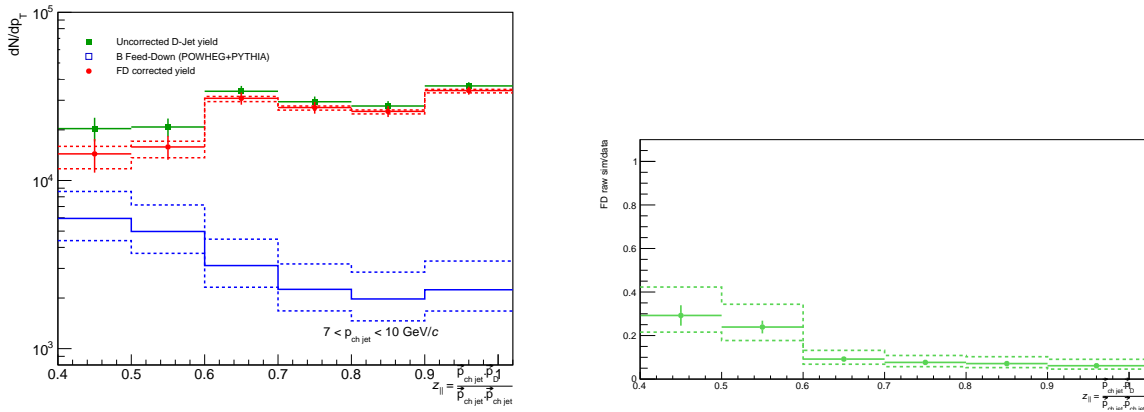


Fig. 69: $R = 0.4$, $7 < \text{jet } p_T < 10$ GeV/c . Left: Efficiency-corrected measured D^0 -jet spectrum in pp collisions at $\sqrt{s} = 5.02$ TeV before FD correction (green) and after FD correction (red). The FD spectrum is also plotted (blue) with its uncertainties. Right plot shows ratio of non-prompt to inclusive D^0 -jet spectrum.

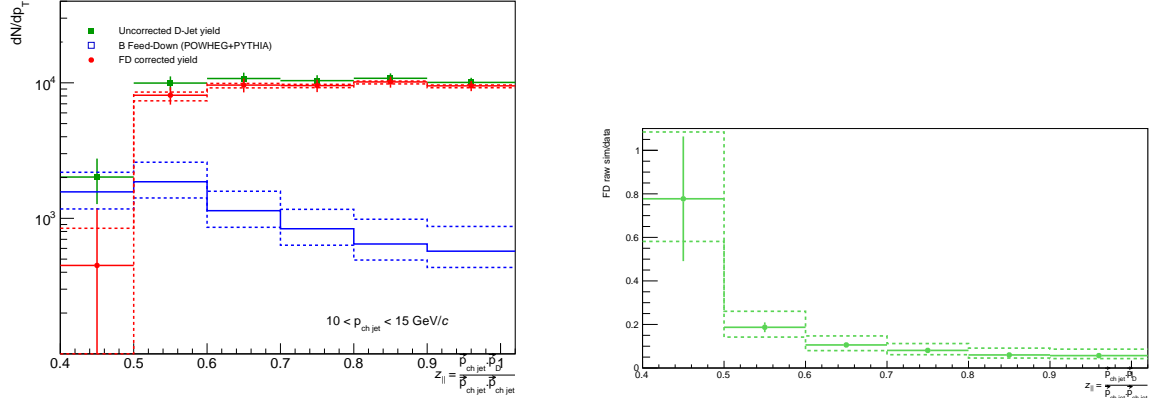


Fig. 70: $R = 0.4$, $10 < \text{jet } p_T < 15 \text{ GeV}/c$. Left: Efficiency-corrected measured D⁰-jet spectrum in pp collisions at $\sqrt{s} = 5.02 \text{ TeV}$ before FD correction (green) and after FD correction (red). The FD spectrum is also plotted (blue) with its uncertainties. Right plot shows ratio of non-prompt to inclusive D⁰-jet spectrum.

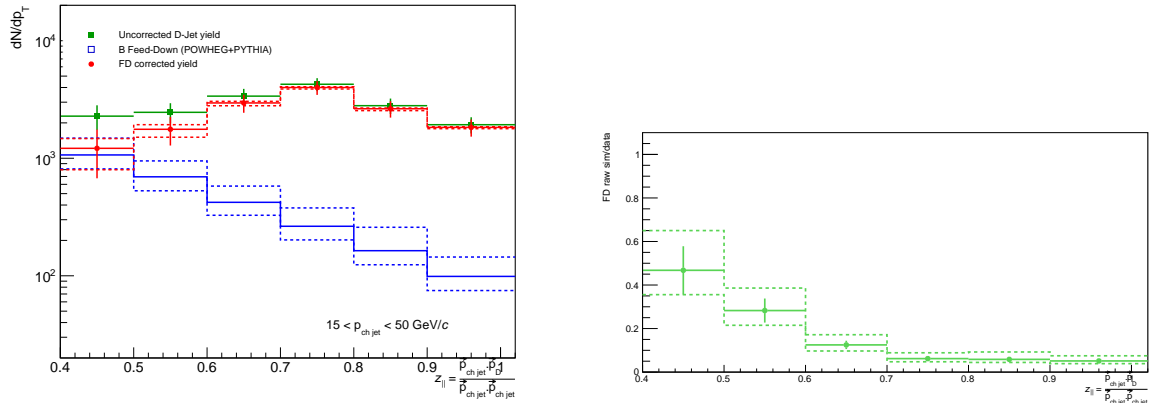


Fig. 71: $R = 0.4$, $15 < \text{jet } p_T < 50 \text{ GeV}/c$. Left: Efficiency-corrected measured D⁰-jet spectrum in pp collisions at $\sqrt{s} = 5.02 \text{ TeV}$ before FD correction (green) and after FD correction (red). The FD spectrum is also plotted (blue) with its uncertainties. Right plot shows ratio of non-prompt to inclusive D⁰-jet spectrum.

9 Unfolding

Due to detector finite momentum resolution and tracking inefficiency the jet p_T spectra measured as described in the previous sections are distorted. These distortions are detector-specific and do not allow a direct comparison with theoretical models and other independent experimental results. In order to correct for these distortions, we first need to assess the detector performance and quantify the detector response to the D-meson jets. Then the matrix is rebinned according to the binning used for the final jet p_T spectra. The detector response matrix, a distribution used as a prior and the corrected jet p_T spectrum obtained from the data are passed to the unfolding algorithm. The algorithm returns an unfolded jet p_T spectrum. As a prior, the spectrum obtained from the Monte Carlo simulation at the generator level is used.

9.1 D^0 -tagged jets

Figure 72 shows a rebinned response matrix for prompt D^0 -jets. The jet p_T spectra corrected for reconstruction efficiency and B feed-down before unfolding (blue) and after unfolding (red), for the side-band method, are presented in Fig. 73. Unfolding is done with Bayesian technique using the RooUnfold software package. The default method is the Bayesian with 4 iterations and $p_{T, \text{chjet}}$ ranges are $3 < p_{T, \text{chjet}} < 50$ both for the generator and reconstructed level p_T with over/under flow bins considered in the unfolding procedure. The green line represents refolded back spectrum, and is compared to the measured jet spectrum before unfolding with different iterations in the Bayes unfolding - right panel of Fig. 74. Figure 74 (left) shows also unfolded spectra with next iterations compared to the default spectrum obtained with 4 iterations. The final reported jet p_T range is $5 < p_{T, \text{chjet}} < 50$ GeV/c. Comparison of unfolded spectra with the SVD method, different p_T ranges for the input and unfolded spectra, and different priors are presented in the systematic uncertainties section, see 10.4.

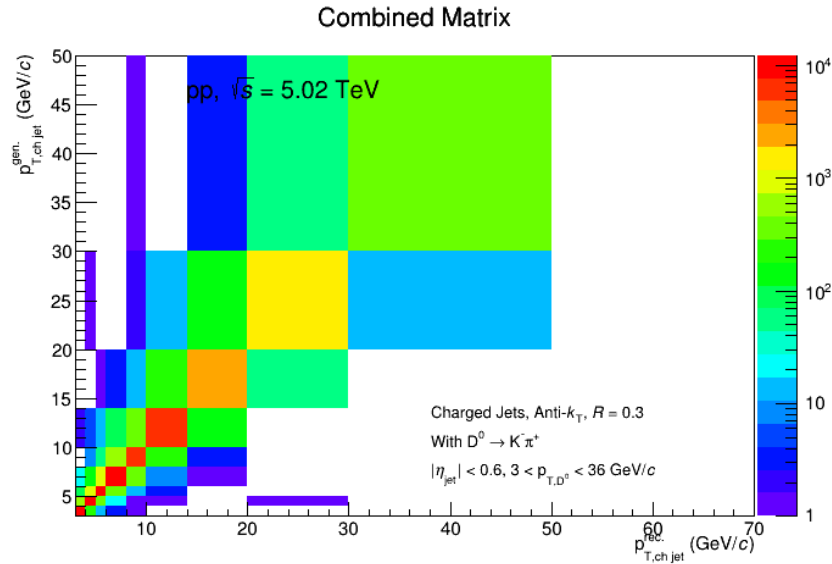


Fig. 72: Rebinning detector response matrix for prompt D^0 -jet in pp events at $\sqrt{s} = 5.02$ TeV, with $R=0.3$.

9.2 D^0 -tagged jets: Parallel momentum fraction, $z_{||}^{\text{ch}}$

The measure of detector performance is quantified in detector response matrices using the final binning for $z_{||}^{\text{ch}}$ used for unfolding, similar to what was done for unfolding in the previous sub-section in bins of jet- p_T . For different jet- p_T intervals the rebinned detector response matrices of previously shown detector response matrices for prompt D-jets are:

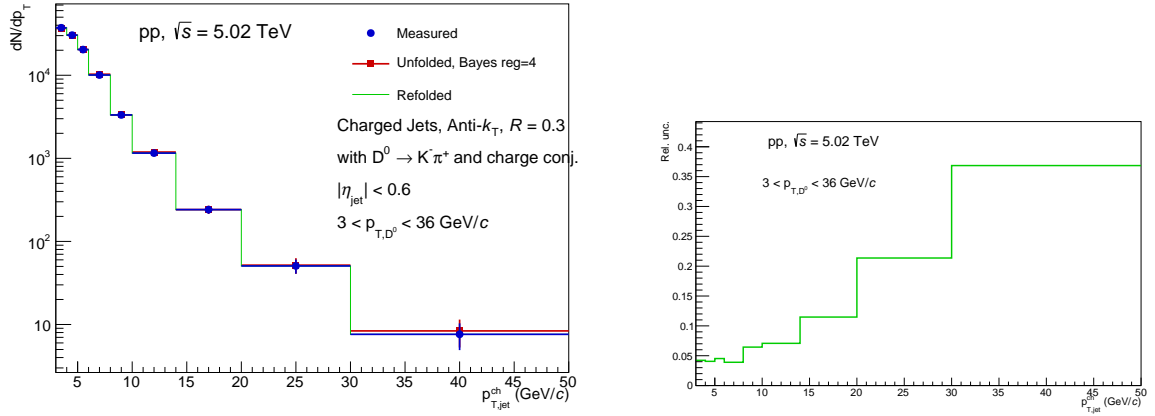


Fig. 73: Left: Corrected jet p_T spectrum before (blue) and after (red) the unfolding procedure (Bayesian method with 4 iterations), pp events at $\sqrt{s} = 5.02$ TeV. Right: Relative statistical uncertainties on the D^0 -tagged jet p_T spectrum after unfolding.

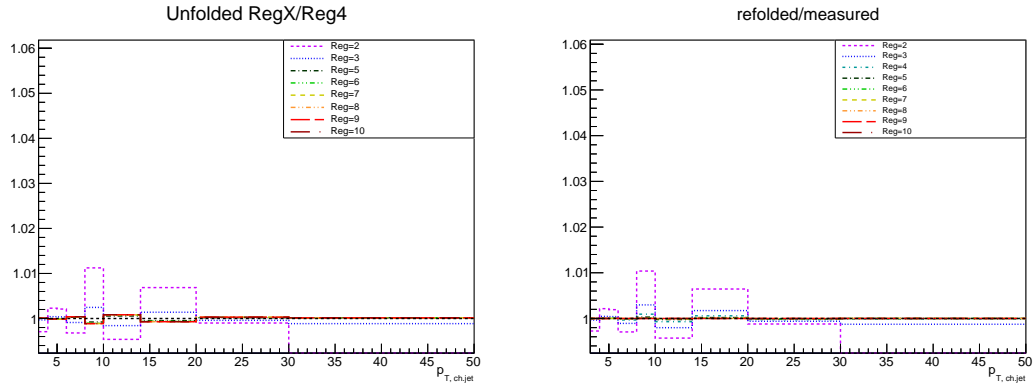


Fig. 74: Left: ratio of the unfolded spectra for up to 10 iterations to the default unfolded spectrum with 4 iterations in the Bayesian unfolding. Right: ratio of the refolded spectrum for up to 10 iterations to the measured in the Bayesian unfolding. The considered jet p_T range is above 5 GeV/c.

9.2.1 $R = 0.3$

- 5-7 GeV/c: 55(left, prompt) → 76 (top).
- 7-10 GeV/c: 56(left, prompt) → 76 (bottom).
- 10-15 GeV/c: 57(left, prompt) → 77 (top).
- 15-50 GeV/c: 58(left, prompt) → 77 (bottom).

9.2.2 $R = 0.4$

- 5-7 GeV/c: 59(left, prompt) → 78 (top).
- 7-10 GeV/c: 60(left, prompt) → 78 (bottom).
- 10-15 GeV/c: 61(left, prompt) → 79 (top).
- 15-50 GeV/c: 62(left, prompt) → 79 (bottom).

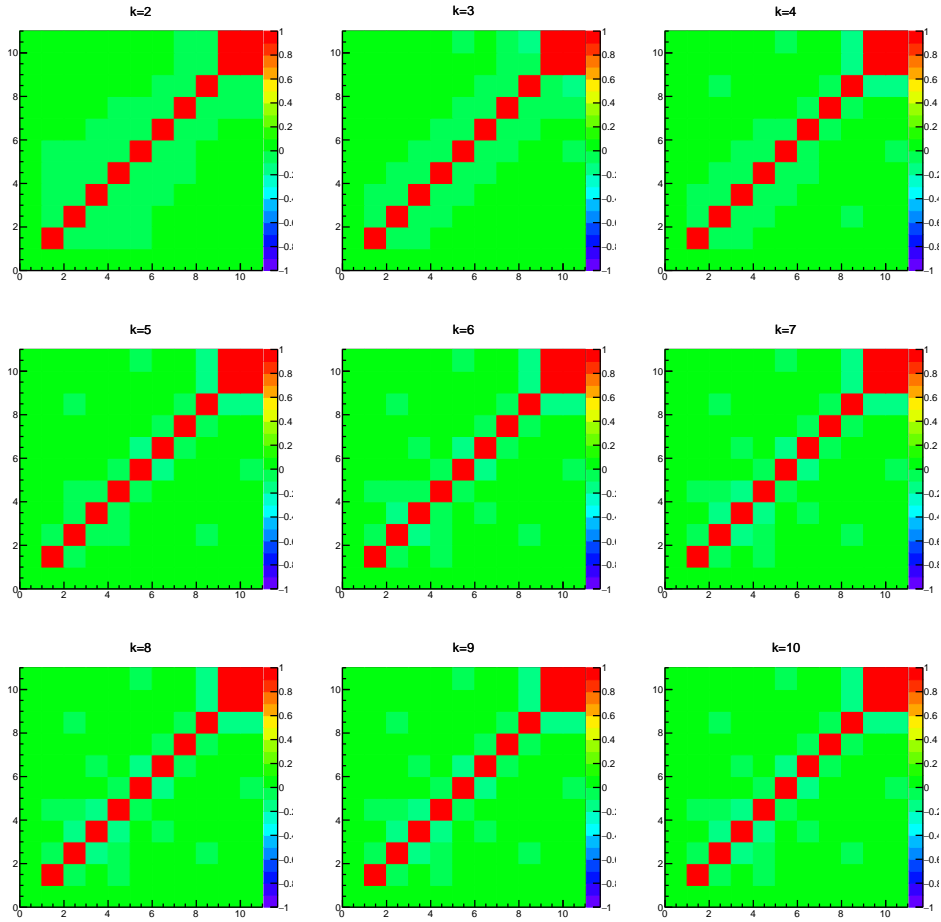


Fig. 75: Pearson coefficients for Bayesian unfolding.

Unfolding is done using the Bayesian approach with default number of iterations as 5. The $z_{||}^{\text{ch}}$ ranges are 0.4 to 1 for both the generator and reconstructed levels. The unfolded spectra can be found at fig. 80 81 82 83 for $R = 0.3$ and at fig. 84 85 86 87 for $R = 0.4$.

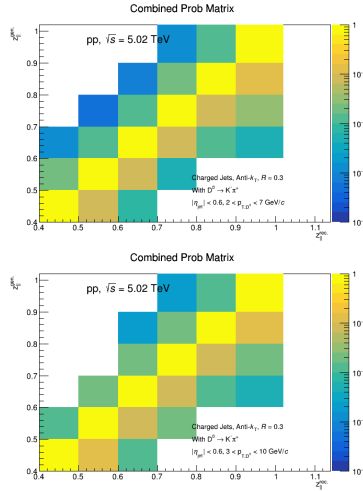


Fig. 76: Rebinned detector response matrix calculated with the PYTHIA part of the simulation of pp events at $\sqrt{s} = 5.02$ TeV: [top] $5 < \text{jet } p_T < 7$ GeV/c and [bottom] $7 < \text{jet } p_T < 10$ GeV/c, $R = 0.3$.

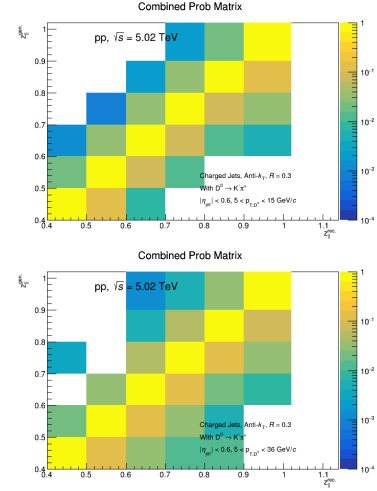


Fig. 77: Rebinned detector response matrix calculated with the PYTHIA part of the simulation of pp events at $\sqrt{s} = 5.02$ TeV: [top] $10 < \text{jet } p_T < 15$ GeV/c and [bottom] $15 < \text{jet } p_T < 50$ GeV/c, $R = 0.3$.

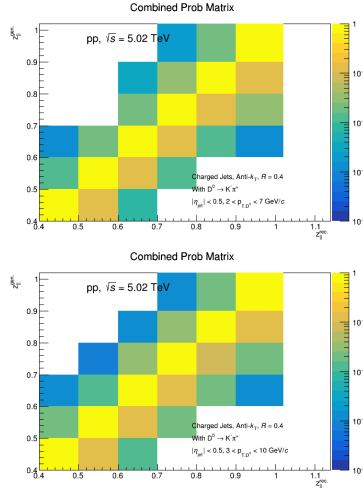


Fig. 78: Rebinned detector response matrix calculated with the PYTHIA part of the simulation of pp events at $\sqrt{s} = 5.02$ TeV: [top] $5 < \text{jet } p_T < 7$ GeV/c and [bottom] $7 < \text{jet } p_T < 10$ GeV/c, $R = 0.4$.

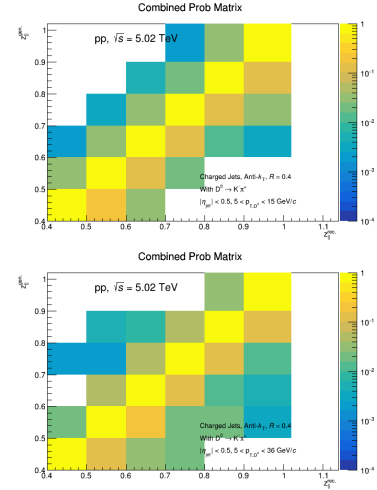


Fig. 79: Rebinned detector response matrix calculated with the PYTHIA part of the simulation of pp events at $\sqrt{s} = 5.02$ TeV: [top] $10 < \text{jet } p_T < 15$ GeV/c and [bottom] $15 < \text{jet } p_T < 50$ GeV/c, $R = 0.4$.

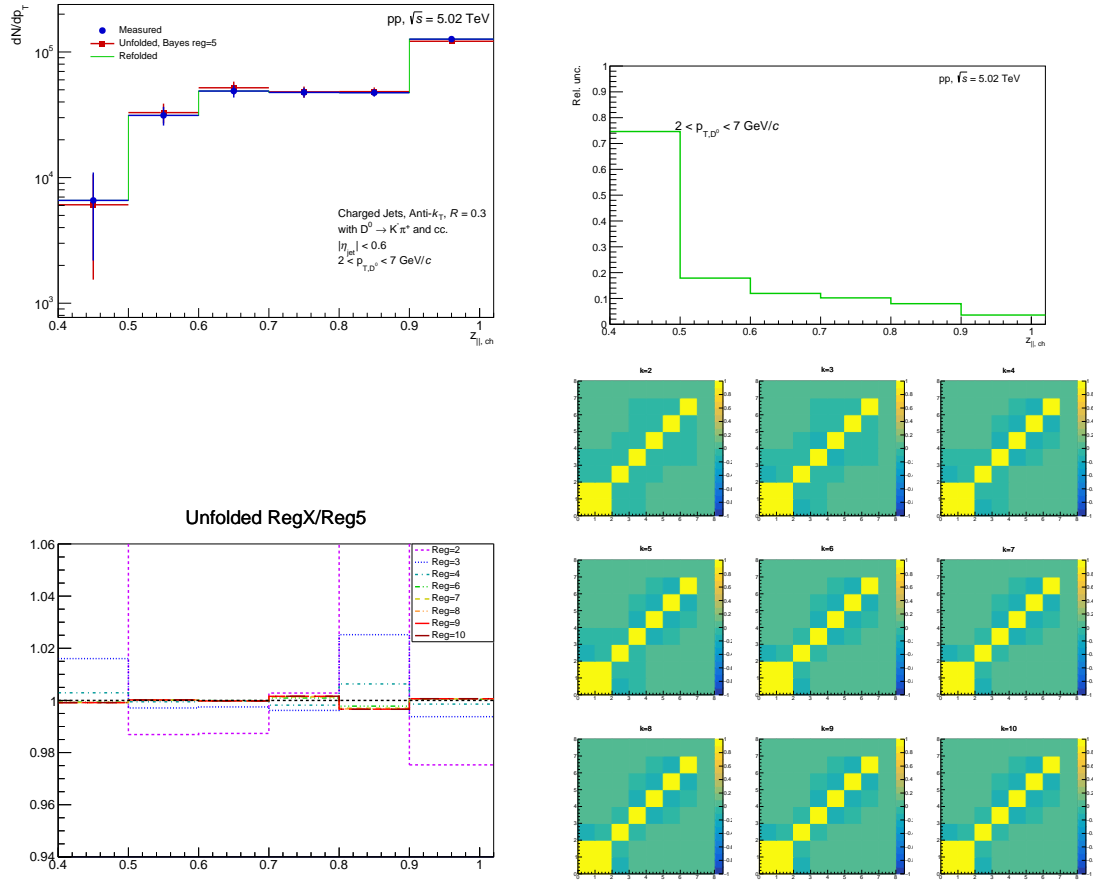


Fig. 80: TOP : Left: Unfolded $z_{||}^{\text{ch}}$ spectra for jet- p_T in 5-7 GeV/c $R = 0.3$. Right: Relative statistical uncertainties after unfolding. BOTTOM : Left: Ratio of spectra unfolded with different number of iterations. Right: Pearson coefficients.

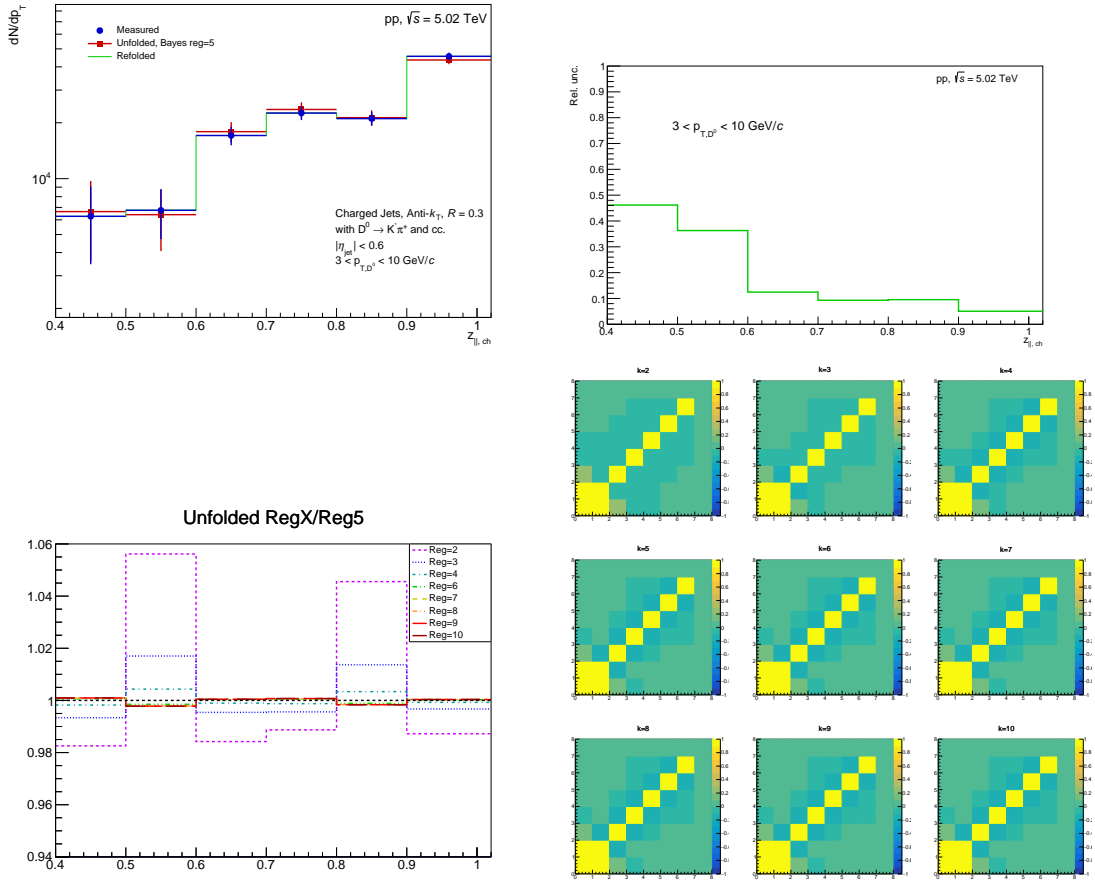


Fig. 81: TOP : Left: Unfolded $z_{\parallel}^{\text{ch}}$ spectra for jet- p_T in 7-10 GeV/ c $R = 0.3$. Right: Relative statistical uncertainties after unfolding. BOTTOM : Left: Ratio of spectra unfolded with different number of iterations. Right: Pearson coefficients.

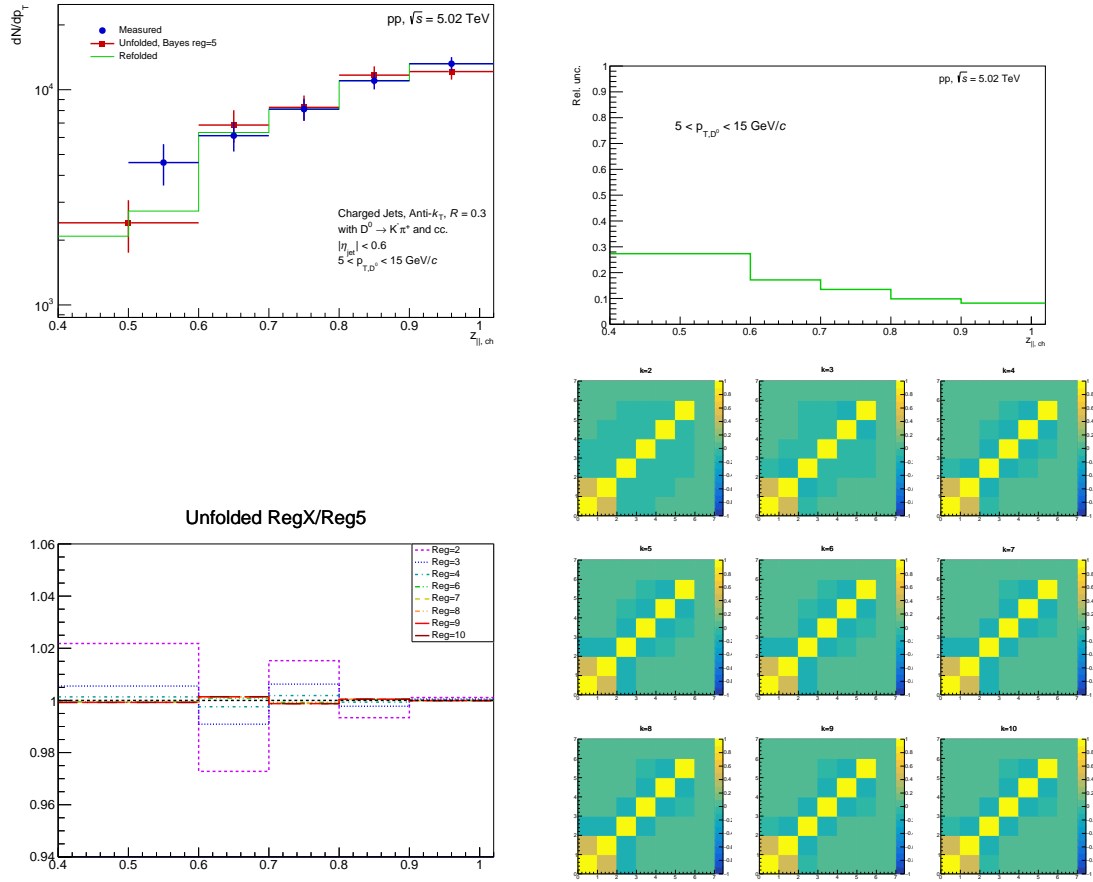


Fig. 82: TOP : Left: Unfolded $z_{||}^{\text{ch}}$ spectra for jet- p_T in 10-15 GeV/c $R = 0.3$. Right: Relative statistical uncertainties after unfolding. BOTTOM : Left: Ratio of spectra unfolded with different number of iterations. Right: Pearson coefficients.

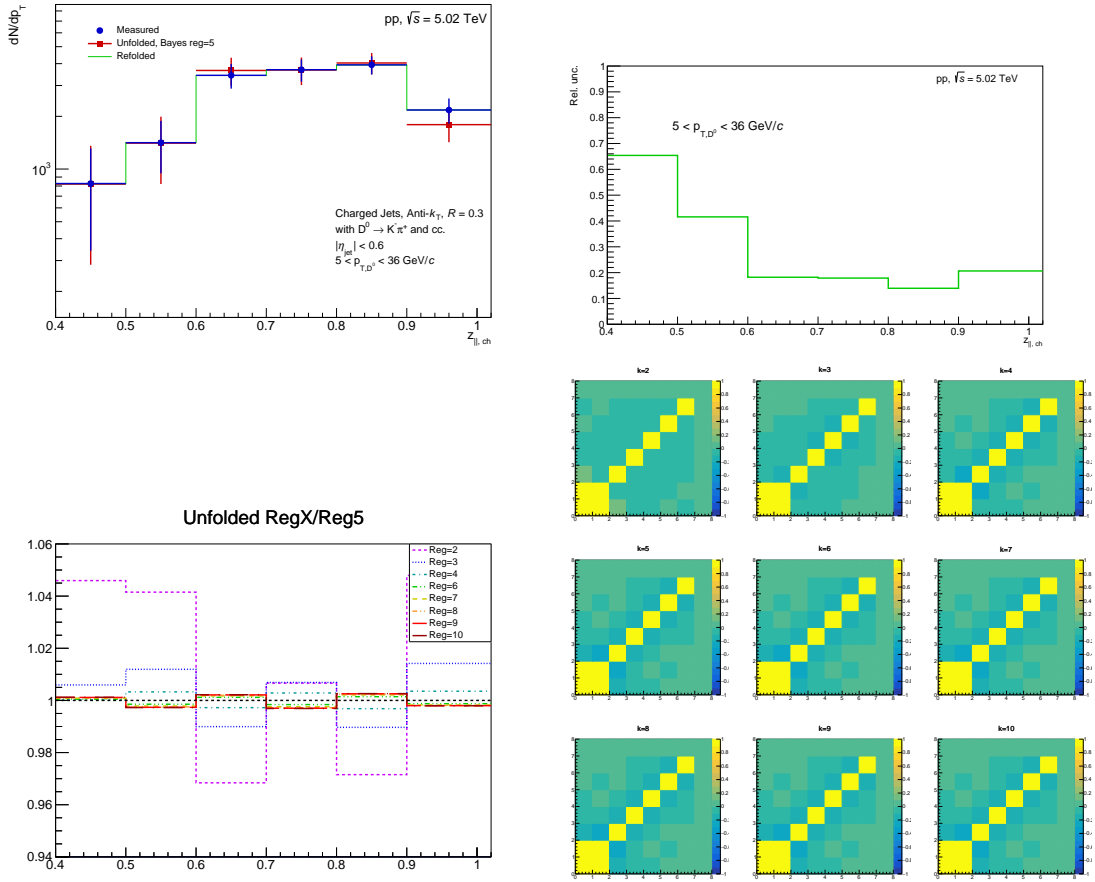


Fig. 83: TOP : Left: Unfolded $z_{\parallel}^{\text{ch}}$ spectra for jet- p_T in 15-50 GeV/c $R = 0.3$. Right: Relative statistical uncertainties after unfolding. BOTTOM : Left: Ratio of spectra unfolded with different number of iterations. Right: Pearson coefficients.

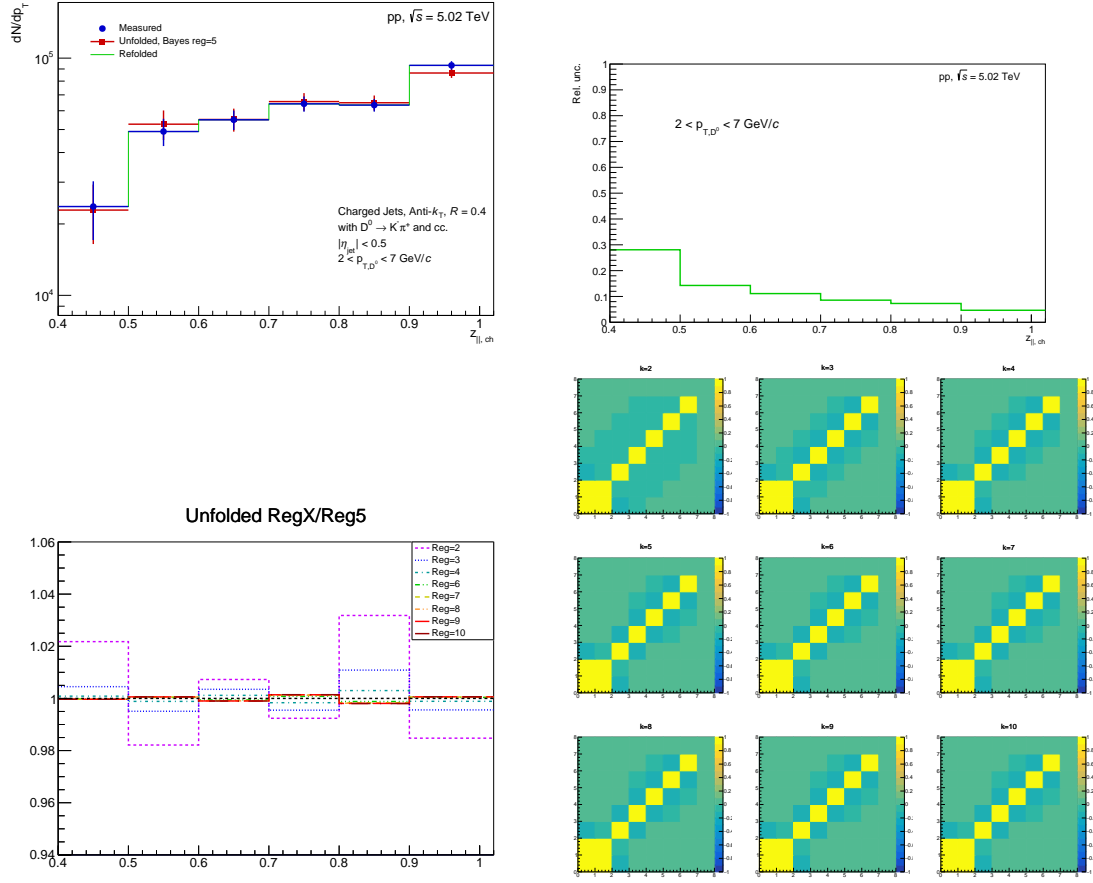


Fig. 84: TOP : Left: Unfolded $z_{\parallel}^{\text{ch}}$ spectra for jet- p_T in 5-7 GeV/c $R = 0.4$. Right: Relative statistical uncertainties after unfolding. BOTTOM : Left: Ratio of spectra unfolded with different number of iterations. Right: Pearson coefficients.

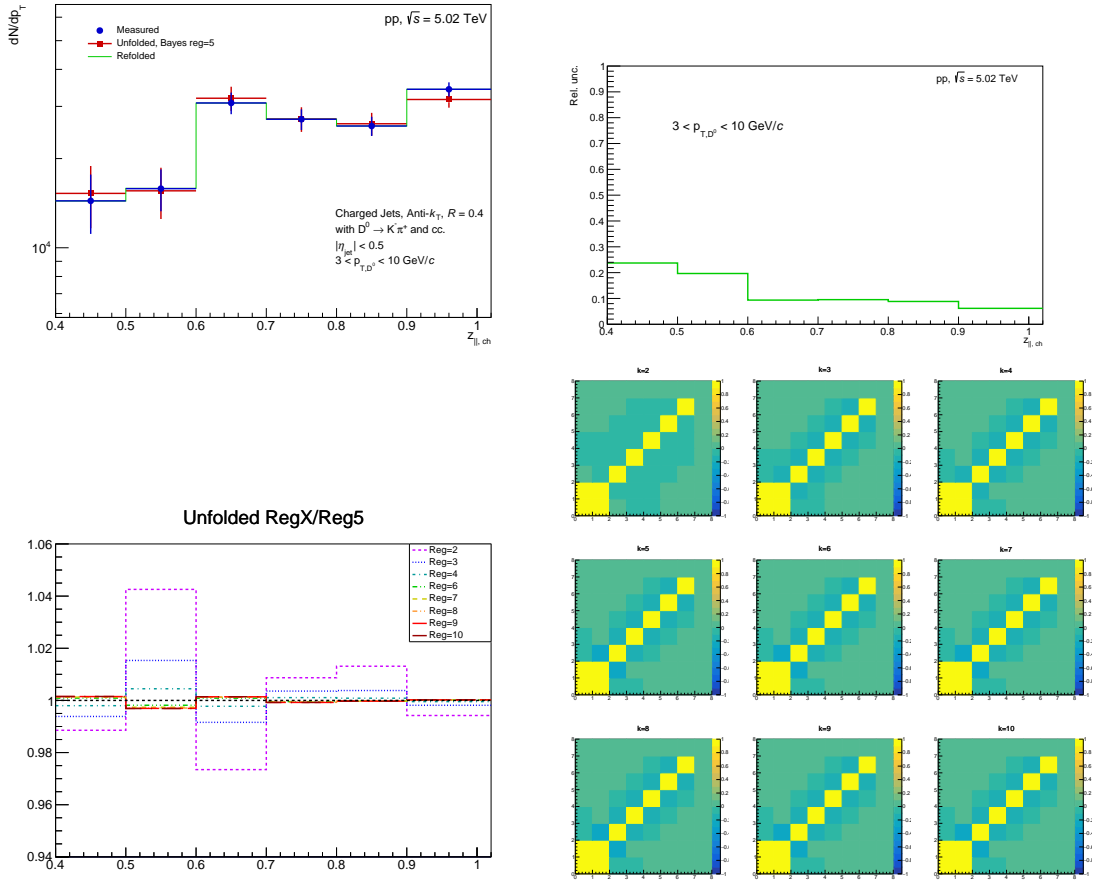


Fig. 85: TOP : Left: Unfolded $z_{\parallel}^{\text{ch}}$ spectra for jet- p_T in 7-10 GeV/ c $R = 0.4$. Right: Relative statistical uncertainties after unfolding. BOTTOM : Left: Ratio of spectra unfolded with different number of iterations. Right: Pearson coefficients.

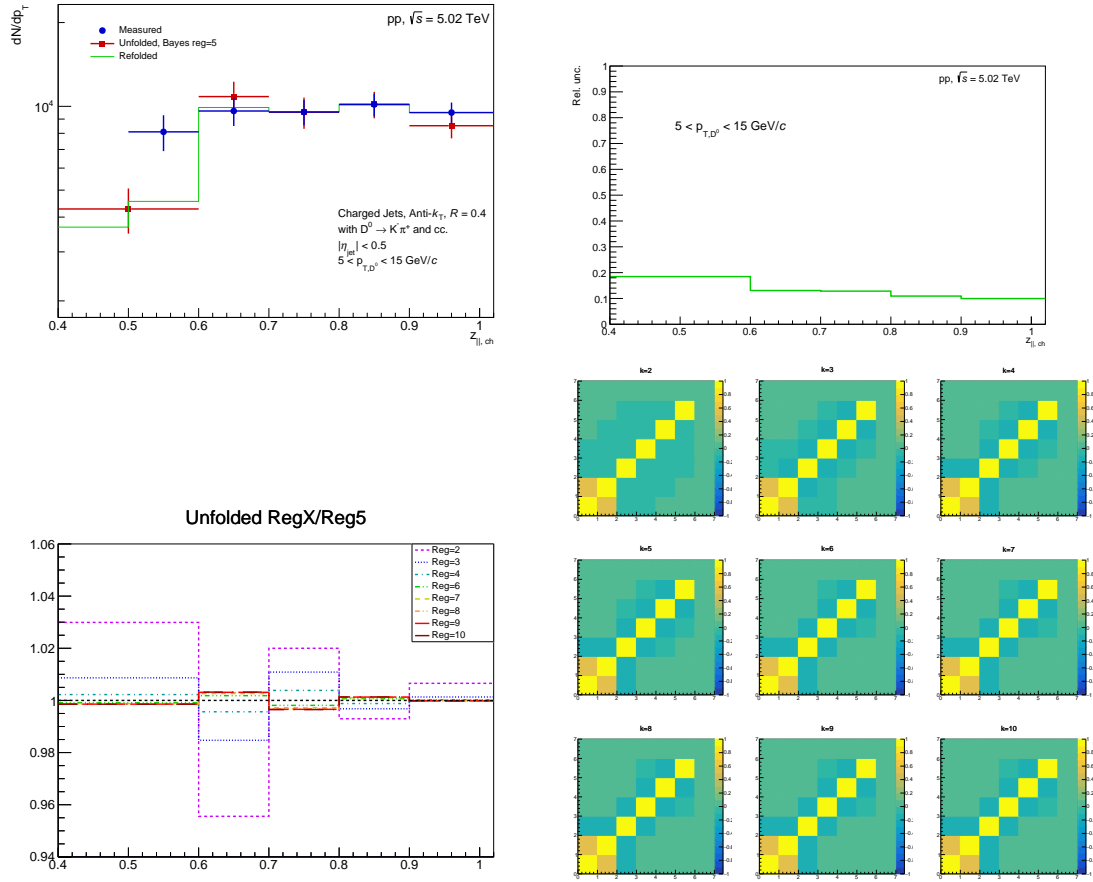


Fig. 86: TOP : Left: Unfolded $z_{||}^{\text{ch}}$ spectra for jet- p_T in 10-15 GeV/c $R = 0.4$. Right: Relative statistical uncertainties after unfolding. BOTTOM : Left: Ratio of spectra unfolded with different number of iterations. Right: Pearson coefficients.

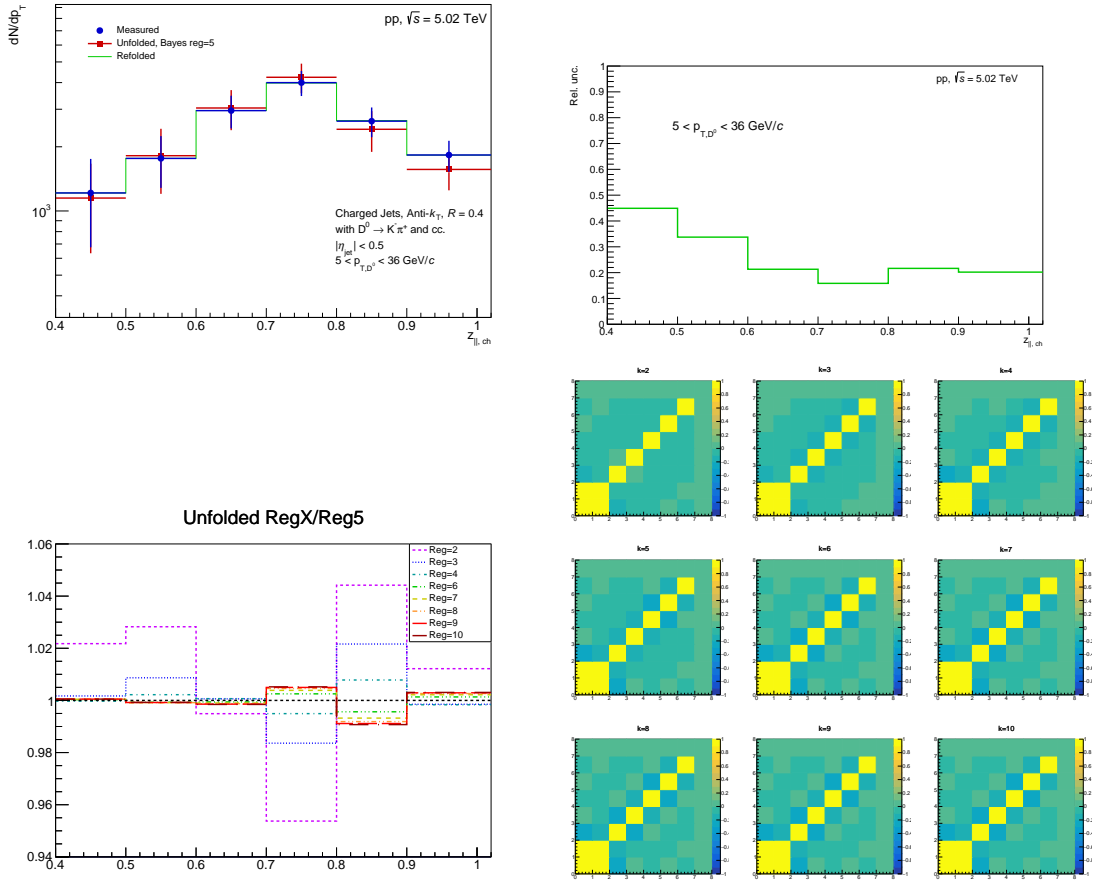


Fig. 87: TOP : Left: Unfolded $z_{\parallel}^{\text{ch}}$ spectra for jet- p_T in 15-50 GeV/c $R = 0.4$. Right: Relative statistical uncertainties after unfolding. BOTTOM : Left: Ratio of spectra unfolded with different number of iterations. Right: Pearson coefficients.

10 Systematic Uncertainties

We considered the following sources of systematic uncertainties:

- Raw yield extraction
- D-Meson Selection Cuts
- B Feed-Down
- Unfolding
- Tracking Efficiency
- p_T Shape of the Monte Carlo Spectrum

10.1 Raw Yield Extraction

10.1.1 Fitting procedure

The stability and systematics of the raw yield extraction has been assessed using the MultiTrial framework developed by the D2H group. This framework performs the fit of the invariant mass distribution many times varying several conditions, such as binning, fixed vs. free parameters, background function, fit range.

The following variations were included in the assessment of the systematics for the raw yield extraction of D^0 jets in pp:

- fixed $\sigma = \sigma_{MC}$;
- fixed $\sigma = 1.15\sigma_{MC}$
- fixed $\sigma = 0.85\sigma_{MC}$
- free σ and fixed $m_0 = m_{PDG}$;
- fixed $\sigma = \sigma_{MC}$ and $m_0 = m_{PDG}$;
- free σ and free m_0 ;
- background functions: exponential, linear, second-order polynomial;
- lower limit of fit range: 1.72, 1.74 GeV/ c^2 ;
- upper limit of fit range: 2.00, 2.03 GeV/ c^2 ;
- rebin by factor 2

Figure 88 shows average of the multi-trial procedure for the side-band method as a function of jet p_T for each $D^0 p_T$ bin scaled by the corresponding efficiency, and sum of all spectra from each $D^0 p_T$ bin (blue). Variations of all trials as a function of jet p_T for each $D^0 p_T$ bin and scaled by the corresponding efficiency are shown in Fig 89.

The systematic uncertainties are calculated as the root-mean-square of all the yields obtained in the multi-trial fits and are shown in Fig. 90.

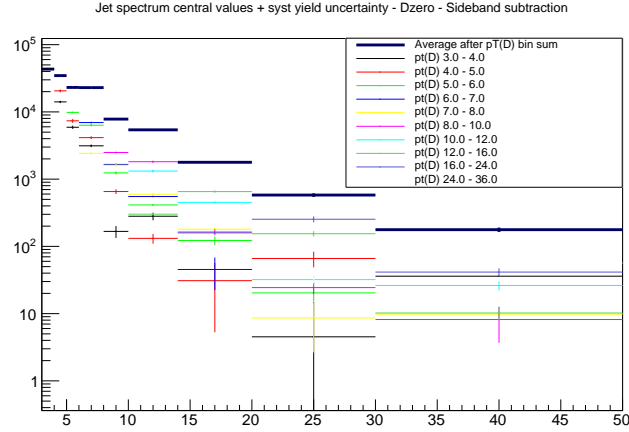


Fig. 88: Average of the multi-trial procedure for the side-band method as a function of jet p_T for each D⁰ p_T bin scaled by the corresponding efficiency, and sum of all spectra from each D⁰ p_T bin (blue).

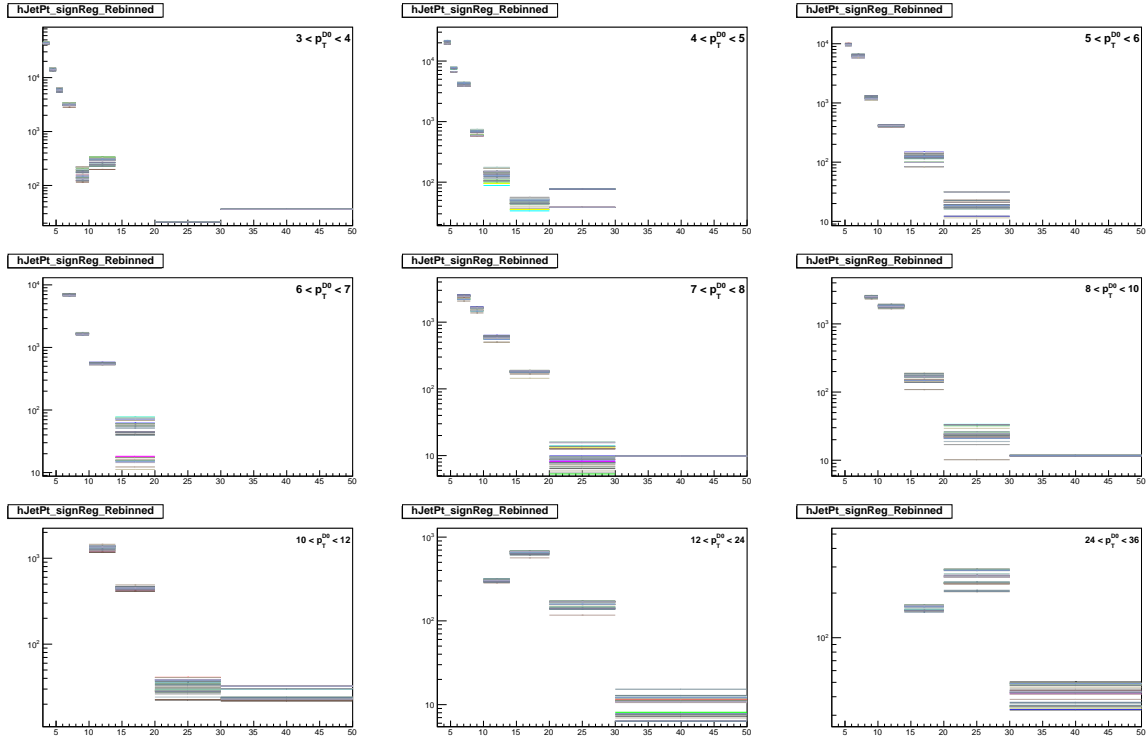


Fig. 89: Variations of all trials as a function of jet p_T for each D⁰ p_T bin and scaled by the corresponding efficiency.

10.1.2 Variation of signal and side-band ranges

As an additional systematic uncertainty, variations of ranges of the signal and side-band definitions in the invariant-mass fit procedure are considered. Figure 91 shows ratios of efficiency and B feed-down corrected yields to the central value and RMS of the variations.

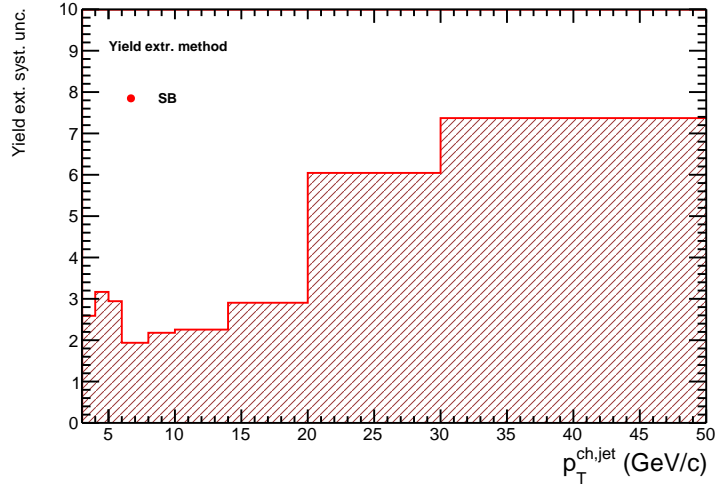


Fig. 90: D^0 -jet systematic uncertainties, RMS.

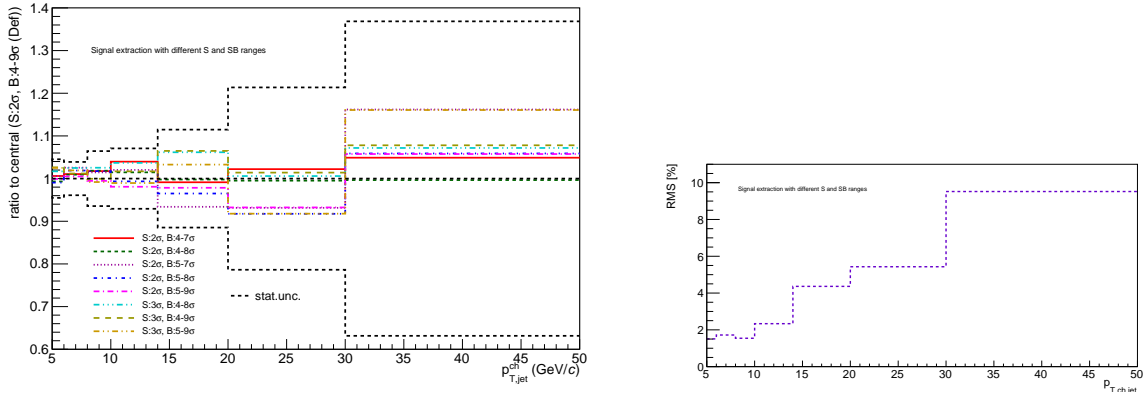


Fig. 91: Left: Systematic uncertainties from the variation of definitions of the signal and side-band regions. Right: Systematic uncertainty: RMS.

10.1.3 Variation of reflection to signal ratio

By default, the ratio reflection/signal is a fixed parameter in the fit and is taken from the MC simulation. The reflection/signal ratio is varied to estimate the systematic uncertainty. Considered variations are $\pm 50\%$ of the default value. Systematic uncertainties arising from these variation on the final unfolded jet p_T spectra are 1-3%, as shown in Fig. 92.

The uncertainties are added in quadratures in order to obtain the final systematic uncertainty on the raw yield extraction.

10.2 D-Meson Selection Cuts

Uncertainties of the D-meson cut selection is estimated by varying cuts applied in the analysis of D-meson selection criteria, as reported in 3.

Eight variations of cut selections are considered, looser sets and tighter sets of cuts. The variations are chosen so that they vary D^0 reconstruction efficiency to high enough extent so that a possible imperfection in MC simulation can be probed. Though at high $p_{T,D}$ the selection criteria are already rather

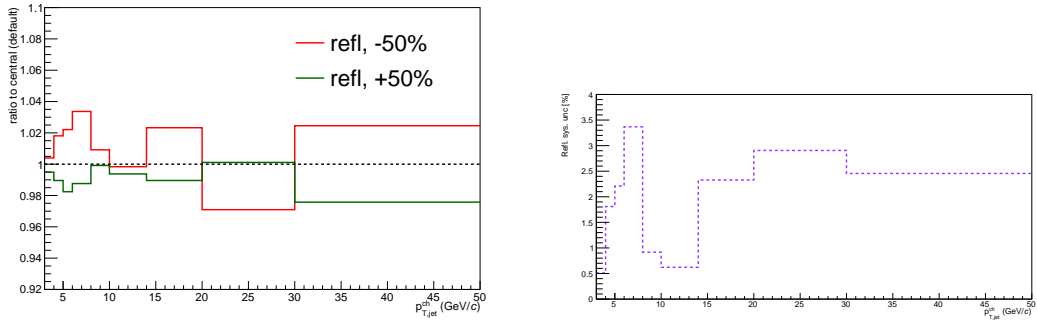


Fig. 92: Left: Ratio of unfolded jet p_T spectrum with $\pm 50\%$ variations of the reflection/signal ratio. Right: Systematic uncertainty, maximum of the variations in each bin.

loose. Raw D⁰-jet p_T distributions with these different cut sets and corresponding D⁰-jet efficiencies are shown in Fig. 93, and ratios to the default set of cuts in Fig. 94. Figure 95 shows non-prompt D⁰-jet reconstruction efficiencies for all the cut variations, and the variations of the FD fraction in the inclusive D⁰-jet spectrum.

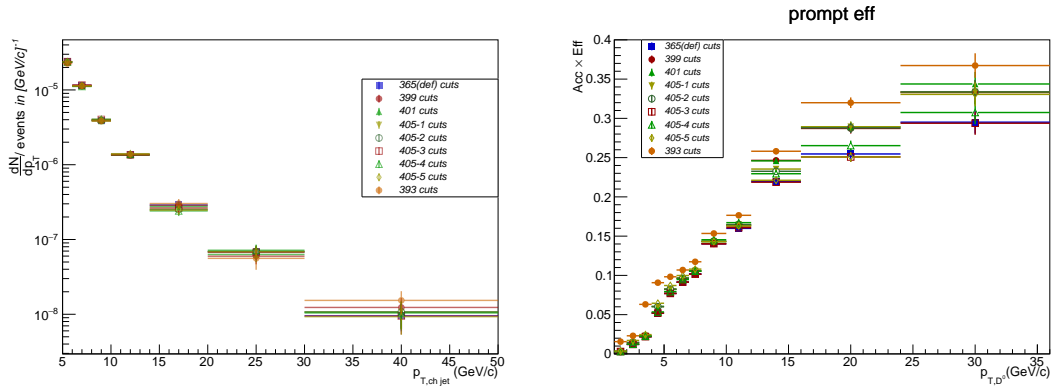


Fig. 93: Left: D⁰-jet p_T distributions with different cut sets for systematic uncertainties estimation. Right: corresponding prompt D⁰-jet efficiencies.

Corrected for the corresponding efficiency D⁰-jet $p_{T,ch,jet}$ distributions are presented in Fig. 96. Systematic uncertainties are estimated by taking ratio of the efficiency-corrected, FD subtracted and unfolded D⁰-jet $p_{T,ch,jet}$ distributions with different cut variations to the D⁰-jet p_T spectrum obtained with the default cut set and taking RMS of them, as shown in Fig. 96.

10.3 B Feed-Down Correction

The B Feed-Down (FD) cross section is obtained from a POWHEG+PYTHIA6 simulation, as discussed in Section 8. In order to assess the systematic uncertainty the same simulation is performed with different choices of the quark mass m_b , the factorization scale factor μ_F , and the renormalization scale factor μ_R . Table 2 shows the list of parameters used to determine the central points and the variations used to determine the systematic uncertainty.

$p_{T,ch,jet}$ p_T differential cross-section for $B \rightarrow D^0$ for all the variations and ratios to the default cross-section are shown in Fig. 97. The $p_{T,ch,jet}$ distribution is with the analysis cut on $3 < p_{T,D} < 36 \text{ GeV}/c$, ratios before scaling by non-prompt to prompt efficiency are shown in Fig. 97.

The non-prompt D⁰-jet p_T spectrum after correcting for the efficiency and smearing with the detector

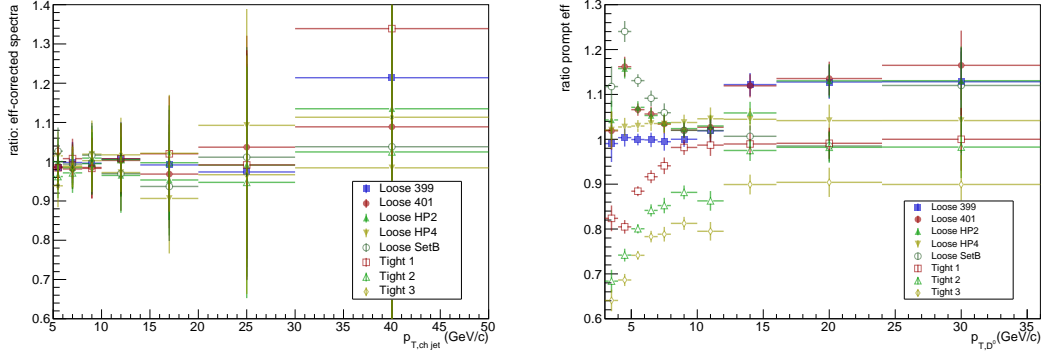


Fig. 94: Left: Ratios of the prompt efficiencies for different cut sets for systematic uncertainties estimation. Right: ratios of the corresponding D^0 -jet efficiencies zoomed in as necessary.

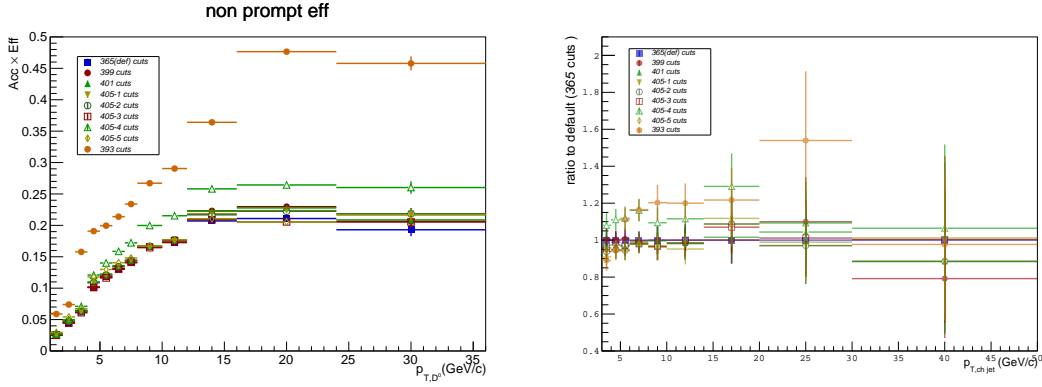


Fig. 95: Ratios of D^0 -jet non-prompt reconstruction efficiencies (left) and FD fractions (right) with different cut sets for systematic uncertainties estimation.

Table 2: Parameters of the POWHEG+PYTHIA6 simulations used to estimate the B Feed-Down.

Parameter	Central Value	Variations
m_b	4.75 GeV/ c^2	4.5, 5.0 GeV/ c^2
PDF	CT10nlo (11000)	—
(μ_F, μ_R)	(1,1)	(0.5,0.5), (0.5, 1), (1, 0.5), (2,2), (2,1), (1,2)

effects is shown in Fig. 63, together with systematic uncertainties obtained by taking the largest upward and downward variation from the central point in each bin, therefore the shown uncertainties are asymmetric (see left panel of Fig. 98). AS the FD subtraction systematic uncertainty the largest between the upward and downward uncertainty is used in order to have a symmetric uncertainty, as shown in Fig. 98.

10.4 Unfolding

Unfolded D^0 -jet p_T spectrum using the Bayesian method with 4 iteration was shown in Fig. 73, and the evolution of D^0 -jet spectrum in pp collisions increasing number of iterations compare to Bayesian unfolding with 4 iterations was shown in Fig. 74. The default $p_{T, ch jet}$ ranges for the unfolding procedure are $3 < p_{T, ch jet} < 50$ both at the generator and reconstructed level p_T with over/under flow bins considered in the unfolding procedure, where $p_{T, jet}^{reco}$ is also the range of the measured in the data D^0 -jet

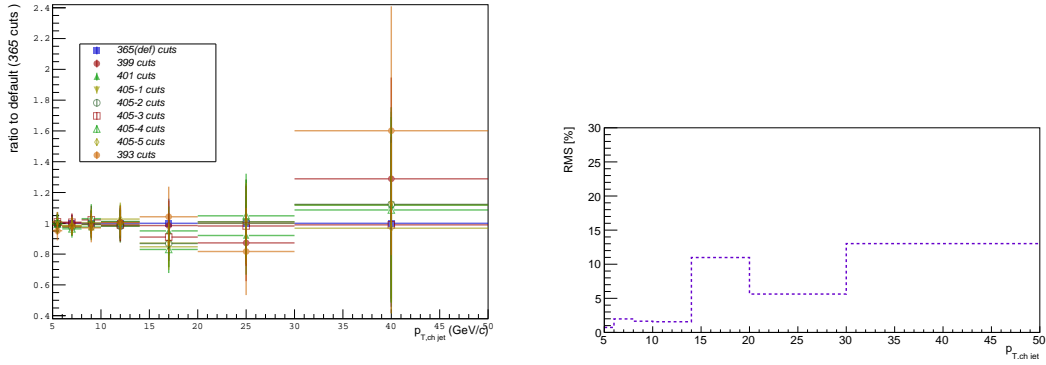


Fig. 96: Left: Ratio of the efficiency-corrected D⁰-jet p_T distributions with different cut sets for systematic uncertainties estimation. Right: RMS - systematic uncertainties.

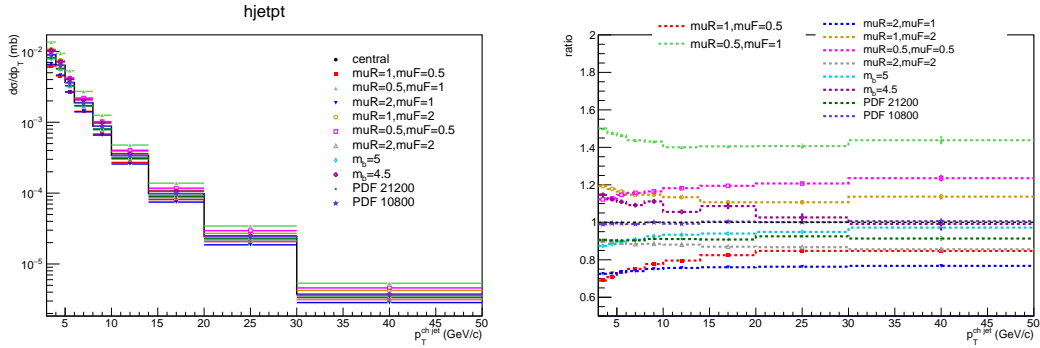


Fig. 97: Non-prompt (B Feed-Down) D⁰-jet cross section in pp at $\sqrt{s} = 5.02$ TeV as a function of $p_{T, \text{ch jet}}$, obtained in POWHEG+PYTHIA6 simulations with different choices of the simulation parameters, $p_{T, D}$ 3-36 GeV/c.

p_T spectrum being unfolded. As systematic checks these ranges are varied. Additional check of the unfolding was done by performing unfolding using the SVD algorithm with $reg = 6$. All these checks are summarized in Fig. 99 as ratios of the unfolded spectra to the default case. The assigned systematic uncertainty is from the RMS. Influence of the change of the upper range of the $p_{T, \text{jet}}^{\text{gen}}$ was also checked by using following ranges: $3 < p_{T, \text{jet}}^{\text{reco}} < 50$, $3 < p_{T, \text{jet}}^{\text{gen}} < 50$ and $5 < p_{T, \text{jet}}^{\text{reco}} < 50$, $5 < p_{T, \text{jet}}^{\text{gen}} < 50$.

Figure 100 (left) shows unfolded jet p_T spectrum using Bayesian unfolding with 4 iterations (left) and unfolded spectra with next iterations compared to the default spectrum obtained after 4 iterations (right). Unfolded spectrum with SVD method using 6 iterations is presented in Fig. 101 (left) together with ratio of the unfolded spectra with different regularization parameters to the default unfolded spectrum with $reg=6$ (right).

The baseline prior used for unfolding is the spectrum obtained (at the generator level) from PYTHIA. For the variations, the priors were obtained from a modified power-law function:

$$f(p_{T, \text{jet}}) = p_{T, \text{jet}}^{-a} e^{-\frac{ab}{p_{T, \text{jet}}}}, \quad (4)$$

where a is the power-law index and b is the position of the local maximum of the distribution. The exponential factor $e^{-\frac{ab}{p_{T, \text{jet}}}}$ was added to avoid infinities at zero and have a more realistic spectrum (the physical cross-section goes to zero for $p_{T, \text{jet}} \rightarrow 0$). Used variations are:

- prior0: $a = 4.6$ $b = 4$ GeV/c

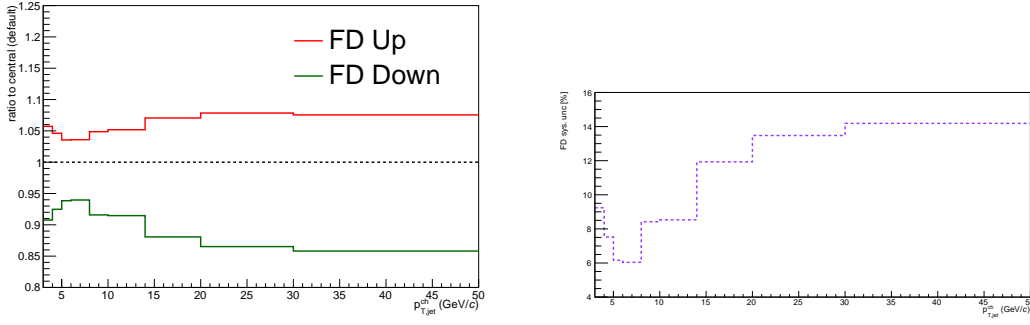


Fig. 98: Systematic uncertainties on the unfolded D^0 -jet p_T spectrum from the B feed-down subtraction.

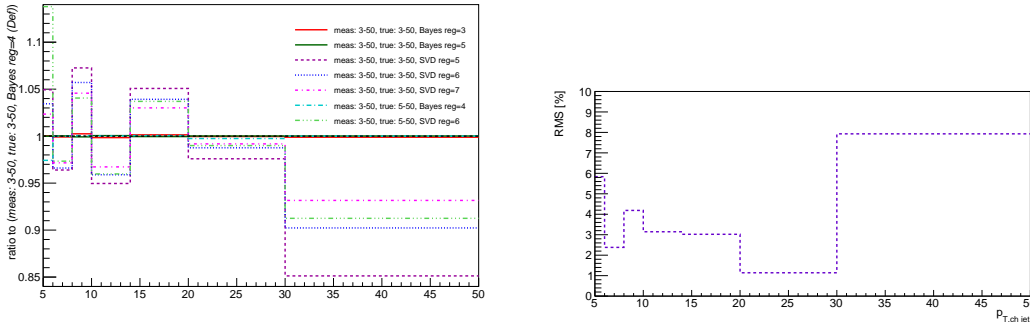


Fig. 99: Ratio of unfolded D^0 -jet p_T spectra with different ranges of $p_{T,jet}^{reco}$ and $p_{T,jet}^{gen}$ using Bayesian and SVD unfolding methods with different iterations (left) and systematic uncertainties from the RMS (right).

- prior1: $a = 3$ $b = 4$ GeV/ c
- prior2: $a = 4$ $b = 4$ GeV/ c
- prior3: $a = 5$ $b = 4$ GeV/ c
- prior4: $a = 6$ $b = 4$ GeV/ c
- prior6: $a = 4.5$ $b = 3$ GeV/ c
- prior7: $a = 4.5$ $b = 5$ GeV/ c
- prior8: fit to the measured spectrum

Example of priors compared to the PYTHIA D^0 -jet p_T spectra at the generator level are shown on Fig. 103. Ratios of the unfolded D^0 -jet p_T spectra with variation of the functions used as priors to the central D^0 -jet p_T spectrum using the Bayesian unfolding with 4 iterations are shown in Fig. 104.

10.5 Tracking Efficiency

Uncertainties on the tracking efficiency affect the measurement in two ways.

First, it introduces an uncertainty on the D-meson reconstruction efficiency. This was evaluated for the D-meson spectra to be 3% for D^0 (mostly p_T -independent). Since we have verified that the reconstruction efficiency itself does not depend on $p_{T,chjet}$ we can assume that our measurement is affected by the same uncertainty.

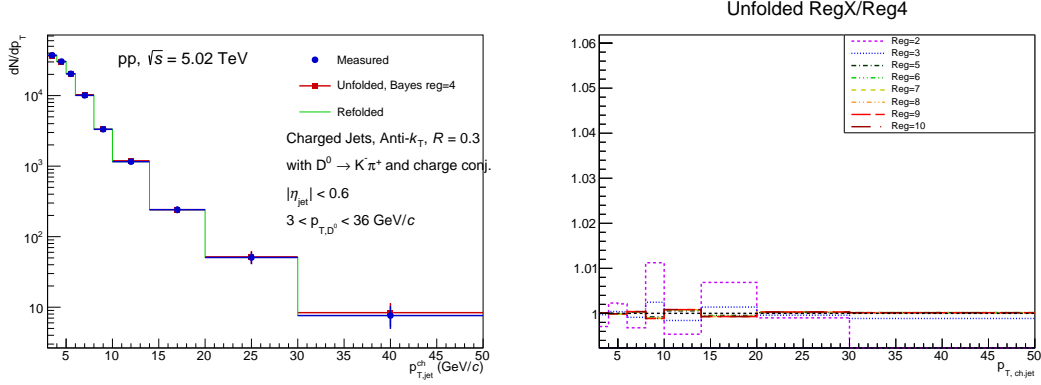


Fig. 100: Left: Corrected jet p_T spectrum before (blue) and after (red) the unfolding procedure (Bayesian method with 4 iterations). Right: Ratio with the default unfolded spectrum with 4 iteration of the unfolded spectra for up to 10 iterations in the Bayesian unfolding. The considered jet p_T range is above 5 GeV/c.

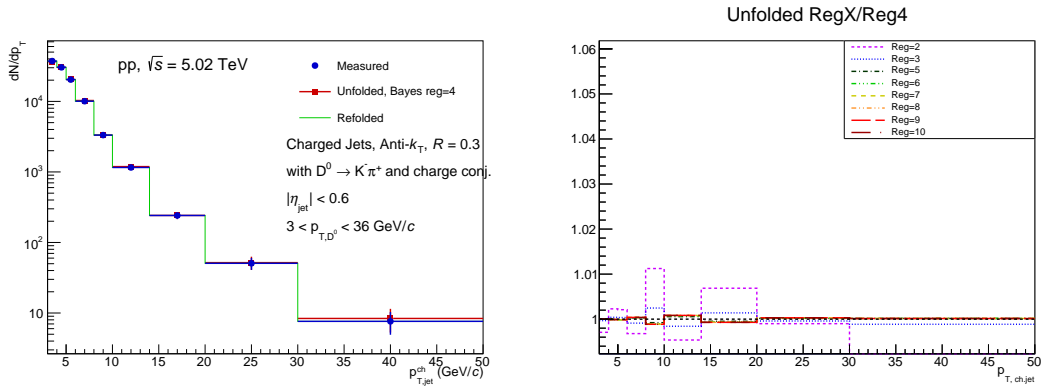


Fig. 101: Left: Corrected jet p_T spectrum before (blue) and after (red) the unfolding procedure (SVD method with 6 iterations). Right: ratio of the measured spectrum to the refolded for up to 10 iterations in the SVD unfolding. The considered jet p_T range is above 5 GeV/c.

10.6 Tracking Efficiency – Jet Energy Scale

Tracking efficiency also affects the detector response. To estimate the uncertainty on the final yield, a new detector response has been built where the efficiency has been reduced to 96% of its normal value, by throwing randomly away 4% of the reconstructed track in the simulation. The raw spectrum is unfolded using this modified response matrix and the outcome is compared with the reference result. The resulting systematic uncertainty is presented in Fig. 106. As a cross-check of the observed effect the efficiency was also reduced to 95% and the both cases were fitted in order to check linearity, the quoted uncertainty is assumed to be symmetric. The systematic uncertainty is estimated by fitting the ratio and as the uncertainty the value obtained from the fitted function is used, the final systematic uncertainties are shown in Fig. 106.

10.7 p_T Shape of the Monte Carlo Spectrum

The D-jet reconstruction efficiency is estimated using a PYTHIA6+GEANT3 simulation. A possible source of systematic uncertainty is the $p_{T,D}$ shape of the Monte Carlo spectrum. Since the efficiency is calculated as a function of D meson, the shape of the D meson $p_{T,D}$ spectrum is compared to FONLL, a parallel studies within the D2H group were performed. In this Monte Carlo production the generated shape and the FONLL shape agree with each other very well. Therefore, no systematic uncertainties from the $p_{T,D}$ shape of the Monte Carlo Spectrum are assigned.

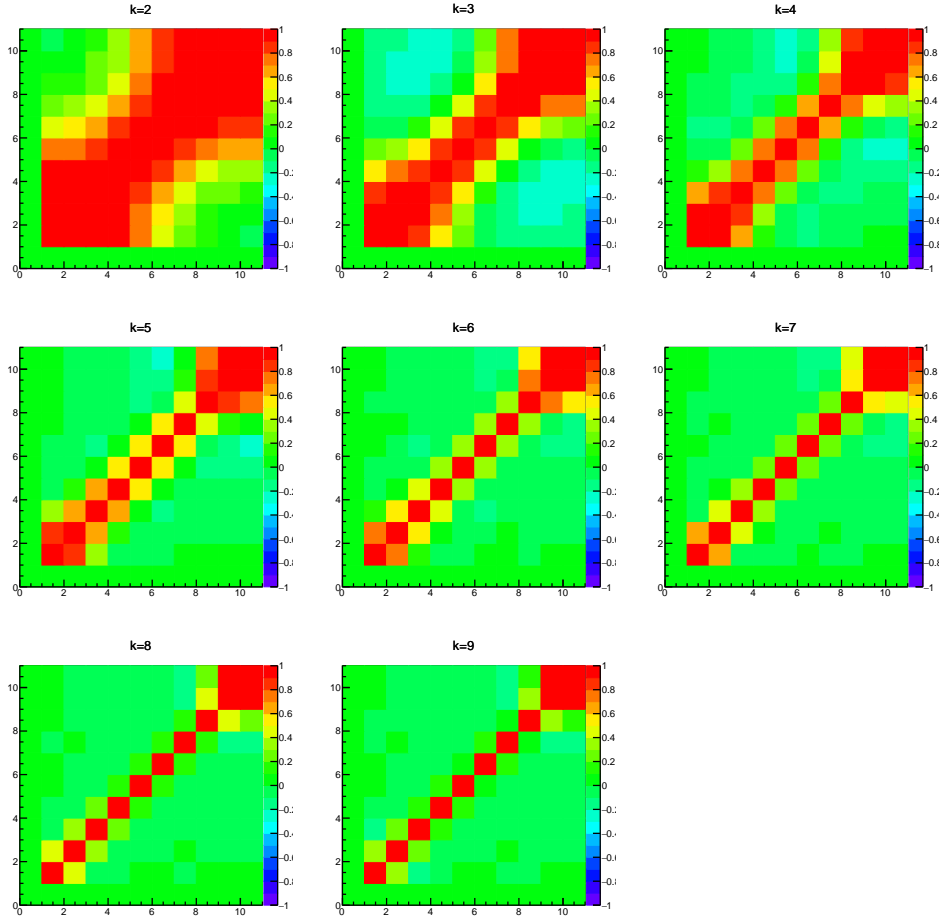


Fig. 102: Pearson coefficients for SVD unfolding.

10.8 Summary of Systematic Uncertainties

The p_T -independent uncertainties are listed in Table ?? . The summary of all uncertainties, including statistical uncertainties are listed for all $p_{T,\text{chjet}}$ bins of the final spectrum in Table 3.

10.8.1 Systematic Uncertainties for R_{pPb}

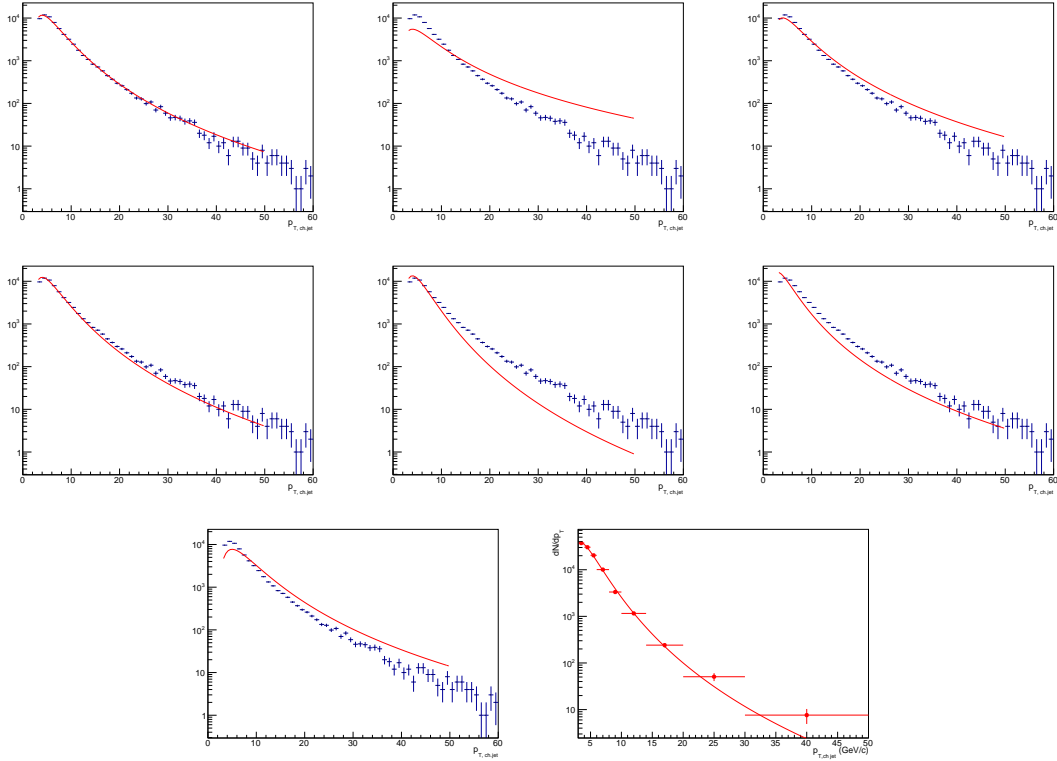


Fig. 103: Different priors compared to the PYTHIA D⁰-jet p_T spectra at the generator level.

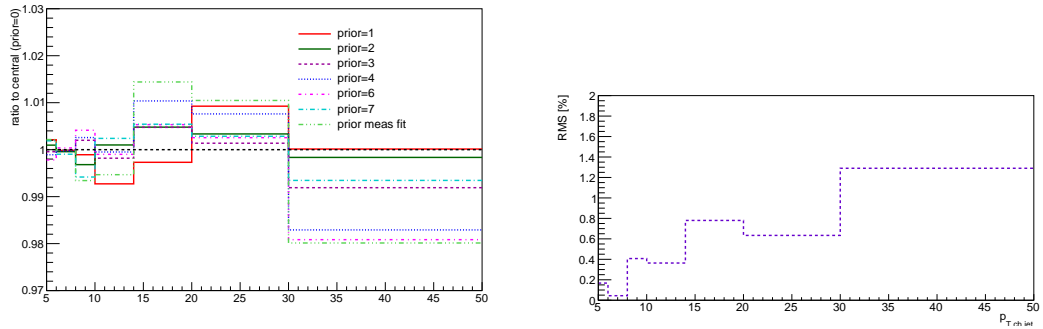


Fig. 104: Unfolded D⁰-jet p_T spectra with different priors used in the unfolding procedure, using Bayes unfolding method with 4 iterations (left) and RMS (right).

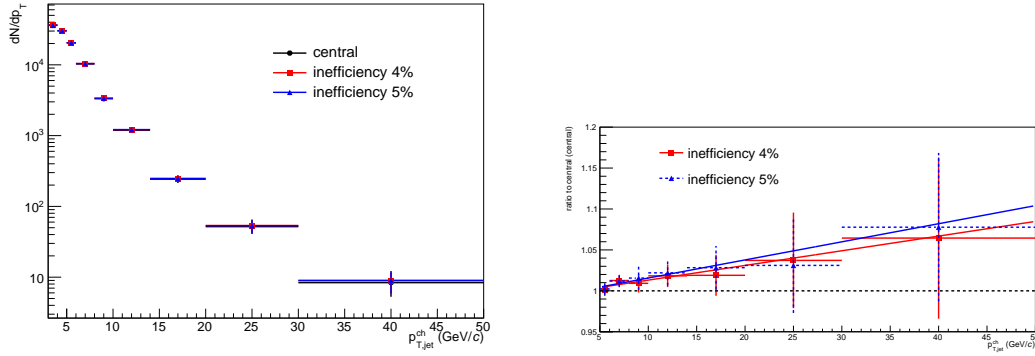


Fig. 105: Unfolded D^0 -jet spectra (left) and a ratio (right) between default unfolding result and with reduced tracking efficiency to 95%.

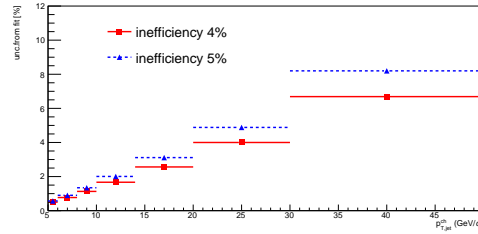


Fig. 106: Systematic uncertainty from the JES, for 4% and 5% inefficiency on D^0 -jet spectra. The final uncertainty is taken from the 4% efficiency case.

Table 3: D^0 -jet: Summary of all uncertainties.

Source	Uncertainty (%)						
$p_{T,chjet}$ (GeV/c)	5 - 6	6 - 8	8 - 10	10 - 14	14 - 20	20 - 30	30 - 50
Raw Yield Extraction (Multi-trial)	3	2	2.5	2.5	3	6	7
Reflections	2	3	2	2	2	3	3
B Feed-Down (x-section)	6	6	8.5	8.5	12	13.5	14
B Feed-Down (R_{pPb})	± 2	± 1	$+3, -1$	$+2, -1$	$+3, -1$	± 1	$+2, -3$
Side-Band and Signal ranges	2	2	2	2	4.5	5.5	6
Unfolding: Bayes	2	0	0	0	0	0	0
Unfolding: SVD	6	2.5	5	4	4	1	9
Unfolding: priors	1	1	1	1	1	1	1
p_T shape of MC (taken from D2H)	0	0	0	0	0	0	0
Tracking Eff. (taken from D2H)	3	3	3	3	3	3	3
Tracking Eff. (Jet Energy Scale)	1	1	1	2	3	4	7
Selection Cuts	1	2	2	2	6	6	6
Total Systematic Uncertainty	10	9	11	11	16	18	20
Normalization Uncertainty	2.1 (Lum) ; 0.04 (BR)						
Statistical	4	3	5	5	8	15	27

11 Results

This section contains a summary of the results for the D -jet p_T -differential cross-section in pp collisions at $\sqrt{s} = 5.02$ TeV with all corrections applied (reconstruction efficiency, B feed-down subtraction, unfolding for detector momentum resolution). The cross-section is calculated according to the following formula:

$$\frac{d^2\sigma}{d\eta dp_T} = \frac{1}{L_{\text{int}} f_{\text{BR}}} \frac{1}{\varepsilon \times A} \frac{1}{2} N_{D\text{-jets}}(p_{T,\text{jet}}), \quad (5)$$

where $L_{\text{int}} = N_{\text{evt}}/\sigma_{\text{inel}}$ is the integrated luminosity ($\sigma_{\text{pp,inel}} = 51.2$ mb), f_{BR} is the branching ratio of the D-meson decay channel used in the analysis, $N_{D\text{-jets}}(p_{T,\text{jet}})$ is the measured number of D-jets in a given $p_{T,\text{jet}}$ bin (with all corrections applied).

The D^0 -tagged jet p_T differential cross section in pp collisions at $\sqrt{s} = 5.02$ TeV compared to POWHEG+PYTHIA6 prediction is shown in Fig 107.

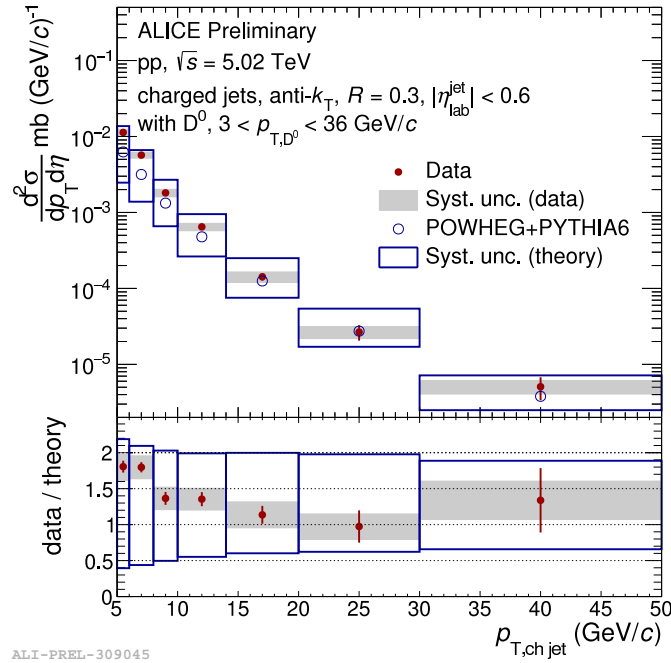


Fig. 107: Unfolded D^0 -jet spectrum in pp collisions at $\sqrt{s} = 5.02$ TeV compared to POWHEG+PYTHIA6 simulations, with the simulation uncertainty.

11.0.1 Monte Carlo Simulations

We performed a set of Monte Carlo simulations using POWHEG and PYTHIA6 to compare with our measurement. The simulations follow the same recipe used for simulating the non-prompt fraction for the B feed-down correction. We simulated 25 M $c\bar{c}$ events with POWHEG+PYTHIA6 for the central points plus several variations of the parameters of the simulation, listed in Table 4.

The systematic uncertainties are obtained by taking the largest upward and downward variation.

Table 4: Parameters of the POWHEG+PYTHIA6 simulations of $c\bar{c}$ events used to compare with our measurement.

Parameter	Central Value	Variations
m_c	1.5 GeV/ c^2	1.3, 1.7 GeV/ c^2
PDF	CT10nlo (11000)	—
(μ_F, μ_R)	(1,1) (0.5,0.5), (0.5, 1), (1, 0.5), (2,2), (2,1), (1,2)	

12 Preliminary Figures

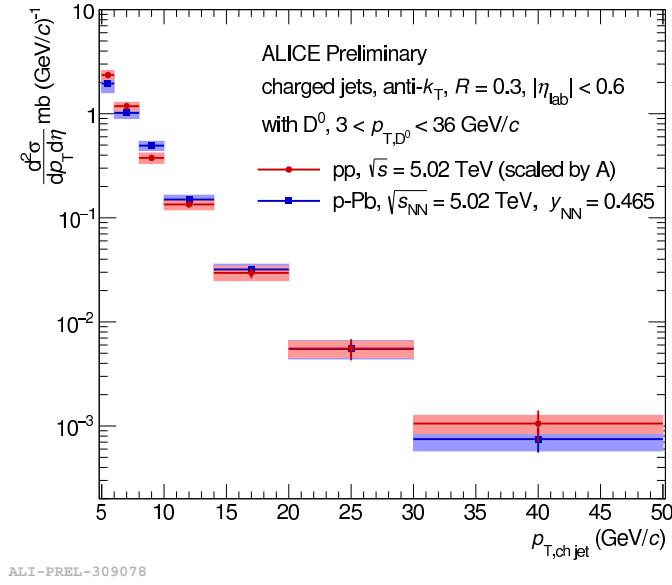
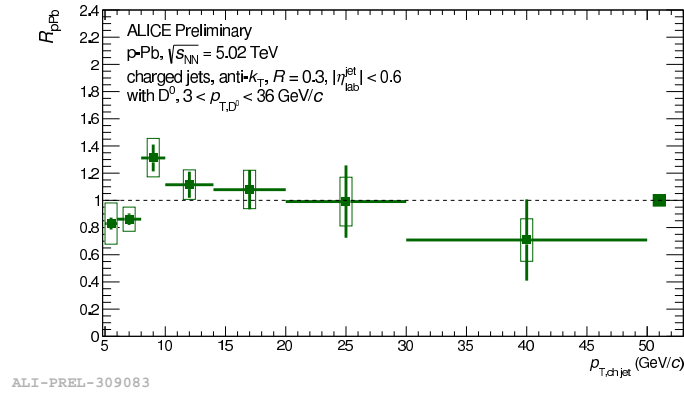


Fig. 108: D^0 -jet cross section in pp at $\sqrt{s} = 5.02$ TeV as a function of $p_{T,\text{ch jet}}$ compared with D^0 -jet cross section in p-Pb at $\sqrt{s} = 5.02$ TeV.

13 Nuclear Modification Factor ($R_{p\text{Pb}}$)

Fig. 109: D⁰-jet R_{pPb}

References

- [1] Tanabashi M *et al.* (ParticleDataGroup) 2018 *Phys. Rev.* **D98** 030001
- [2] Cacciari M, Salam G P and Soyez G 2012 *Eur.Phys.J.* **C72** 1896 (*Preprint* 1111.6097)
- [3] Cacciari M, Salam G and Soyez G 2008 *JHEP* **04** 063
- [4] Cacciari M, Greco M and Nason P 1998 *JHEP* **9805** 007 (*Preprint* 9803400)
- [5] Abelev B *et al.* (ALICE) 2012 *JHEP* **01** 128 (*Preprint* 1111.1553)
- [6] Abelev B *et al.* (ALICE) 2014 *Phys. Rev. Lett.* **113**(23) 232301 (*Preprint* 1405.3452)
- [7] Adam J *et al.* (ALICE) 2016 (*Preprint* 1605.07569)
- [8] Alioli S, Nason P, Oleari C and Re E 2010 *Journal of High Energy Physics* **2010** 1–58 ISSN 1029-8479
- [9] Cacciari M *et al.* 2012 *JHEP* **2012** 1–24 ISSN 1029-8479 (*Preprint* 1205.6344)